JET-P(94)61

Many Authors

JET Posters and Papers presented at the 36th Annual Meeting, APS Division of Plasma Physics

(Minneapolis, Minnesota, USA, 7-11 November 1994)

JOINT EUROPEAN TORUS

JET-P(94)61

JET Posters and Papers presented at the 36th Annual Meeting, APS Division of Plasma Physics

(Minneapolis, Minnesota, USA, 7-11 November 1994)

Many Authors.

JET Joint Undertaking, Abingdon, Oxfordshire, OX14 3EA, UK.

Preprint of papers to be to be published in the Proceedings of
36th Annual Meeting, APS Division of Plasma Physics
(Minneapolis, Minnesota, USA, 7-11 November 1994)

November 1994

JET Posters and Papers presented at the
36th Annual Meeting , APS Division of Plasma Physics
(Minneapolis, Minnesota, USA, 7-11 November 1994)

The New Phase of JET and Prospects for Future Operation

The JET Team
(presented by B Tubbing)

JET Joint Undertaking, Abingdon, Oxfordshire, OX14 3EA, UK.

The Joint European Torus (JET) [Fusion Technol. **11**, 1 (1987)] restarted operations in its new Pumped Divertor configuration. The main elements of the new configuration are four divertor coils, an inertially cooled divertor structure, and an internal cryogenic vacuum pump. Two major differences were observed with respect to the 'old' JET. First, the heat load capability of the divertor is dramatically improved. Second, in the High confinement mode (H-mode) the occurrence of Edge Localised Modes (elms), is more prevalent. Quasi steady-state elmy H-modes are now obtained in a wide variety of conditions. In the 1994 experimental campaign maximum plasma currents of 4MA have been obtained. Steady-state H-mode operation has been obtained for a duration of 20s. Detached divertor operation was established in ohmic and L-mode plasmas, but not yet in H-mode. In low current discharges a poloidal beta $\beta_P = 2.6$ has been obtained in transient. The high β_P regime has been extended to long pulse elmy H-mode. Preliminary experiments have not shown an effect of magnetic shear reversal on the confinement. Using the new internal saddle coils, powered by high frequency amplifiers, Toroidal Alfven Eigen-modes (TAE) were excited. The first direct measurements of the damping of TAE modes were carried out.

I. INTRODUCTION

In February 1994, after a 22 month shutdown for installation of the new 'Pumped Divertor', the Joint European Torus (JET)[1] has entered a new phase. The main elements of the pumped divertor configuration[2] are four divertor coils, wound inside the vacuum vessel, an internal cryogenic vacuum pump, and an inertially cooled divertor target structure.

The key objective of the new phase of JET is to demonstrate effective control of impurities by divertor action, both in 'steady-state' and in 'transient peak performance' regimes. The new installation serves this objective: the internal coils allow formation of diverted magnetic equilibria up to high plasma currents (design current is 6MA), the cryogenic pump allows the removal of particles, and the target structure is designed for a high heat load capability, in particular when X-point sweeping is applied.

The initial months of operation in the new configuration[3,4] revealed two important differences with the past. First, the new target structure has a strongly improved heat load capability. Carbon influxes (or blooms), resulting from local overheating of target tiles, were a common feature in past high power experiments. They have not been observed in the new configuration. Second, in the High confinement (H)-mode operation, a significant change in the behaviour of Edge Localised Modes (elms) was observed. In the past operation of JET in the H-mode - at low and medium densities - was characterised by long elm-free periods. At present elms appear soon after the transition from L to H-mode. Due to these elements the focus of the achievements of the past months has been on the 'quasi steady-state', elmy H-mode regime[5].

The elmy H-mode regime is at present considered the most credible candidate for operation of the International Thermonuclear Experimental Reactor (ITER)[6]. However, to be credible the regime needs to be compatible with a comprehensive set of requirements: acceptable confinement, sufficient helium ash removal, compatibility with detached divertor operation, etc. A demonstration of this viability is still lacking. Further development of the regime, integrated with detached divertor operation, and leading to a demonstration of its compatibility with reactor requirements, is a priority of the JET project.

The peak transient performance - achieved in the past with the Hot-ion H-mode and Very High confinement (VH)-mode - , has not yet been reproduced. The maximum Deuterium-Deuterium (D-D) neutron rate achieved so far in 1994 ($2.3\ 10^{16}$) is about half of that achieved in the past ($4.3\ 10^{16}$). A variety of factors is found to play a role; the shorter elm-free periods, the generally higher levels of operating density and recycling, and effects of plasma geometry which affect confinement and edge stability. A recovery, or preferably an improvement in the peak performance levels over the past is desirable before execution of further Deuterium-Tritium experiments. Hence, optimisation of the transient peak performance remains a priority issue[7].

Significant work has been done in the area of tokamak concept improvement[8]. This covers the general exploration of methods to affect confinement and stability by modifying the current density profile. The most important results are the extension of the regime of high bootstrap current to a quasi steady-state and to lower safety factors, and an initial experiment on the effects of shear reversal on the transport.

In section 2 the new configuration and the many upgraded and new systems are presented. In section 3 the differences in machine behaviour between the past and present, and their effects on confinement and performance are highlighted. In section 4 the work on long pulse elmy H-mode, on divertor detachment and on cryopump effects is discussed. In section 5 the work in the general area of tokamak concept improvement is shown. In section 6 the first experiments on external excitation of Toroidal Alfven Eigen-modes is presented. In section 7 a preview of the further JET programme is given, and in section 8 the main conclusions of the paper are summarised.

II. THE NEW CONFIGURATION

A. The pumped divertor

The new pumped divertor configuration of JET is shown in figure 1. There are four internal divertor coils. On these, the water-cooled support structure for the target tiles is mounted. The divertor target consists of Carbon Fibre Composite (CFC) tiles, with typical dimensions 35 x 80, depth 50mm. The fibres of the CFC are aligned perpendicular to the plasma facing surface, so as to have a high heat conductivity into the tile. Cooling of the tiles is by conduction and radiation to the structure, on a 'between shots' timescale.

The divertor cryopump has a pumping speed for deuterium of $170 m^3 s^{-1}$. Conductance from the scrape-off layer to the pump is via the slots between the divertor tiles. The pump is designed to pump Helium using the Argon frost technique.

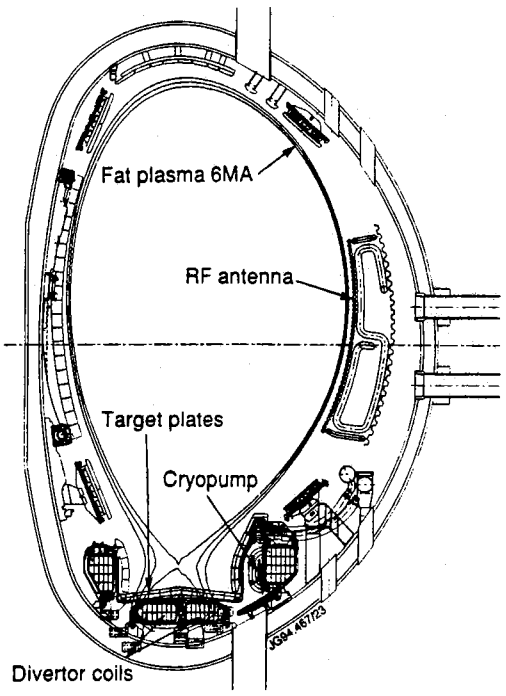

Fig.1 Poloidal cross-section of the JET pumped divertor configuration.

B. The additional Heating Systems

The Neutral Beam Injection (NBI) system has undergone minor modifications. The capability is about 20MW (in Deuterium), with half the injectors operating at 80keV and the other half at 140keV.

The Ion Cyclotron Resonance Heating (ICRH) system has been strongly modified, mainly in view of developing the Fast Wave Current Drive capability. There are four antennas containing four current-carrying straps each. The phase of each of the straps is controlled and adjustable, so that a directional Fast Wave can be launched. The design power capability is 20MW. At present, up to 12MW has been coupled to H-mode plasmas, and H-mode with ICRH alone has been achieved. The performance has been limited by technical problems. First, there have been several problems with the new low-power electronics. Second, a minor modification to cross-over straps inside the antennas is required.

The Lower Hybrid (LH) system has been upgraded to the full capability of 10MW installed power. Up to 6MW has been coupled to the plasma.

C. Other systems

Eight internal saddle coils were installed inside the vacuum vessel. These coils have a triple objective. First, to perform experiments on the stabilisation of the n=1, m=2 tearing mode. Second, to reduce error fields which can narrow the operational domain. Third, to study the active excitation and the damping of Toroidal Alfven Eigen-modes.

A new Fast Radial Field Amplifier for vertical position control has been installed. A new fully digital plasma current and shape control system now allows feedback control of selected geometrical entities, such as plasma to vessel distances, X-point position, and separatrix strike points on the target.

In addition to these 'active' systems, a large number of new diagnostics has been installed, in particular aimed at improving the measurement capability in the divertor.

III. PERFORMANCE OVERVIEW

A. Divertor heat load capability

The power handling capability of the new divertor is strongly improved with respect to the past. In discharges without X-point sweeping, and with 14MW of NBI power at medium density, tile surface temperatures of about 1000°C are reached about 4s after switch-on of the NBI, that is at an input energy of about 55MJ. This contrasts with the 10 to 15MJ input energy quoted in the past for obtaining peak tile surface temperatures in excess of 1200°C. Several elements are involved in this improvement: the shaping of tiles to avoid exposure of edges; the small installation tolerances, the orientation of the CFC fibres, and perhaps the spreading of power by the elms.

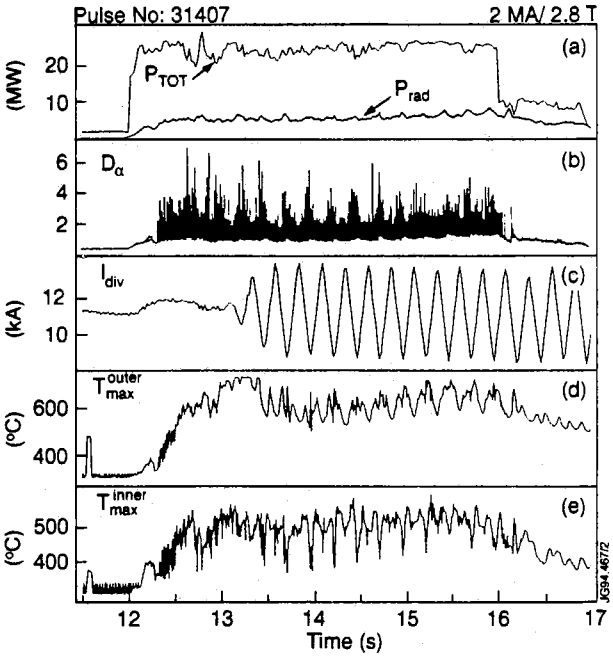

Fig.2 Time evolution of a discharge with 25MW of combined heating power for 4s. X-point sweeping is 100mm, starting at 13s, and is shown here by the current in one divertor coil. The bottom two traces shot maximum target tile surface temperature near outer and inner strike zone respectively.

With X-point sweeping, significantly higher input energies can be used. In figure 2 the time evolution is shown for a discharge with an input power of 24MW for 4s, in which the X-point is swept. The divertor tile surface temperature is seen to saturate at about 600°C. There is no evidence of impurity influxes.

B. Energy confinement scaling

The changes in the geometry of JET have an effect on the predicted energy confinement. Using the ITER89P L-mode scaling, the predicted confinement is lower by about 15% for the present configuration.

In figure 3 the confinement enhancement factors H_{ITER89}, that is the ratio of measured to predicted confinement, are shown for a selection of 1994 discharges in the elm-free phase. The value of H, typically around 2.3, has not changed significantly with respect to the past. However, VH performance[9], which in the past has led to higher enhancement factors, has not yet been reproduced.

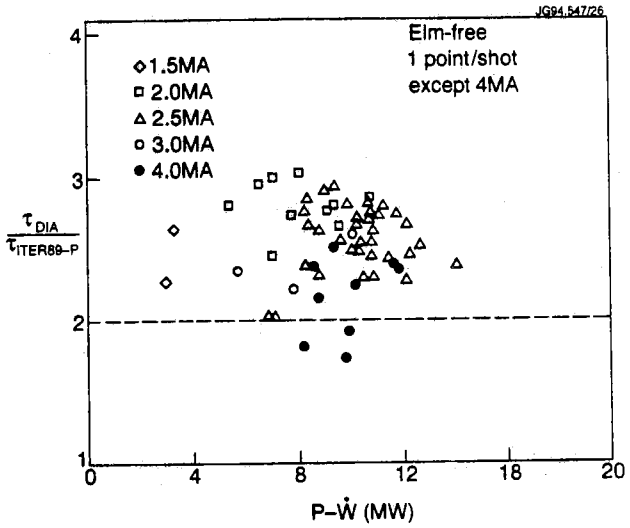

Fig.3 Confinement times, normalised to the ITER-89P scaling law prediction, for a selection of 1994 JET discharges in the elm-free phase.

Elmy H-mode data has now been obtained in a variety of conditions. Figure 4 shows normalised confinement times for a selection of the elmy data. The figure shows that the typical level of the enhancement factor is about H ≈ 1.9. The reduction in confinement, when operating in steady-state elmy conditions is thus of the order of 20% when compared to 'standard' elm-free H-mode, but is larger when compared to VH mode.

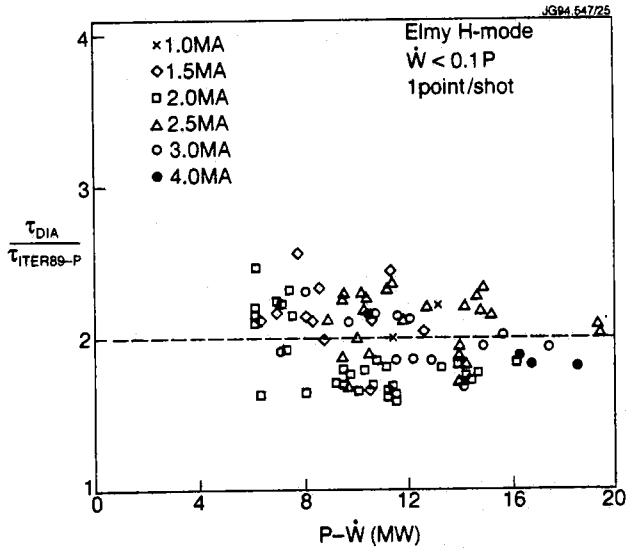

Fig.4 Confinement times, normalised to the ITER-89P scaling law prediction, for a selection of 1994 JET discharges in the elmy phase.

C. Operation at high plasma current

The maximum plasma current achieved so far is 4MA[7]. In figure 5 an overview is shown for a 4MA discharge with 15MW of additional heating. The safety factor q_{95} of this discharge is 2.8 at 3.4T. The maximum stored energy is about 9MJ. The fusion triple product $n_D T_{i0} \tau_E$ is about 4.9 10^{20} m^{-3} keV s during the transient elm-free phase, and drops to about 2.5 10^{20} m^{-3} keV s during the quasi steady elmy phase.

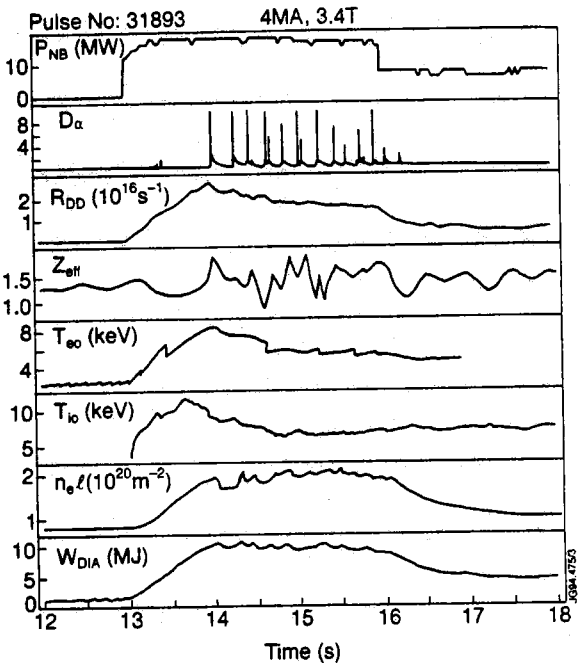

Fig.5 Traces for a 4MA discharge, showing both the elm-free phase (13.4 - 14s) and the elmy phase.

D. Performance optimisation

Short elm-free periods limit the peak fusion performance. Therefore, a large part of the work on performance optimisation has concentrated on attempts to increase the duration of the elm-free period. Two aspects have been addressed. First, the condition of the machine and the differences in operating temperature, hydrogenic inventory and target design with respect to the past. Second, the effects of the magnetic configuration.

Several experiments were carried out to address the possible effect of the target. As a result of these, it appears now unlikely that details of target design, target temperature or target outgassing are the cause of the increased elminess.

The D-D neutron rate, for discharges with similar parameters, has been significantly improved by the use of the divertor cryopump. With the cryopump, the NBI particle source is dominant over the recycling particle source. Then, the peaked density profiles, for which NBI penetration is favourable, are established.

IV. DIVERTOR REGIMES AND CRYOPUMP

A. Long pulse elmy H-mode

The high heat load capability of the divertor has allowed quasi steady-state elmy H-modes of 20s duration to be obtained[5]. In figure 6 traces are shown of one of these discharges with about 7MW NBI input power. During the H-mode, plasma fuelling was by NBI alone. The divertor cryopump was used for control of the density. With the crypump, no saturation effect of the

pumping was experienced. This contrasts with old results on long pulse elmy H-mode, where the wall pumping saturated after about 10s, and where no true steady-state could be achieved as regards fuelling.

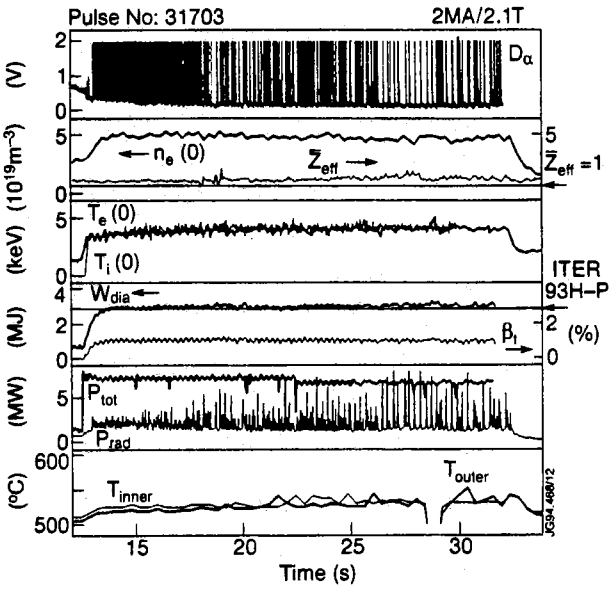

Fig.6 Traces for a steady-state elmy H-mode discharge with a duration of 20s. The bottom trace shows the maximum surface temperature of the divertor target near the inner and outer strike zones respectively.

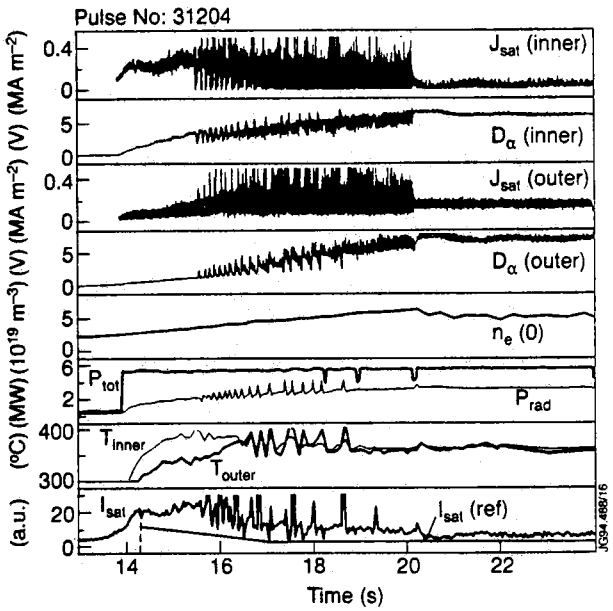

Fig.7 Traces for an L-mode discharge in which divertor detachment is obtained at 20s. In the phase prior to detachment (15 - 20s), a divertor instability is observed.

B. Detached divertor plasmas

In figure 7 traces are shown for a discharge in which detachment is achieved for a Low confinement (L) mode plasma at a power level of 5.5MW[5]. In this scenario, the gas input is controlled by feedback from the ion saturation current of one of the Langmuir probes close to the inner target. We observe the gradual drop of I_{sat} between 16 and 20s, while the density is increasing. A reduction of the pressure at the probe is obtained while the total radiated power is of the order of 50%. Prior to detachment, - 15 to 20s - a divertor instability is observed.

Attempts to achieve similar detachment in H-mode plasma have so far failed. The H-mode returned to L-mode, before detachment was observed.

C. Pumping effects with the cryopump

An experiment was carried out to investigate the dependence of the particle removal rate on the X-point geometry[5]. In this experiment the outer strike zone was moved over the horizontal target plate and up the vertical plate, while the pressure in front of the pump was monitored. The result is shown in figure 8. A maximum particle removal rate of 8.0 10^{21} was reached as

the outer strike zone aligned with a toroidal slot in front of the pump. The removal rate is reduced when the strike zone is moved away from this position. The variation is about a factor two, indicating a good conductance to the pump through the radial slots between target tiles for strike zone locations away from the pump.

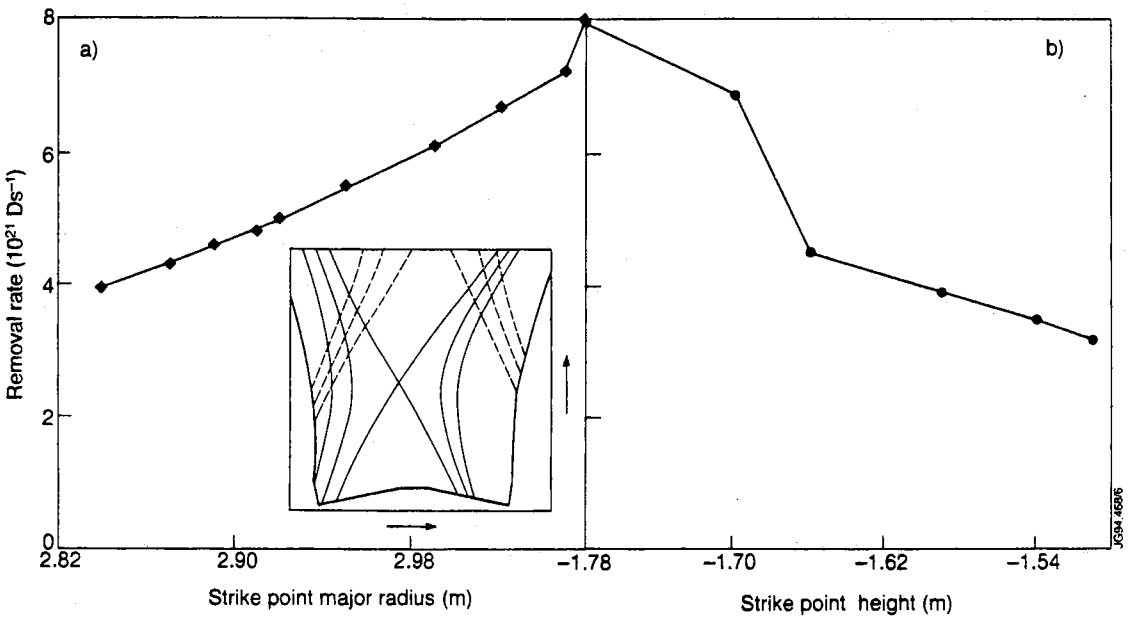

Fig.8 The measured particle removal rate as a function of the outer strike zone position. The removal rate is shown as the outer strike zone is swept across the horizontal target plate (left of the figure), and upwards on the vertical target plate (right of the figure).

V. TOKAMAK CONCEPT IMPROVEMENT

A. The high poloidal beta regime

The present experiments have concentrated on extending the existing results in this regime[10] into quasi steady-state, making use of the frequent elms. Further, on extending it to lower q_{95}, and higher normalised beta β_N. In figure 9 a discharge is shown in which $\beta_P = 2.6$ is obtained in transient in a 1MA, 2.8T, and β_P is maintained above 1.5 for a duration of 3s. In discharges with a toroidal field of 1.4T, a value of $\beta_P = 1.6$, with $\beta_N = 3$, were maintained simultaneously for 7s.

In figure 10 values of the achieved β_P, β_N and q_{95} are shown in relation to the values required for a typical advanced tokamak reactor operating scenario. A distinction is made between transient points and points for which the values are maintained for at least 3s. While the 3s criterion does not define a steady-state as regards current diffusion, it does establish a sufficient energy balance steady-state.

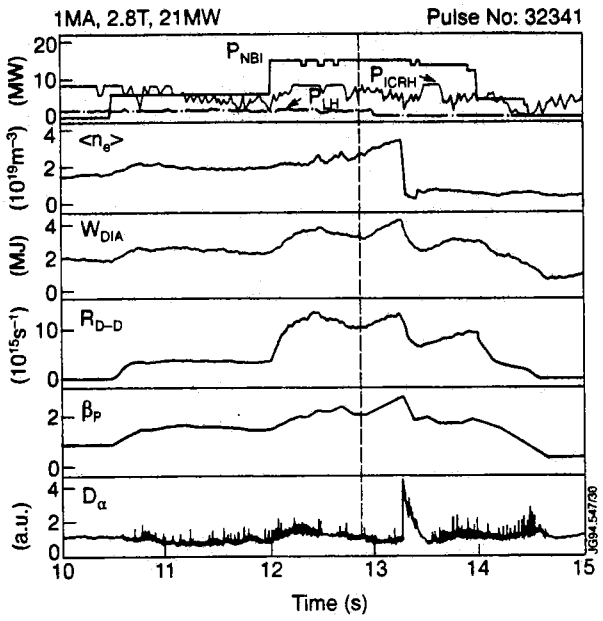

Fig.9 Traces for a discharge with a transient value of β_P of 2.6±0.2. With 21MW of combined heating power, an elmy H-mode is established. At 12.8s, there is a sudden transition to a transient phase of improved confinement, which is terminated by a large elm.

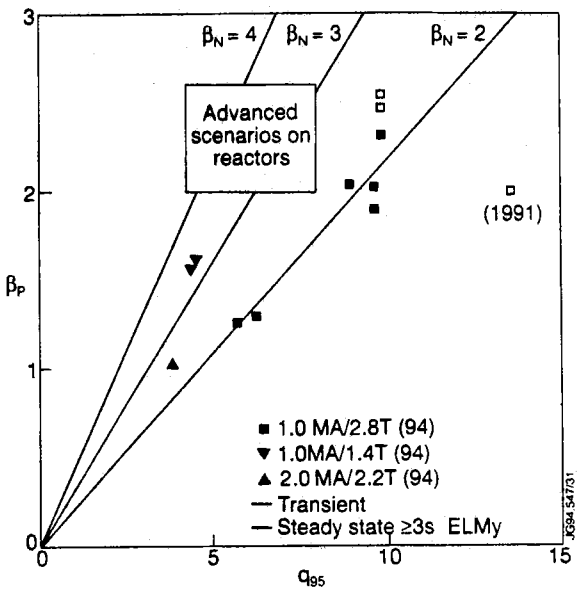

Fig.10 The JET data on the high β_P regime in a diagram of β_P versus q_{95}. Open symbols represent transient data. Closed symbols represent shots which maintain the value of β_P for at least 3s.

B. Shear reversal

Configurations with reversed magnetic shear have been produced by additional heating with LH, ICRH and NBI as early as possible in the current rise. This increases the current penetration time. In figure 11 traces are shown for a typical 'shear-reversal' shot. The plasma is initiated by a low voltage breakdown, and plasma current takes off at 0.3s. The X-point configuration is fully formed at 0.9s. NBI heating is started at 2.5s, resulting in an elmy H-mode, which persists throughout the entire discharge phase. The equilibrium code indicates shear reversal between about 2 and 6s. A time sequence of q profiles is shown in figure 12.

During the NBI heated phase it is observed that the energy confinement time and the D-D neutron rate, increase constantly with time while the internal inductance l_i increases. The enhancement factor H_{ITER89} is about 1.1 at 3s at $l_i = 0.5$, and increases to about 1.5 at 9s at $l_i = 0.7$. In a reference shot with a 'normal' $l_i = 0.95$, a the normal H factor for elmy H-mode H = 1.9 is found. These findings are consistent with the observations on several machines that energy confinement time scales with internal inductance, to a power of order unity.

Hence, during the elmy H-mode phase, no evidence of improved confinement due to shear reversal could be found. During the preceding L-mode phase, before 2s, there is some evidence

for improved confinement. However, simultaneously, there is evidence for a fast electron population, driven by the LH. This issue needs further analysis.

Although these experiments are not yet conclusive, they do appear to set practical boundary conditions on the types of current density profiles that may lead to reduction of the anomalous transport.

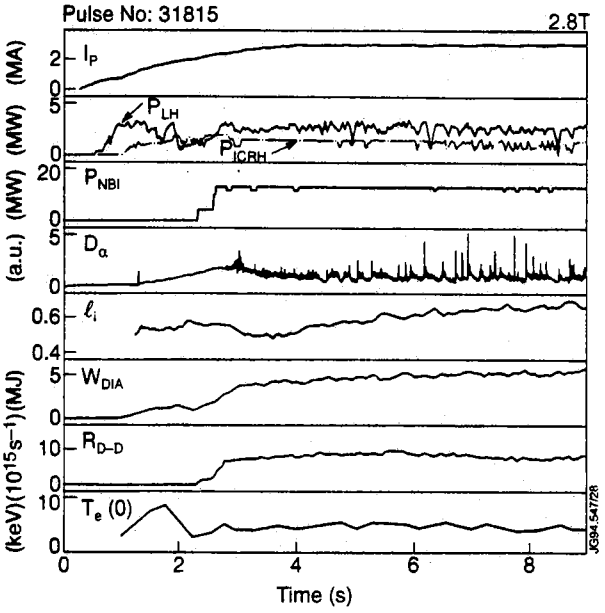

Fig.11 Traces of a shot in which a shear reversed configuration is established. The X-point configuration is established at 0.9s.

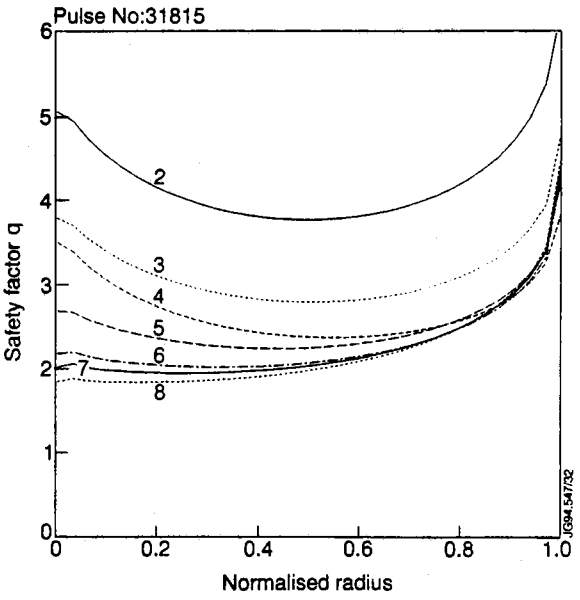

Fig.12 A series of q profiles, reconstructed by the equilibrium code, for the shear reversal shot shown in figure 11.

VI. T.A.E. MODE DAMPING

The first experiments were carried out in which Alfven Eigen-modes were externally excited. This was done with the saddle coils, driven by a high frequency amplifier of 3kW power capability. In ohmic plasmas, resonances have been clearly observed. The Alfven nature of the resonances was verified by executing a scan in toroidal field, and comparing the measured resonance frequency with the calculated TAE frequency. Damping rates of the mode between 0.1 and 0.01 are measured, depending on the density profile. These damping rates are consistent with the predicted presence and absence of continuum damping.

VII. THE FUTURE PROGRAMME

The present JET campaign is scheduled to May 1995. Important elements of the remainder of the campaign are: the extension of X-point operation to 5or 6MA; the further exploration of the detached divertor regime and its compatibility with elmy H-mode operation; a study of Helium transport and pumping using the Argon frosting facility of the cryopump; further studies of

effects of current density profile modifications; a number of specific ITER relevant experiments, such as: an experiment on toroidal field ripple; an H-mode threshold experiment and an experiment on the issue of scaling of the transport with gyro-radius. Finally, the present CFC divertor target tiles will be exchanged for a set of Beryllium tiles in order to study the differences between these materials as plasma-facing components.

An extension of the JET programme to the end of 1999 is proposed. A new divertor, called Mark-2, will be introduced in 1995. This will provide a more closed divertor geometry. Mark-2 will feature a large carbon plates as opposed to the present system of many small tiles. The Mark-2 mechanical support structure is designed to accommodate a variety of possible top structures and target plate designs. A period of D-T experiments is planned for the end of 1996. After this, it is planned to construct a strongly ITER relevant 'Gas-Box' divertor, on the same Mark-2 support structure. A final D-T phase is planned for 1999.

VIII. DISCUSSION

The initial operational phase of JET in its pumped divertor configuration has made evident the increased power handling capability of the divertor and the more frequent occurrence of elms. Significant progress has been made in the extension of the H-mode operation to the reactor relevant steady-state elmy H-mode. This regime is now obtained in a variety of conditions, in particular at plasma currents ranging from 1 to 4MA, power levels ranging from a few to 26MW, in the high β_P regime, in discharges with shear reversal, and at high normalised beta. The next milestone in showing the reactor relevance of this regime will be the demonstration of the compatibility of high confinement operation with detached divertor operation, which has not been successful so far. This demonstration may, in fact, require the closed divertor structure planned for the JET extension.

The cryopump allows effective particle removal. The use of it improves vacuum conditions, reduces recycling, allows generally higher performance operation. In the long pulse elmy H-mode regime, the cryopump eliminates the effects of wall saturation that were observed in earlier experiments.

The experiments on optimisation of the JET transient peak fusion performance have not yet resulted in an improvement over the past. Various factors play a role in this; the increased elminess, the change of the plasma geometry, the generally higher operating densities, and the higher recycling. This area will be pursued in the remainder of the campaign.

The regime of high poloidal beta operation has been extended to steady-state, at least as far as the power balance is concerned. Initial experiments on the effects of shear reversal have not yet led to the observation of confinement enhancements, in discharges where the magnetic analysis shows the existence of shear reversal.

ACKNOWLEDGEMENTS

The results reported in this paper would not have been possible without the sustained efforts of the staff in the technical divisions who designed and built the many modifications to the JET machine, and who support the operation.

REFERENCES

1 P. H. Rebut, B. E. Keen, Fusion Technol. **11**, 1 (1987).

2 E. Bertolini, and JET Team, 'JET with a pumped divertor', Fusion Eng and Design (proc. 18'th SOFT conference, Karlsruhe, 1994) to be published for the Commission of the European Communities, Brussels, Belgium.

3 A. Tanga and JET Team, 'First results with the modified JET', Plasma Phys. and Contr. Fusion (proc. 21'st Eur. Conf., Montpellier, 1994) to be published by the Institute of Physics Publishing, Bristol, UK.

4 D. Stork and JET Team, Plasma Phys. and Contr. Nuc. Fus. Res. (proc. 15'th IAEA conf., Seville, October 1994, paper IAEA-CN-60/A-1-I-3) to be published by the International Atomic Energy Agency, Vienna, Austria.

5 D. J. Campbell and JET Team, ibidem, paper IAEA-CN-60/A-4-I-4.

6 P.H. Rebut, V. Chuyanov, M. Huguet, R. Parker, Y. Shimomura and the ITER Joint Central Team and Home Teams, ibidem, paper IAEA-CN-60/E-1-I-1.

7 P. J. Lomas and JET Team, ibidem, paper IAEA-CN-60/A-2-I-4.

8 C. Gormezano and JET Team, ibidem, paper IAEA-CN-60/A-2-I-4.

9 R. Gianella, and JET Team, ibidem, paper IAEA-CN-60/A-2-III-1.

10 C. D. Challis, T.C. Hender, J. O'Rourke, S. Ali-Arshad, B. Alper, H.J. de Blank, N. Deliyanakis, C.G. Gimblet, J. Han, J. Jacquinot, G.J. Kramer, W. Kerner, D.P. O'Brien, P. Smeulders, M.F. Stamp, D. Stork, P.M. Stubberfield, D.D.R. Summers, F. Tibone, B.J.D. Tubbing, W. Zwingmann, Nuclear Fusion **33** (1993) 1097.

Power Deposition and Driven Current Profiles in Lower Hybrid Current Drive Experiments on JET

Y F Baranov, A Ekedahl, B Fischer, P Froissard,
C Gormezano, M Lennholm, F Rimini, F X Söldner.

JET Joint Undertaking, Abingdon, Oxfordshire, OX14 3EA, UK.

Power Deposition and Driven Current Profiles in Lower Hybrid Current Drive Experiments on JET

Y F Baranov, A Ekedahl, B Fischer, P Froissard, C Gormezano, M Lennholm, F Rimini, F X Söldner.
JET Joint Undertaking, Abingdon, Oxfordshire, OX14 3EA, UK.

SUMMARY.

High performance and reliability of the new Lower Hybrid Current Drive (LHCD) system has been demonstrated in the recent experiments on JET in divertor discharges. The system operates at a frequency 3.7GHz with the maximum power of 12MW (20s). Up to 6MW of LH power was launched into the plasma through a single multiple waveguide grill type antenna. Nearly full current drive of Ip=2MA was achieved in the plasma with $n_e(0) \cong 2.3\ 10^{19} m^{-3}$ by launching about 4MW of LH power during 3.5s. The electron temperature increased from 3keV up to about 5keV during current drive phase. The LHCD experiments have been modelled by means of code [1]. It includes ray-tracing in the toroidal geometry with the real divertor configuration and 2-D Fokker Planck calculations. Scattering of the lower hybrid waves on density fluctuations and spatial diffusion of the fast electrons with the diffusion coefficient $D=D_0 v_{//}/v_e$ ($D_0=0.5 m^2/s$, $v_{//}$ and v_e, parallel and thermal electron velocities) are taken into account. Results of the modelling are in good agreement with the experimentally observed LHCD efficiency [2]. Simulated fast electron bremstrahlung (FEB) emission is compared with the measured FEB profiles [3] for a number of shots. The deposition profile varies with plasma density, temperature, and plasma current.

2MA CURRENT DRIVE EXPERIMENTS.

Discharge with nearly full plasma current driven by LH waves. Calculated by LHCD code $I_{LH}=1.86MA$ and efficiency $\eta=0.22*10^{20}(A*m^{-2}W^{-1})$. It is very close to the estimation from the change of the loop voltage and plasma resistance.

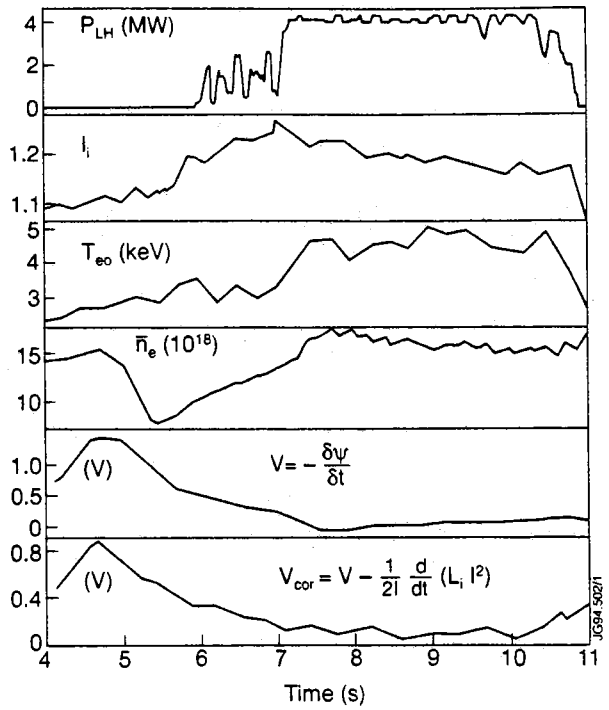

Fig. 1. Shot #29711. with I_p=2MA, n(0)≅2.3 $10^{19}m^{-3}$, at B_t=2.8T. Evolution of LH power (a), internal inductance (b), central electron temperature (c), line averaged density (d), flux consumption (e), smoothed over 0.5s measured and corrected loop voltages (f).

BROADENING OF LH DRIVEN CURRENT PROFILE WITH DENSITY INCREASE.

Current and power deposition profiles broaden when density increases while electron temperature does not change significantly in a greater part of the plasma volume.

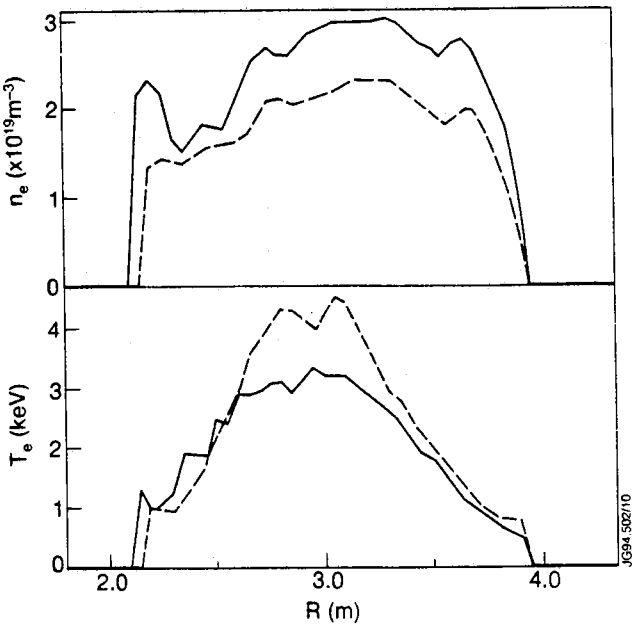

Fig. 2 Electron density (a) and temperature profiles (b) for shots #29711 and #29639. I_p=2MA, B_t=2.8T.

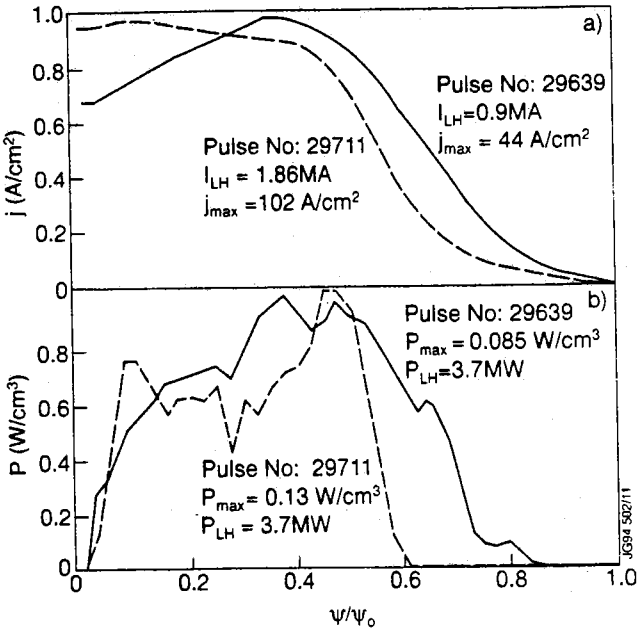

Fig. 3. Calculated driven current (a) and power deposition (b) profiles. Solid line-#29639, dashed line- shot #29711

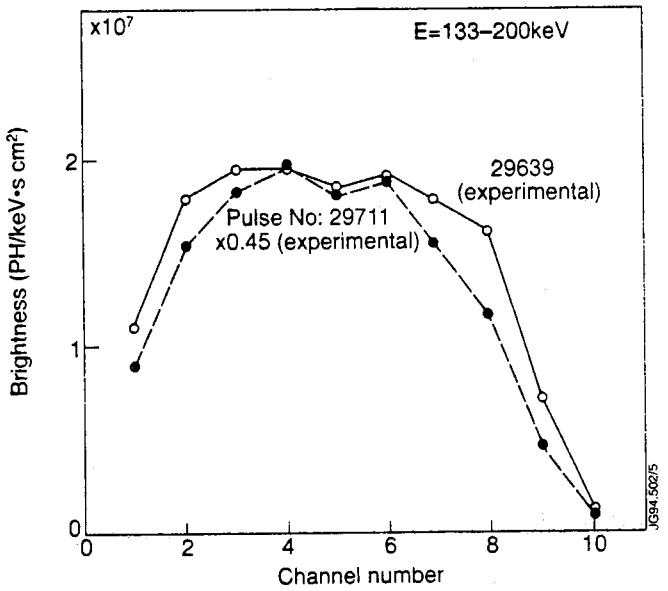

Fig. 4. Comparison of measured FEB profiles for shot #29639 (solid line) and #29711 (dashed line, this profile normalised by a factor 0.45).

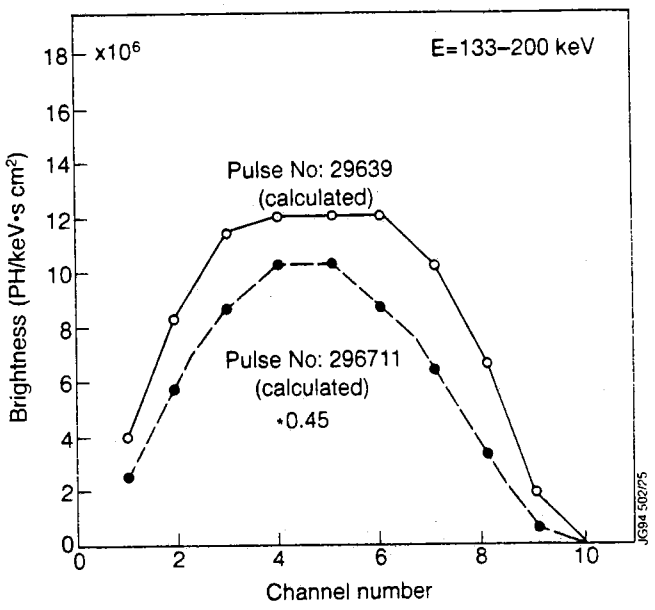

Fig.5. Comparison of calculated FEB profiles for shot #29711 (dashed line, this profile is normalised by a factor 0.45). The discrepancy in the calculated and measured brightness may be caused by uncertainty in $Z_{eff}(r)$ and error in the estimation of the average perpendicular electron energy of the tail $E_\perp(v)$ [1].

In the framework of the model the broadening of the profile is explained in the following way: at high density plasma the LH waves propagate closer to the periphery, where RF energy density (quasi linear diffusion coefficient $D_{ql)}$ increases. Ray trajectories experience greater number of reflections.

When reflection occurs in the top sector of the plasma boundary, the wave is strongly slowed down. This is the major mechanism for the 'spectral gap' filling. Higher power is absorbed and greater current is driven further out from the centre, (due to the higher value of D_{ql}) than in lower density plasma (under the condition that electron temperatures are not too different).

BROADENING OF THE LH CURRENT PROFILE WITH PLASMA CURRENT INCREASE

Comparison of experimental data shows that the LH driven current profile is systematically broader in discharges with higher plasma current. Calculation of ray trajectories (Fig.14) indicates that waves experience a greater number of reflections and spend more time in the peripheral region in the case of higher plasma current. Result is similar to the increase of plasma density (see above).

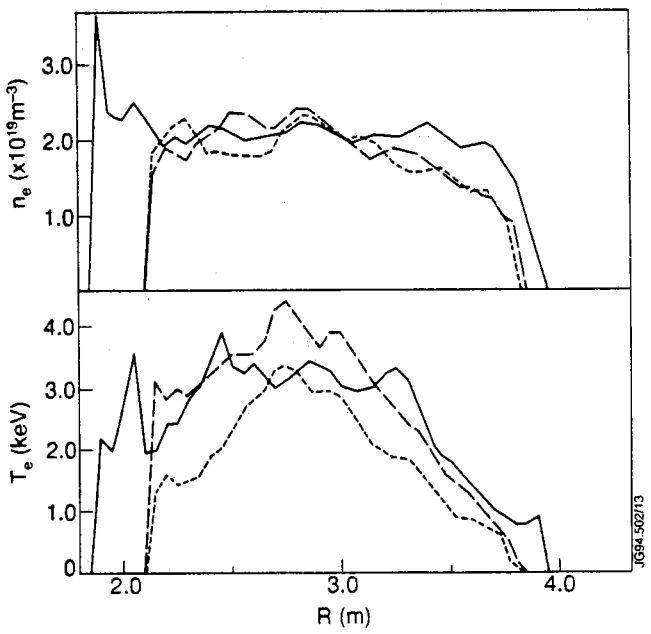

Fig. 6. Density and temperature profile for shots #30505 (solid line), #30542 (dashed line) and #30649 (dotted line)

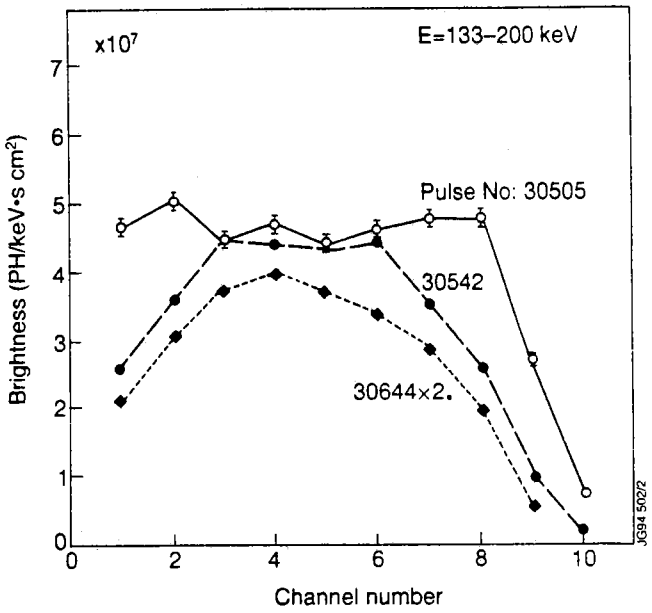

Fig. 7 Comparison of measured FEB profiles for pulses with different plasma current: -shot #30505, Ip=3MA, P_{LH}=4.6MW-(dashed line), and shot #30644, Ip=1.5MA, P_{LH}=1.9MW-(dotted line)

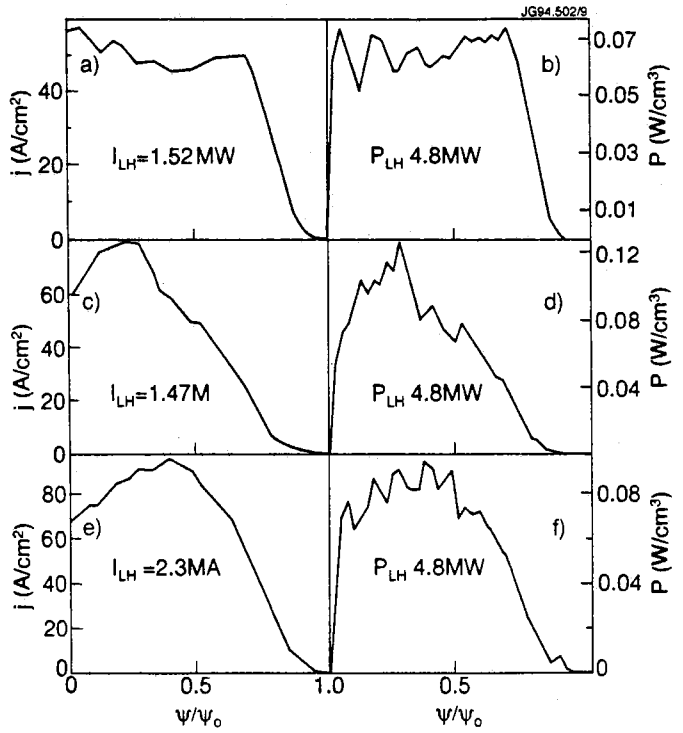

Fig. 8 Calculated LH current (a) and power deposition (b) profiles for shot #30505. Calculated LH current (c) and power deposition (d) profiles with equilibrium from shot #30542, and plasma parameters from shot #30505. Calculated LH current (d) and power deposition (f) profiles with equilibrium from shot #30505 and plasma parameters from shot #30542.

TRANSPORT CODE MODELLING OF LHCD

Evolution of the full current and l_i was simulated with the transport code JETTO taking into account the driven current, calculated by the LHCD code. In most shots with high LH power internal inductance l_i decreases and current profile broadens. This indicates off axis power deposition. Simulations reproduce the broadening of current profile and the decrease of l_i.

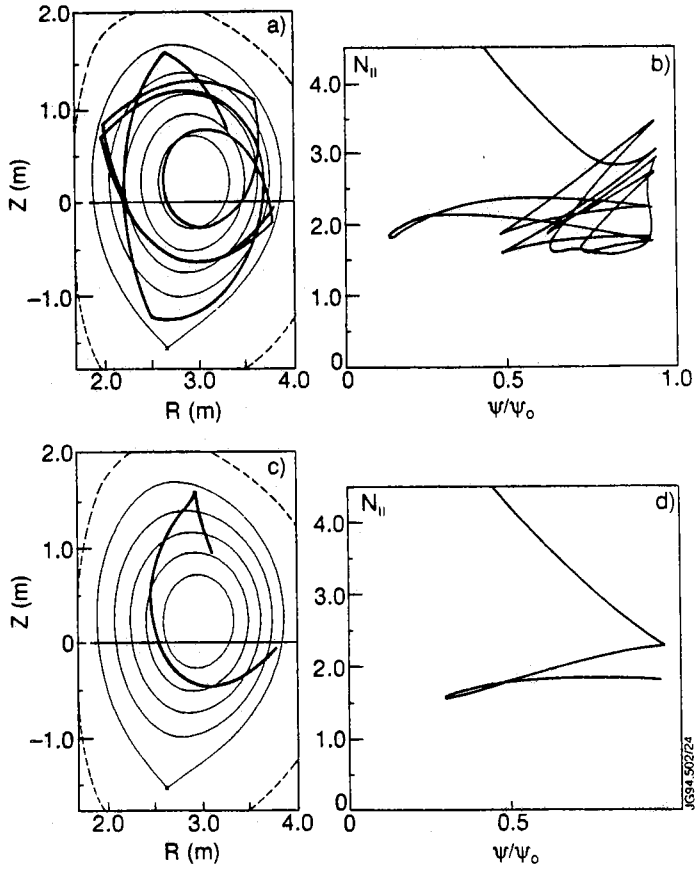

Fig. 9. Ray trajectories (a),(c) and behaviour of $N_{//}$ along trajectories as a function of poloidal magnetic flux (b),(d) for shots #30505 and #30542, respectively. Initial $N_{//}$=1.85

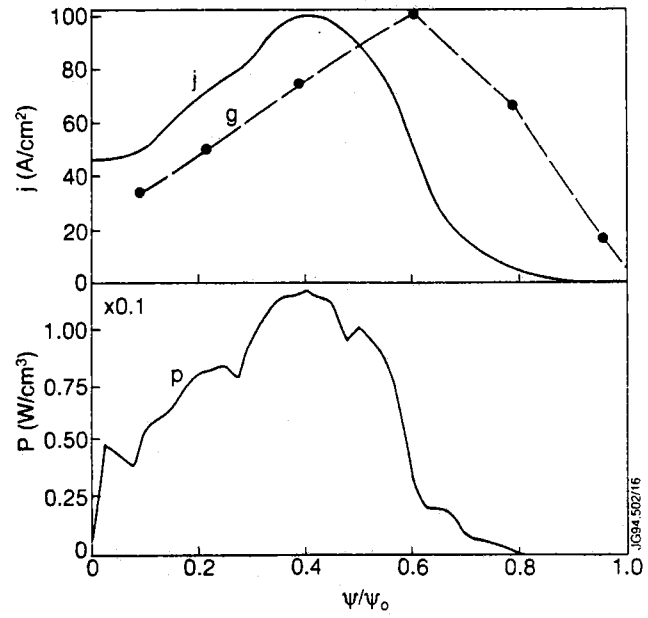

*Fig. 10. Calculated LH driven current j and power deposition profiles p and ratio g of the local FEB emissivity and electron density for shot #30517, t=57s, P_{LH}=4.5MW, $\overline{n_e}$ =1.6*10^{19} m^{-3}, n_{eo}=1.9*10^{19}m^{-3}, T_{eo}=3.5keV, $N_{//max}$=1.85, I_p=3MA, B_t=2.8T. Function g is calculated by Abel inversion of the measured chord integrated FEB profile (see Fig. 11). In our simple model g should be proportional to the number of suprathermal electrons.*

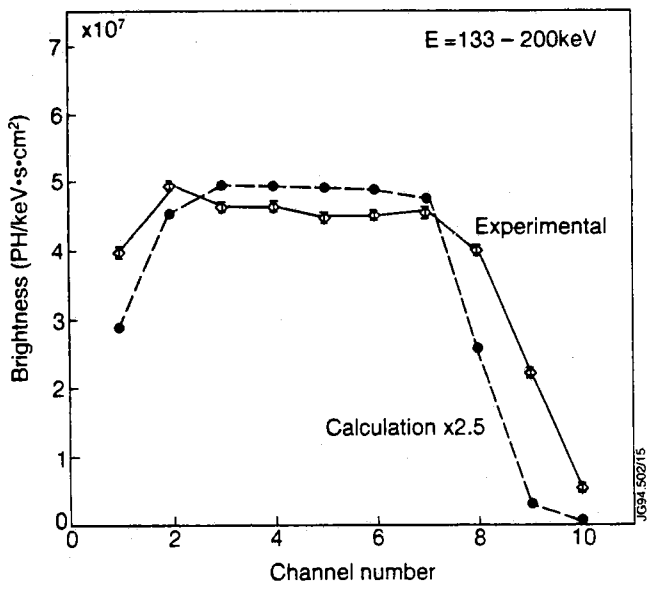

Fig. 11. Comparison of measured and calculated FEB profiles for shot #30517 (calculated signal multiplied by factor 2.5). Discrepancy in the amplitude and form of the profiles may be attributed to the same factors as in Fig.4 and Fig.5..

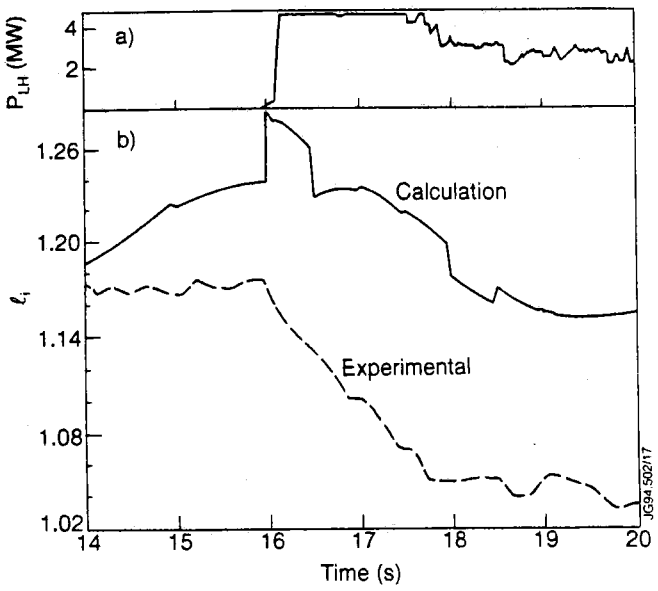

Fig. 12 Comparison of measured and calculated FEB profiles for shot #31753 at t=41.5s

VARIATION OF LH POWER SPECTRUM

Two spectra with different $N_{//max}$= 1.4 and 2.3 and equal full width $\Delta N_{//FW}$=0.46 were launched into plasmas with similar parameters. The FEB profiles for both spectra have a similar shape. Simulation roughly reproduces the similarity of LH drive current and power deposition profiles. Calculations show that in the case of relatively high density $n_{eo}=2.9*10^{19}m^{-3}$ and moderate temperature T_{eo}<2.5keV multiple pass absorption takes place. Initial spectra are modified considerably in the plasma in both cases.

Comparison of shots with different antenna phasing (parameters change with time in the indicated range):

#29548,
$$P_{LH} = 2.7 - 3.1MW,\ \overline{n_e} = 2.3^{*}10^{19}m^{-3}, n_{eo} = 2.9^{*}10^{19}m^{-3},$$
$$T_{eo} = 2.2 - 2.6keV, N_{//\max} = 1.4,\ I_p = 2MA, B_t = 2.8T$$

#29549,
$$P_{LH} = 1.8 - 3.2MW,\ \overline{n}_e = 2.3*10^{19}m^{-2},\ n_{eo} = 2.9*10^{19}m^{-3},$$
$$T_{eo} = 2.2 - 2.6keV, N_{ll\ max} = 2.3,\ I_p = 2MA$$

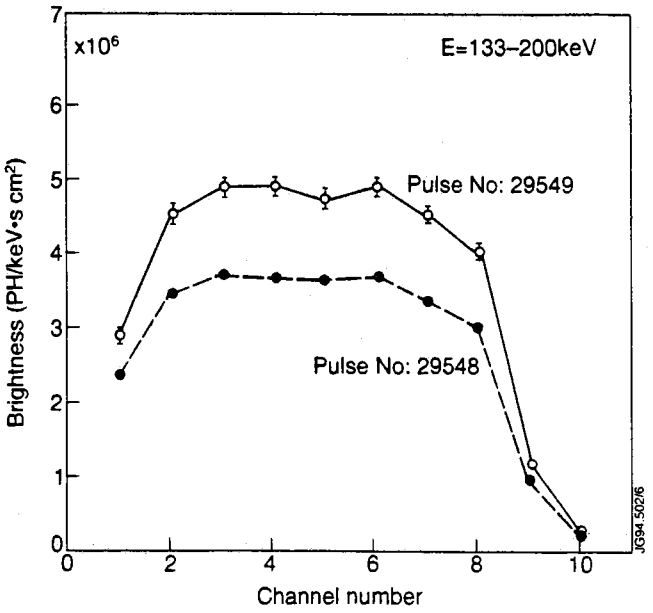

Fig.13. Measured FEB profiles: crosses-shot #29548, bars-shot #29549.

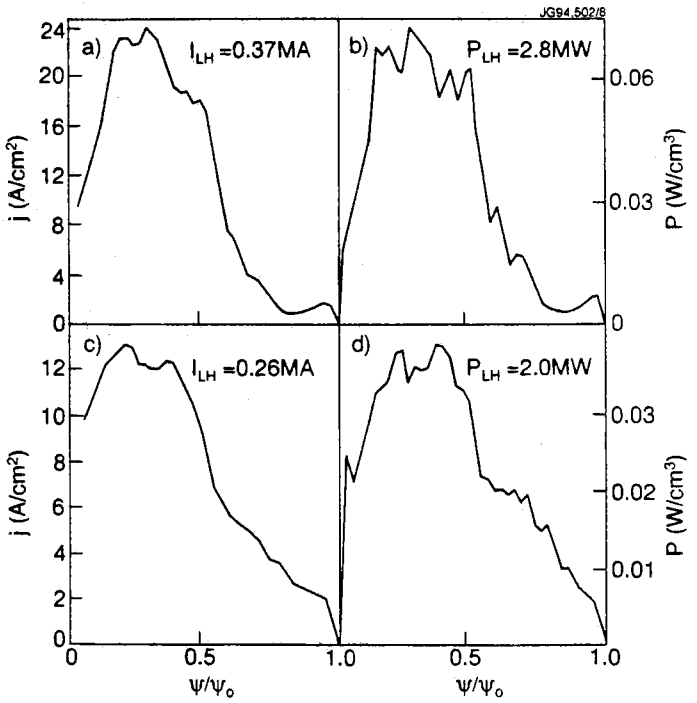

Fig.14. Calculated current (a), (c) and power deposition (b), (d) profiles for shots #29548, #29549, respectively. Calculated $\eta=0.085*10^{20}(A*m^{-2}/W$ for both shots

CONCLUSION.

High versatility of LHCD was demonstrated in experiments on JET. Full current drive as well as considerable modification of plasma current shape for the purpose of profile control have been achieved. Experiments were carried out in a wide range of plasma parameters; n_{eo}=(0.9-4.0)*$10^{19}m^{-3}$, T_{eo}=1.5-6.keV, I_p=0.5-3MA, B_t=2.4-2.8T with maximum available LH power of 6MW and different power spectra $N_{//max}$=1.4,1.85,2.3 with LH alone and in combination with NBI and ICRH. Results of modelling by LHCD and transport (JETTO) code are in qualitative agreement with experimental data. Calculations show that in most analysed cases multiple pass absorption of LH waves takes place. Reflection of the waves as well as the process of the wave scattering requires additional investigation. When plasma temperature increases the number of reflections decreases. Extrapolation to high temperature plasma of ITER shows that LH waves should be absorbed during the first pass. Under such conditions predictions of the LHCD code are more reliable.

REFERENCES

1. Y.F.Baranov et al, 20th EPS Conf.Proc., Lisbon 1993, part 3, p.881
2. F Söldner et al., 15th Int. Conf. on Plasma Phys. and Control. Nucl.Fusion, Madrid, 1994, IAEA-CN-60/A-3-1-2.
3. P.Froissard, et al, 18th EPS Conf. Proc., Berlin 1991, part 3, p.389

Li-Beam Measurements of Edge Electron Density and Impurity on JET

P Breger, D Summers, Z A Pietrzyk[1], B Viaccoz, J Vince.

JET Joint Undertaking, Abingdon, Oxfordshire, OX14 3EA, UK.
[1] CRPP, Lausanne, Switzerland.

Li-Beam Measurements of Edge Electron Density and Impurity on JET

P Breger, D Summers, Z A Pietrzyk[1], B Viaccoz, J Vince.
JET Joint Undertaking, Abingdon, Oxfordshire, OX14 3EA, UK.
[1] CRPP, Lausanne, Switzerland.

INTRODUCTION

A Li-beam edge diagnostic has been implemented on JET. Employing a multifibre array and fast CCD cameras, beam emission and charge-exchange emission profiles can be obtained with high spatial and temporal resolution. Spectral resolution of the emission using spectrometers allows separate analysis of the various intrinsic plasma edge emissions in addition to the beam induced radiation. A new density de-convolution method has been developed to enable reconstruction of the density profile.

DIAGNOSTIC LAYOUT

A 60 keV mono-energetic beam of neutral Li atoms is injected into the top edge region of the JET plasma near the stagnation point. An observation periscope is employed to monitor radiation emitted from a 17 cm section of the beam trajectory in the range 1.4 m to 1.85 m above the torus midplane. This is imaged onto a multi-fibre array (53 optical fibres, 1mm core diameter). The spatial resolution obtained is of order 4 to 7mm in radial direction. The density fall-off length in this region is of order 50 mm. The light is transported back to a diagnostic hall via fibres, where it is spectrally resolved and recorded by CCD detectors.

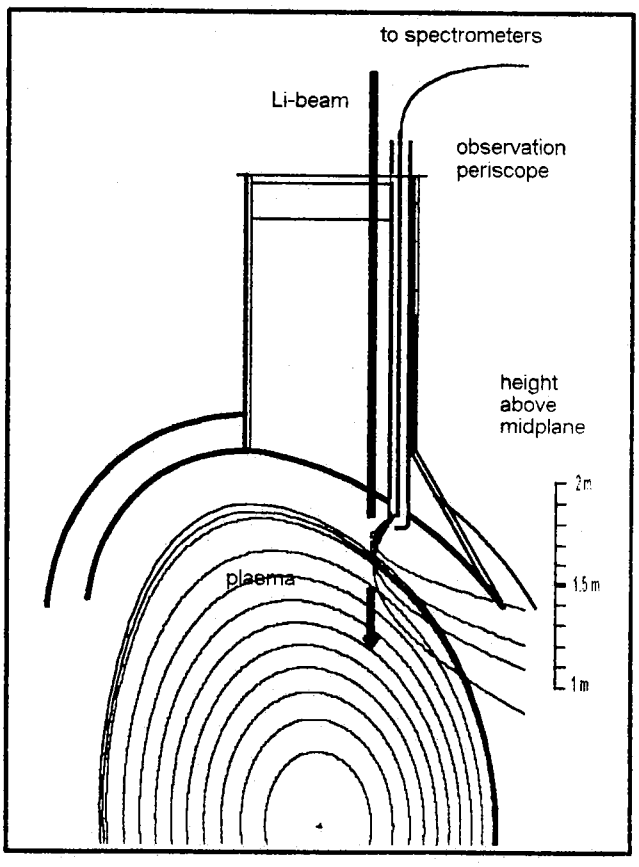

Fig. 1: Diagnostic Layout

ION SOURCE

The ion source electrode geometry (Fig. 2) is based on a modified Wehnelt extraction system [1], which has been optimised for JET using the source simulation code IONTRAK [2]. A Spectra-Mat emitter assembly (∅ 15 mm) is coated with ceramic β-Eucryptite ($Li_2O\ Al_2O_3\ 2(SiO_2)$). The extracted and focussed Li ion beam is neutralised in Li vapour. For commissioning purposes a Faraday cup can be inserted into the beam path at a distance of about 2m from the source. The operating voltages (extraction and acceleration), the emitter heating current and neutraliser temperature are optimised to yield maximum neutral beam intensity (see Fig. 3).

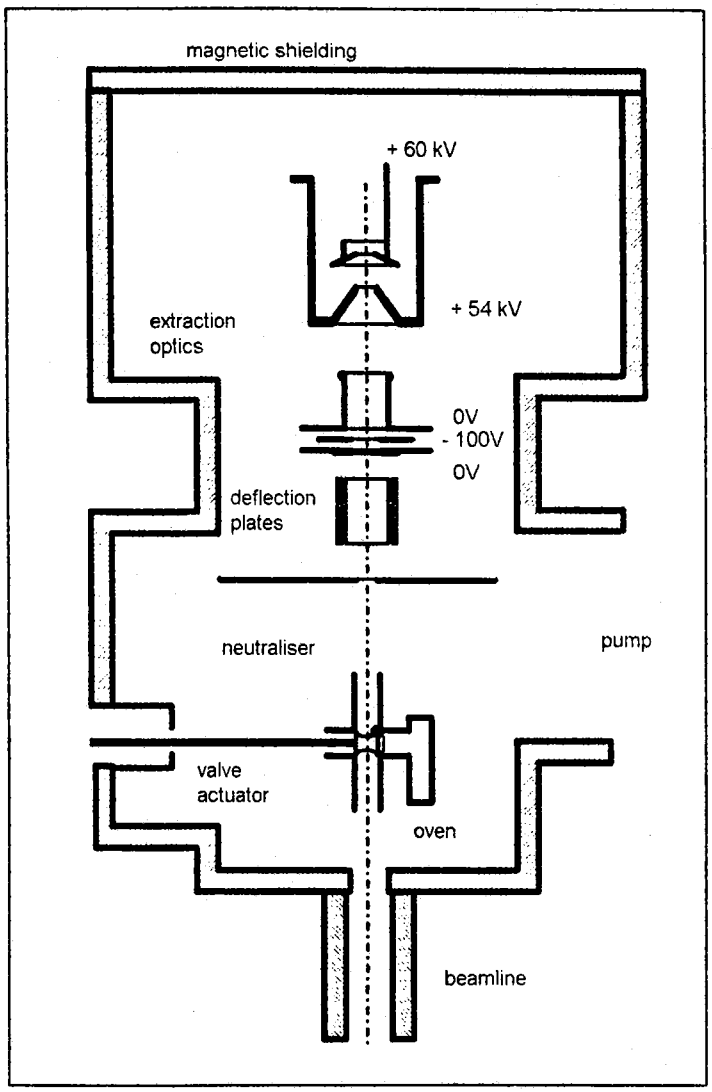

Fig. 2: Ion Source Setup

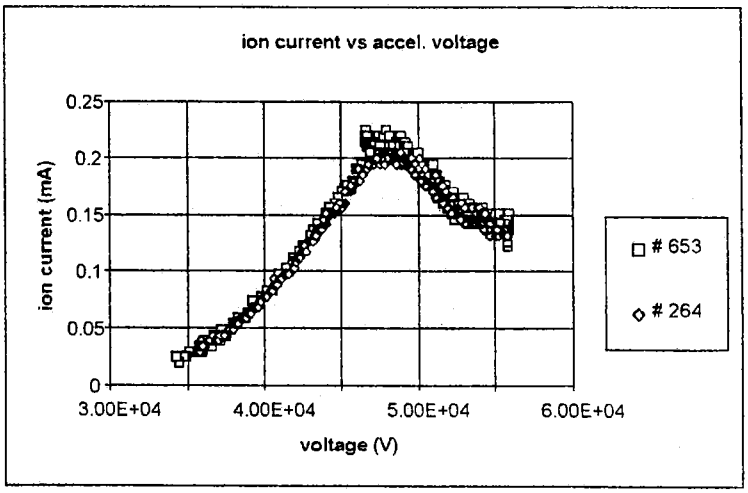

Fig. 3a: Optimisation of extracted ion current as function of acceleration voltage

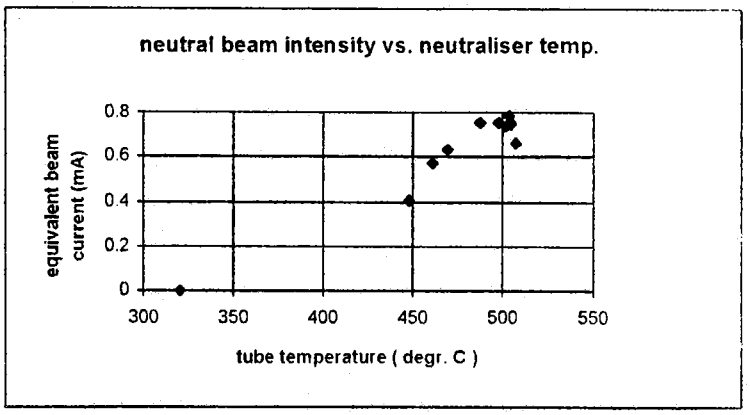

Fig. 3b: Beam current optimisation with respect to neutraliser temperature

SPECTRAL ANALYSIS

53 optical fibres relay the light from the beam path to a diagnostic hall outside the biological shield. Four fibres are arranged to view the plasma next to the beam. These are used primarily for alignment purposes, but can also be used as a monitor of passive radiation from the plasma. 44 of the 53 fibres are imaged on the entrance slit of an astigmatism-corrected low-resolution spectrometer (0.27 m Chromex) to separate the resonance beam emission at 670nm from the parasitic plasma background radiation. The resultant spatial profile of the beam emission can then be de-convoluted to obtain the **electron density profile** along the beam trajectory.

The remaining five beam monitoring fibres are passed to a high resolution spectrometer (1.25m SPEX) to enable analysis of the beam induced impurity radiation (charge-exchange radiation) for **impurity density determination**.

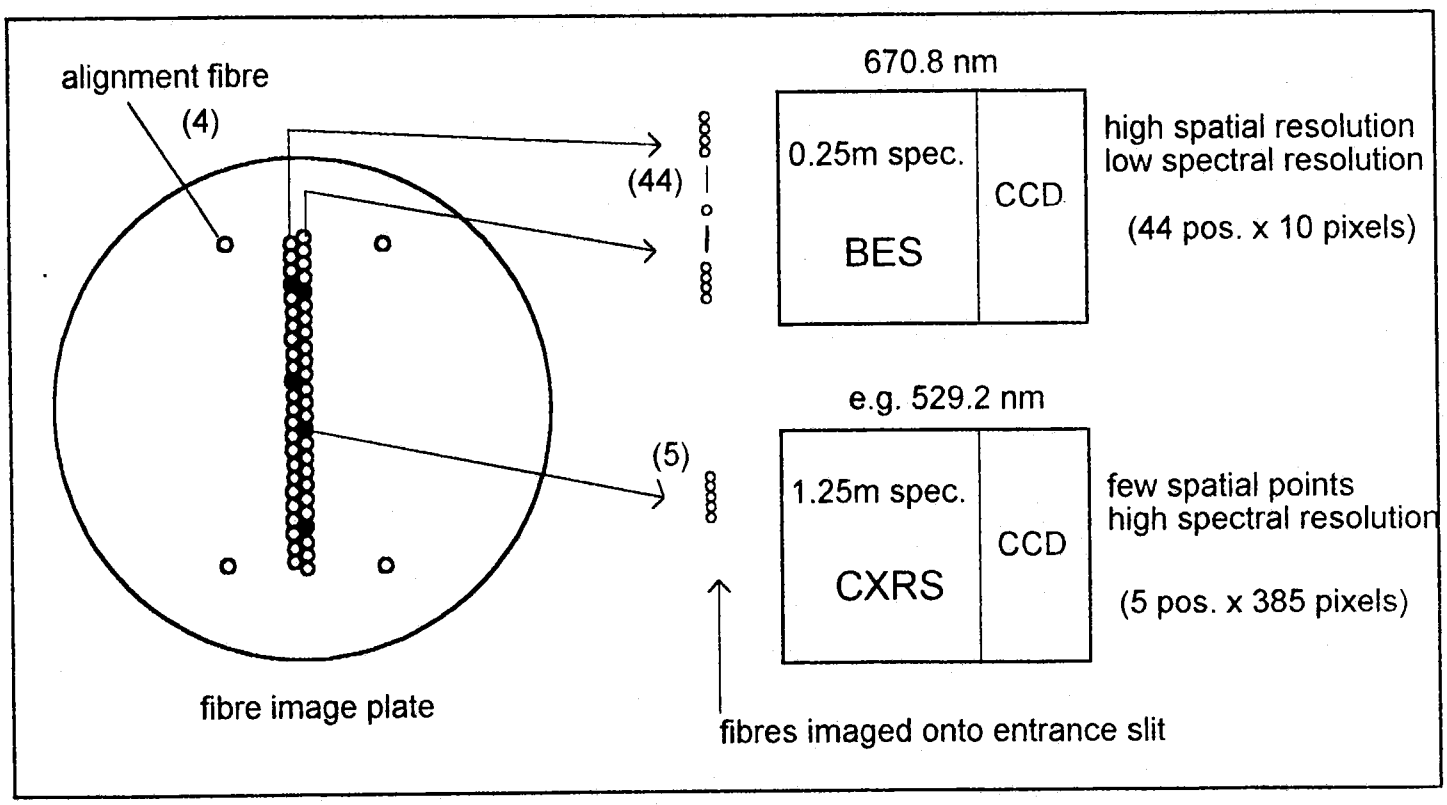

Fig. 4: Optical instrument layout.

For alignment purposes, the beam is injected into the torus filled with gas at a pressure of order 10^{-5} mbar. The beam image at 670 nm is then recorded with both instruments (see Fig. 5). The images on the CCD are Doppler-shifted due to different viewing line / beam intersection angles along the beam profile.

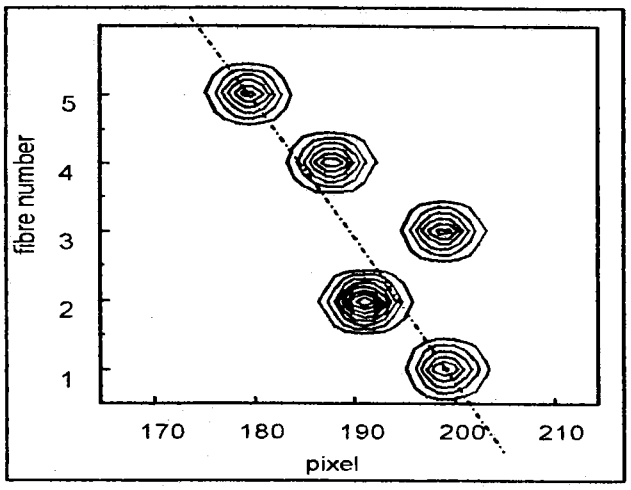

Fig. 5a: Fibre images on CXRS camera

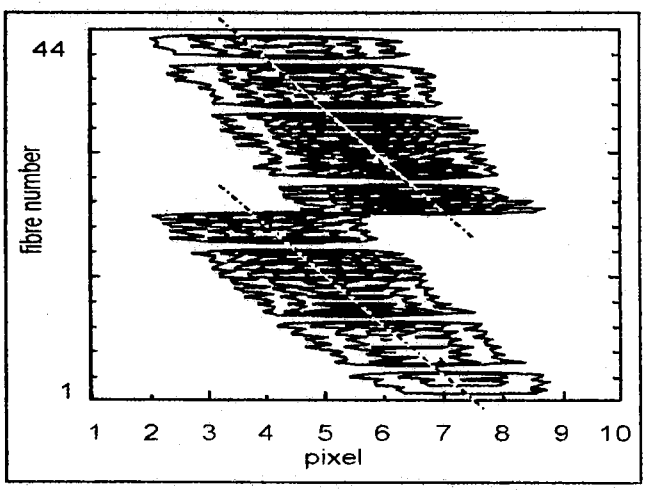

Fig. 5b: Fibre images on BES camera

The spatial position of the monitored beam profile in the torus is determined by two methods :

- back-illumination of the viewing lines with a laser and recording of the laser spots inside the torus with the in-vessel inspection system (IVIS)
- analysis of the Doppler-shift of the beam emission along the trajectory .

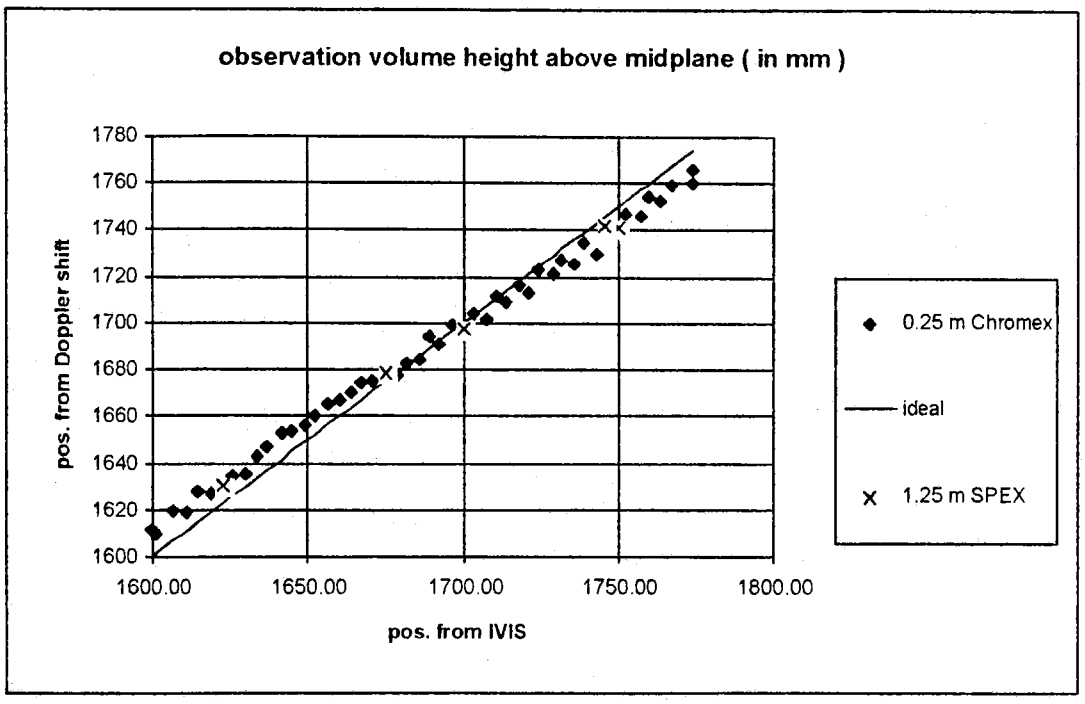

Fig. 6 : Comparison of in-vessel position of radial profile using two methods .

ELECTRON DENSITY DETERMINATION

Beam emission and attenuation model

The population of the Li-beam atomic levels (n_i) is described by a coupled set of rate equations, which for a mono-energetic lithium beam can be written as :

$$\frac{dn_i}{dx} = \sum_{j=1}^{n}(n_e \cdot n_j \cdot a_{ij} + n_j \cdot k_{ij}) \qquad (1)$$

The coefficients k_{ij} contain the spontaneous emission rates, a_{ij} contain the collision rates [4].
The observed line emission from the 2p - level is thus described by the population equation

$$\frac{dn_2}{dx} = n_e(x) \cdot \sum_{j=1}^{n}(n_j \cdot a_{2j}) + \sum_{j=1}^{n}(n_j \cdot k_{2j}) \qquad (2)$$

'Normal' solution algorithm

From eq. 2 an *exact* expression for the local electron density $n_e(x)$ can be calculated, which allows calculation of the electron density profile from the observed 2p-2s emission profile.

$$n_e(x) = \frac{\frac{dn_2}{n_2\,dx} - \sum_{j=1}^{n}\left(\frac{n_j}{n_2} \cdot k_{2j}\right)}{\sum_{j=1}^{n}\left(\frac{n_j}{n_2} \cdot a_{2j}\right)} \qquad (3)$$

This de-convolution algorithm is sensitive to :

- Limited experimental resolution (much worse than the numerical grid resolution used)
- Signal noise on emission profile (affects differentiated profile sensitively)
- Absolute specification of the injected beam current
- Error in input plasma parameters of temperature, impurity content

- Singularity point instabilities - coefficients a_{ij} and k_{ij} can be positive or negative, depending on whether excitation or de-excitation is described. There exists a particular set of plasma conditions for which the numerator and denominator both can be equal to zero. This physically corresponds to the point where electron induced population of a level is equal to electron induced de-population. Since all electron collision rates are proportional to n_e, the value of n_e is undetermined at this point in the profile. Numerically, however, the point where denominator and numerator are equal to zero will not occur at the same grid point, causing singular behaviour in a deconvolution code.

To include proton and ion collisions in the model, the electron collision coefficients a_{ij} can be rewritten to include the diluted proton concentration and any impurity concentrations

$$a_{ij} \equiv a_{ij}^{el} + \left(\frac{n_p}{n_e}\right) \cdot a_{ij}^{p} + \left(\frac{n_C}{n_e}\right) \cdot a_{ij}^{C} + \left(\frac{n_{Be}}{n_e}\right) \cdot a_{ij}^{Be}$$

$$a_{ij}^{k} n_k \equiv \sum_{q=1}^{q_{max}} \frac{\langle \sigma_{k,q} v \rangle}{v_b} \cdot n_{k,q} = q_{k,rms}^2 \cdot \frac{\langle \sigma_p v \rangle}{v_b} \cdot n_k$$

This increases the requirement for atomic collision data as well as input data to the analysis code, but does not change the existence of a singularity point.

'Integral' solution algorithm [3]

To avoid the numerical difficulties around the singularity point, an integral form of eq. 2 can be used

$$n_2(x) = \int_z^x n_e(x) \cdot \sum_{j=1}^{n} (n_j a_{2j}) dx + \int_z^x \sum_{j=1}^{n} (n_j k_{2j})\, dx + n_2(z) \qquad (4)$$

where z is the position at which the switch-over from the normal to the integral method is made. Integration by parts gives the formula used in the de-convolution code in the singularity region :

$$n_e(x) = \frac{n_2(x) + \int_z^x \frac{dn_e}{dy} \int_{zj=1}^{y} \sum^{n} (n_j \cdot a_{2j}) dxdy - \int_{zj=1}^{x} \sum^{n} (n_j \cdot k_{2j}) dx - n_2(z)}{\int_{zj=1}^{x} \sum^{n} (n_j \cdot a_{2j}) dx} \qquad (5)$$

PREDICTED PERFORMANCE

The sensitivity of the proposed algorithm to the factors listed above has been investigated [3] . The numerical instability near the singularity is overcome successfully using the "integral method" in the critical region, and the "normal method" in the surrounding profile regions. The sensitivity to the experimental constraints are found to be acceptable

- reliable de-convolution is possible for experimental resolutions of 4mm
- using a suitable noise-reduction algorithm, de-convolution of density profiles with 25% statistical error was achieved in the presence of ± 15% noise
- the sensitivity on accurate specification of injected beam current is only critical near the singularity point in the profile - this can be exploited to calibrate the beam current
- the sensitivity to ion and electron temperature is small - 50% error in temperature results in density error < 10%
- the sensitivity on impurity specification is critical near the singularity point in the profile - 30% error in impurity specification results in density errors of about 15%, larger error in impurity concentration causes instabilities near singularity point .

Presented below is an example calculation done on a simulated Li-beam emission measurement taking typical JET plasma conditions and the measured diagnostic sensitivity into account. The case shown corresponds to a 2.6 MA, 3.2 T plasma with neutral beam heating of 15 MW. The central electron density is 4×10^{19} m^{-3} . The calibrated channel sensitivities and plasma positions were used to predict the Li 670 nm emission profile, shown in Fig. 7. The Li-beam parameters in the calculation were 1 mA equivalent intensity, and 60 keV beam energy. Superimposed on the calculated signal is a 10% noise (Poisson statistic) . This signal has then been de-convoluted using above algorithm, the result is shown in Fig. 8.

The singularity point is at a position of 1.47 m (14.5 cm into the plasma profile), the separatrix position is estimated to be at 1.49 m.

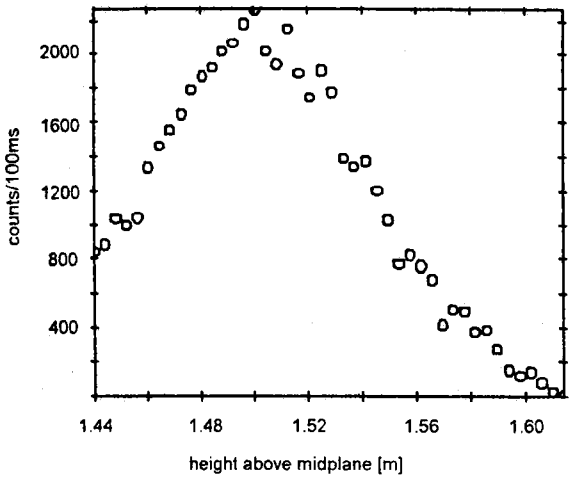

Fig. 7 : Simulated emission profile at 670 nm measured by CCD.

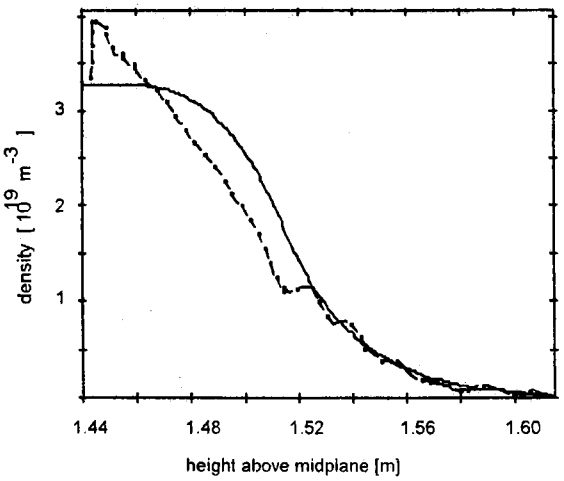

Fig. 8 : Comparison of de-convoluted density profile (dashed line) and original density profile used in simulation of Li-beam emission (full line).

The de-convoluted density profile agrees well within the 25% error limit established previously for the diagnostic accuracy [3]. The large discrepancy at 1.52m is due to an unfavourable noise excursion in the emission profile, which cannot be distinguished from a real density perturbation.

ACKNOWLEDGEMENTS

We should like to thank K.McCormick and J.Schweinzer for many helpful discussions, and the Swiss National Science Foundation for partially funding this work.

REFERENCES

[1] M Kick, K McCormick, H Schmid, A 100 keV neutral Lithium beam for plasma diagnostics, IPP Report IPP2/265, Max-Planck-Institute, Garching (1983)

[2] A J T Holmes, S Norris, The IONTRAK Code, AEA Technology, Culham, Abingdon

[3] Z A Pietrzyk, P Breger, D D R Summers , Plasma Phys. Control. Fusion **35** (1993) 1725-1744

[4] F Aumayr et al, Atomic database for lithium beam edge plasma spectroscopy, IAEA report INDC-NDS-267 (1992)

The Scaling of JET Divertor and Scrape-Off Layer Parameters

S Davies, S K Erents[1], H Y Guo[2], A Loarte, G F Matthews, K McCormick[3], R D Monk[4], D O'Brien.

JET Joint Undertaking, Abingdon, Oxfordshire, OX14 3EA, UK.
[1] UKAEA Fusion, Culham, Abingdon, Oxfordshire, OX14 3DB, UK.
[2] INRS-Energie et Materiaux, University de Quebec, Canada.
[3] Max-Planck-Institut für Plasmaphysik, EURATOM Association, 85748 Garching, Germany.
[4] Department of Physics, Royal Holloway College, University of London, Surrey, TW20 0EX, UK.

The Scaling of JET Divertor and Scrape-Off Layer Parameters

S J Davies, S K Erents[1], H Y Guo[2], A Loarte, G F Matthews, K McCormick[3], R D Monk[4], D O'Brien.

JET Joint Undertaking, Abingdon, Oxfordshire, OX14 3EA, UK.

[1] UKAEA Fusion, Culham, Abingdon, Oxfordshire, OX14 3DB, UK.

[2] INRS-Energie et Materiaux, University de Quebec, Canada.

[3] Max-Planck-Institut für Plasmaphysik, EURATOM Association, 85748 Garching, Germany.

[4] Department of Physics, Royal Holloway College, University of London, Surrey, TW20 0EX, UK.

1. INTRODUCTION

This poster will describe the initial investigations into divertor and Scrape-Off Layer (SOL) scaling obtained in the new JET pumped divertor using both fixed and reciprocating Langmuir probe systems. The data presented in this poster were obtained from a series of pulses at different toroidal field, input power and density in the reversed field (ion gradB away from target) configuration. The main topics described are :

- Determination of separatrix values using Pressure balance.
- Power balance.
- Scaling of SOL fall-off lengths.
- Comparison of fall-off lengths in vertical/horizontal configurations (see also poster by C. Lowry et al., this conference).
- Comparison of target power fall-off lengths with analytical and JT-60 scalings.
- Mapping of detachment with power and configuration.

2. PROBE SYSTEM OVERVIEW

- Both main SOL and target parameters can be measured simultaneously.
- The reciprocating probe measures upstream radial SOL parameters.
- The distribution of the fixed probes in the divertor, coupled with sweeping of the strike points across the divertor floor, provides complete profiles from private plasma into the SOL. Further details are presented in the poster by H. Guo et al., this conference.

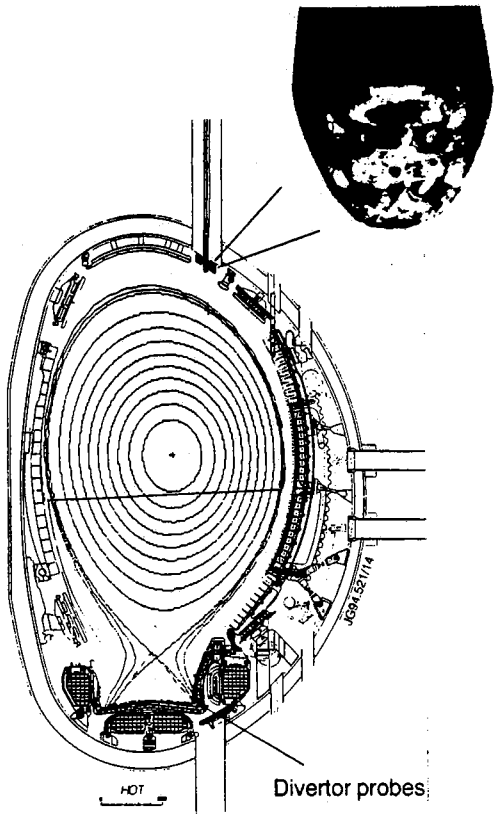

Figure 1 : Arrangement of fixed divertor and reciprocating probe systems at JET.

- Two reciprocating probe systems are available to measure the upstream radial SOL parameters in up to eight different time slices during a pulse.
- The photograph in Figure 1 shows one of the probe heads consisting of four single Langmuir elements.
- In addition to obtaining SOL profile data at each probe tip location it is also possible to obtain Mach number profiles.
- The other system has the facility to be able to use a number of different probe heads such as a Triple probe, Collector probe or Retarding Field Analyser probe.

3. PRESSURE BALANCE

- Various criteria are available to define the position of the separatrix [1]. The criteria used in our analysis has defined the separatrix at the target as corresponding to the peak in the J_{sat} profile.
- Upstream the pressure profile was shifted to attain balance with the target pressure profile. Generally this occurred close to the point at which the gradient of the upstream floating potential tends to infinity.

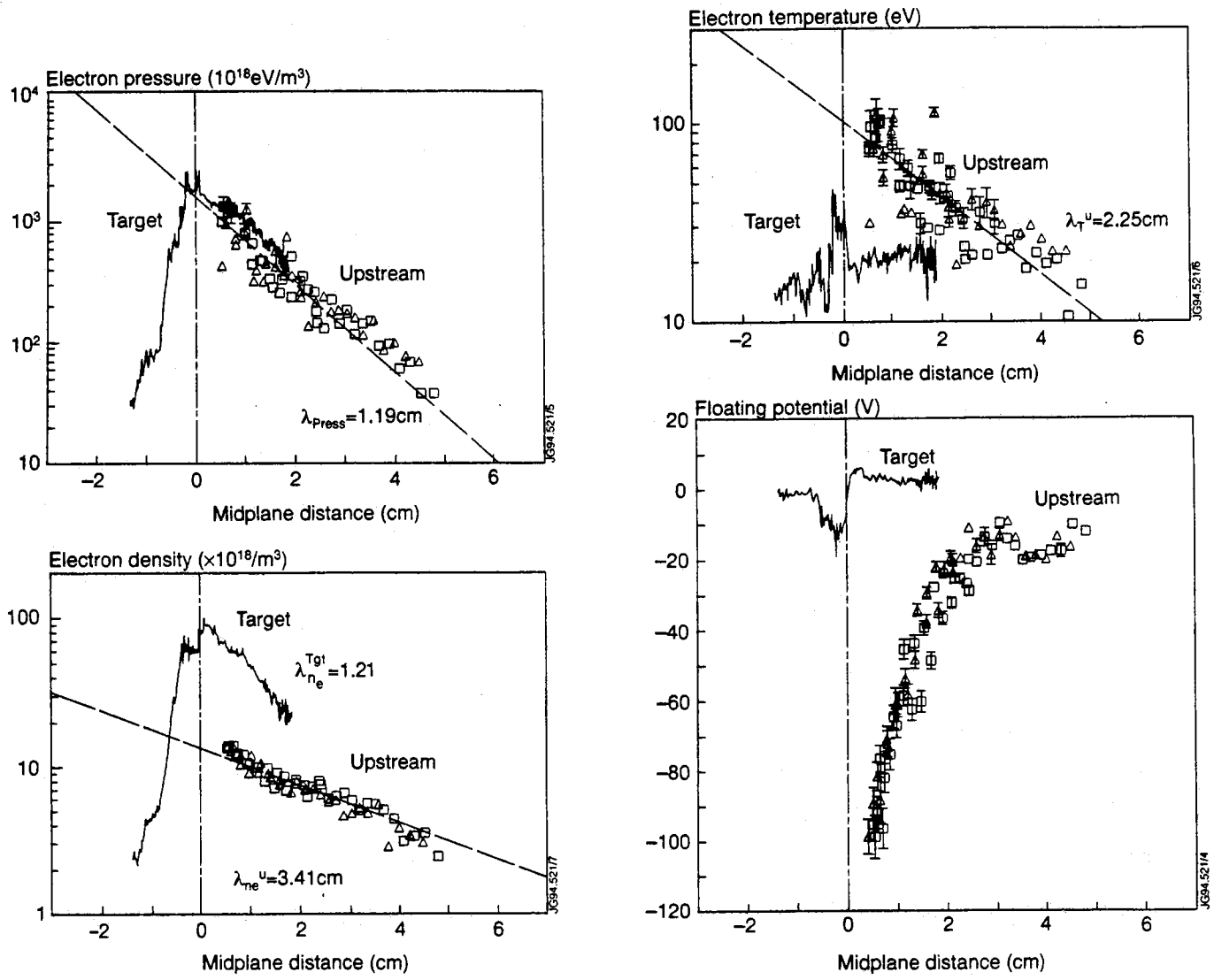

Figure 2 : Upstream and target pressure, density, temperature and floating potential profiles obtained using pressure balance method.

- λ_{Press} (target) = λ_{Press} (SOL)
- λ_{ne} (target) < λ_{ne} (SOL)
- λ_{Te} (target) > λ_{Te} (SOL)
- n_e (target) > n_e (SOL)
- T_e (target) < T_e (SOL)

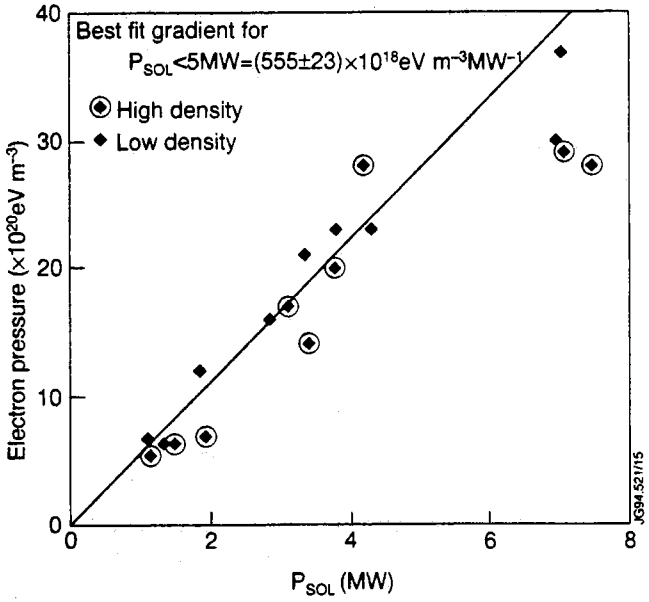

Figure 3: Upstream and target pressures as a function of power obtained using pressure balance method.

4. POWER BALANCE

- The power level observed by the target probes is compared to the power received at the divertor plates calculated from global parameters (P_{TOT} - P_{RAD} where P_{RAD} is both bulk and divertor radiated power).

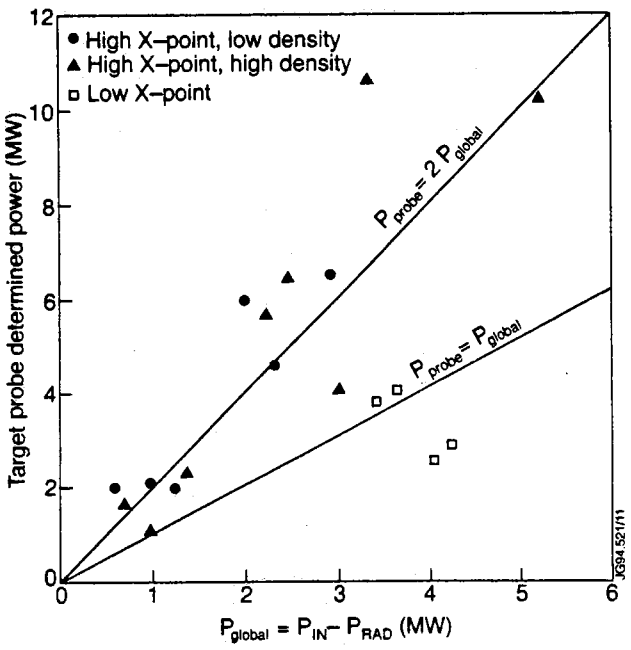

Figure 4 : Comparison of power to the target calculated from probe data and from global parameters.

- The power level observed by the probes was calculated using $Q_{par} 2\pi$ R $\sin\theta_{perp}$ λ_p for both the inner and outer strike zones, where Q_{par} is the parallel power at the separatrix calculated using the probe data and given by $\gamma J_{sat} T_e$ with $\gamma = 8$, R the major radius, θ_{perp} the field line angle and λ_p the fall-off length for Q_{par}.
- Power to divertor from probe data is approximately twice that required to achieve power balance with the high X-point pulses.
- Low X-point plasmas give better power balance.

5. COMPARISON BETWEEN UPSTREAM AND TARGET DENSITIES/TEMPERATURES

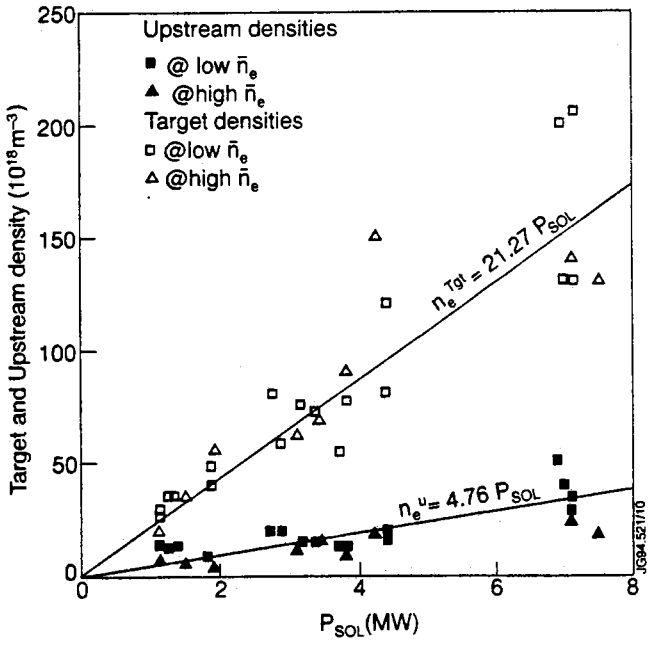

Figure 5 : Upstream and target separatrix densities derived using the pressure balance method as a function of power in the SOL.

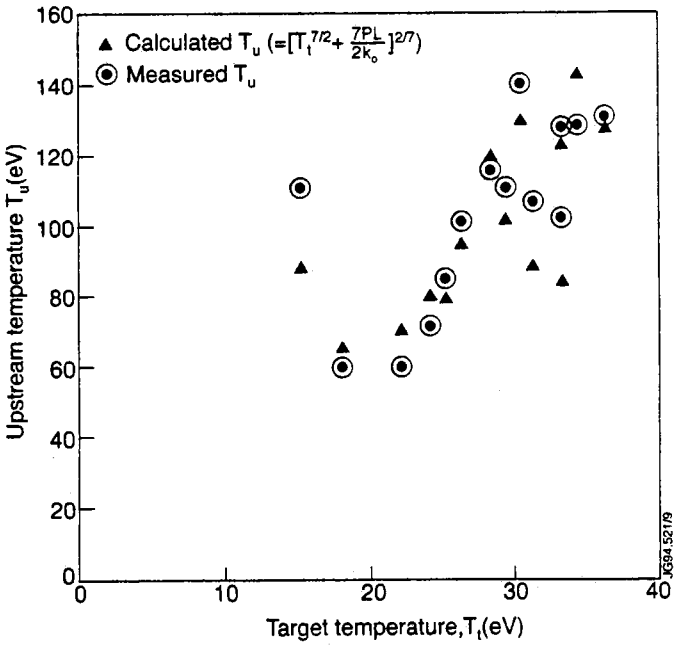

Figure 6 : Comparison between calculated and measured upstream temperatures using simple two-point model.

- The average ratio of target density to upstream density is ~4.
- The average ratio of upstream to line averaged density ranges from 0.2-0.9, the ratio generally increasing with increasing input power.
- The upstream density fall-off length, λ_n^u, is $\approx 1.6\lambda_n^{tgt}$, the target density fall-off length.

6. SCALING OF FALL-OFF LENGTHS FOR HORIZONTAL CONFIGURATIONS

- At present sufficient data are available for the scaling of fall-off lengths in horizontal configurations with B_t=2.2–2.4T.
- The best regressions are obtained by fitting to data with (i) Ohmic and input powers of <4MW and (ii) with input powers of 4-8MW.
- An example of the regression fits obtained for the upstream pressure, density, temperature and power fall-off lengths for ohmic and input powers of <4MW is shown below.
- The best fit parameters for the rest of the data are summarised in Table 1.

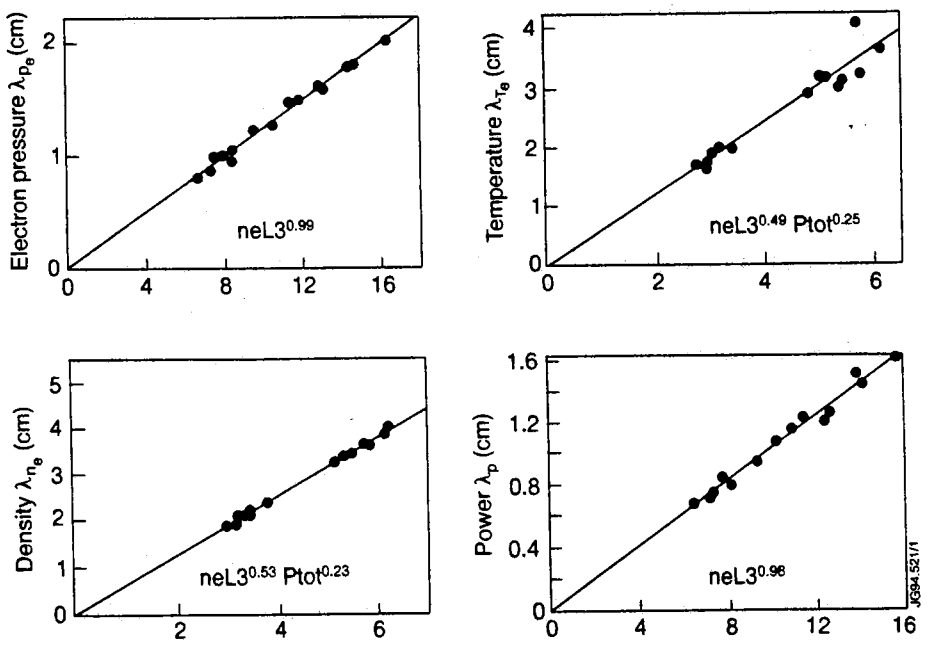

Figure 7 : Example regression fits to the fall-off lengths for pressure, density, temperature and power for ohmic and input powers of <4MW.

SOL fall-off length in	Const.	Line density Nel3 (x10^{19}m^{-2})	P_{tot} (MW)	Fit Coeff., R	Range (cm)
Pressure	0.123	0.99±0.04	0	0.994	0.8-2.0
J_{sat}	0.376	0.64±0.09	0.13±0.04	0.985	1.2-2.9
Temperature	0.603	0.49±0.17	0.25±0.07	0.962	1.6-4.0
Density	0.642	0.53±0.06	0.23±0.03	0.998	1.9-4.0
Power	0.103	0.98±0.05	0	0.989	0.7-1.6

Table 1a : Fitting parameters for P_{NI} =0-4MW

Fits are of the form, for example, T_e=0.603 $Nel3^{0.49\pm0.17}$ $P_{tot}^{0.25\pm0.07}$ and R is the regression coefficient.

SOL fall-off length in	Const.	Line density Nel3 ($x10^{19}m^{-2}$)	P_{tot} (MW)	Fit Coeff., R	Range (cm)
Pressure	0.044	0.76±0.10	0.99±0.05	0.995	1.25-2.6
J_{sat}	0.1	0.59±0.15	0.97±0.07	0.984	1.9-3.6
Temperature	0.381	0.41±0.22	0.65±0.14	0.902	3.0-4.5
Density	0.287	0.44±0.16	0.86±0.08	0.971	3.2-5.6
Power	0.042	0.75±0.16	0.90±0.08	0.986	1.0-2.0

Table 1b : Fitting parameters for PNI =4-8 MW

- Comparing the two regimes it is seen that for higher powers the density dependence is marginally reduced and the power dependence increases radically when compared to the fits for the lower powers.
- The temperature fall-off length, λ_{Te}, does not decrease with input power, P_{TOT}, as simple theory [2] might predict.

Comparisons have also been made between the fall-off lengths in horizontal and vertical configurations as illustrated below.

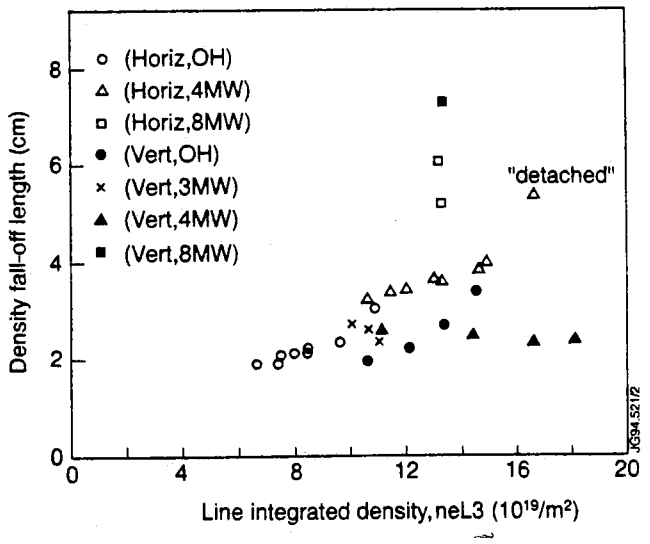

Figure 8 : Comparison between density fall-off lengths for horizontal and vertical configurations.

- The vertical fall-off lengths in density are generally lower than the horizontal case.
- λ_{ne} under OH conditions in the vertical configuration does not increase as rapidly as for the horizontal configuration.
- For moderate (<8MW) heating, λ_{ne} for the vertical case shows no increase with density whereas it increases rapidly for the horizontal case, leading to detachment.
- At 8MW, for the one density point available, there is no significant difference.

7. SCALING OF TARGET POWER FALL-OFF LENGTHS

(i) Scaling with JET specific parameters

- The target power fall-off length, λ_P^{tgt}, calculated using JET specific quantities is [3]

$$\lambda_P^{tgt} = \left(\frac{2}{7}\right)^{7/9} \left(en_u \chi_p A_p\right)^{7/9} P_{SOL}^{-5/9} \left(\frac{7L}{8\pi R k_o (B_\theta / B)_u}\right)^{2/9}$$

where $A_p = 4\pi^2 Ra\kappa^{1/2}$ and typical values for JET are R=3m, a=0.9m, $\kappa = 1.8$ and $Z_{eff} = 1$.

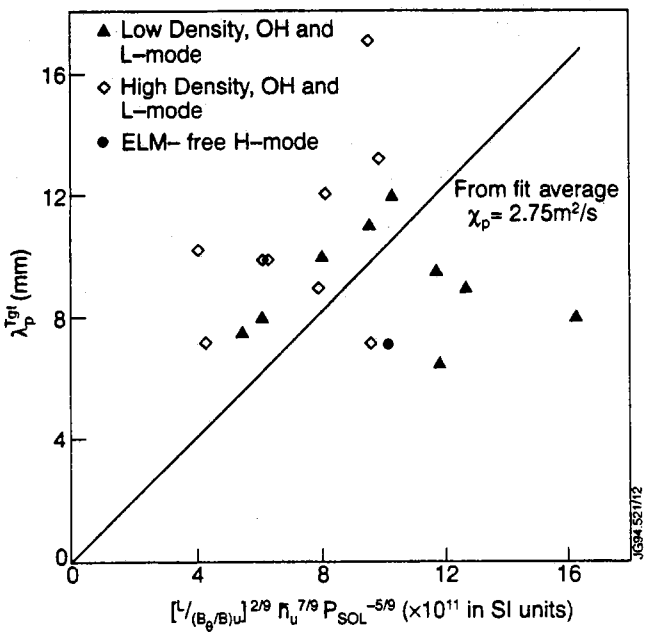

Figure 9 : Scaling of λ_P^{tgt} with JET specific parameters.

- A best fit to the data shown below results in an average χ_{perp} of 2.75m²/s.
- The spread of the data illustrates that χ_{perp}, derived in this way, is not a constant.
- In the current data set, χ_{perp} ranges from ~2m²/s to ~6m²/s.

(ii) Scaling with JT-60 data

- The behaviour of λ_P^{tgt} within the framework of the JT-60 empirical scaling law [4] is shown. Regression analysis shows $\lambda_P^{tgt} \sim B_t^{0.42}$ in general agreement with JT-60.

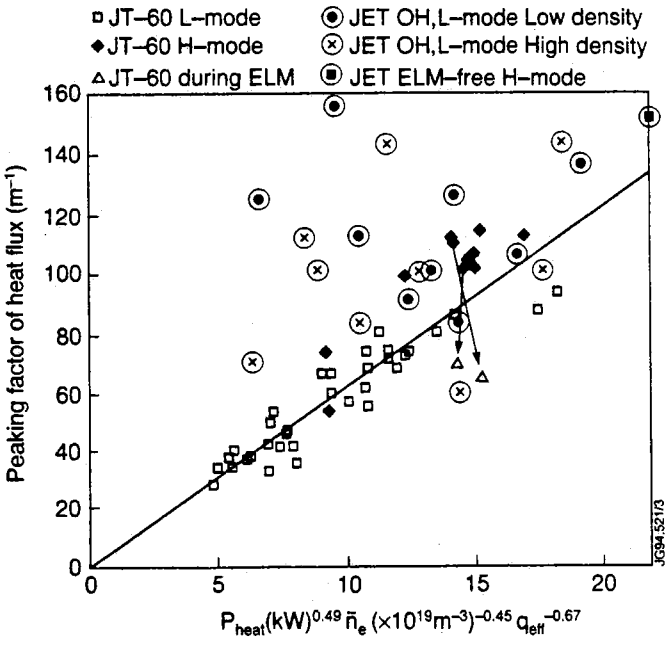

Figure 10 : λ_P^{tgt} as a function of the JT-60 experimentally derived scaling law.

8. MAPPING OF DETACHMENT WITH POWER AND CONFIGURATION

- Data for Ohmic and 4MW injected neutral beam power in the Horizontal (ion-gradB drift towards and away from target) and Vertical (ion-gradB away from target) configurations are currently available.
- Further details on detachment are also given in the poster by H. Guo et al., this conference.

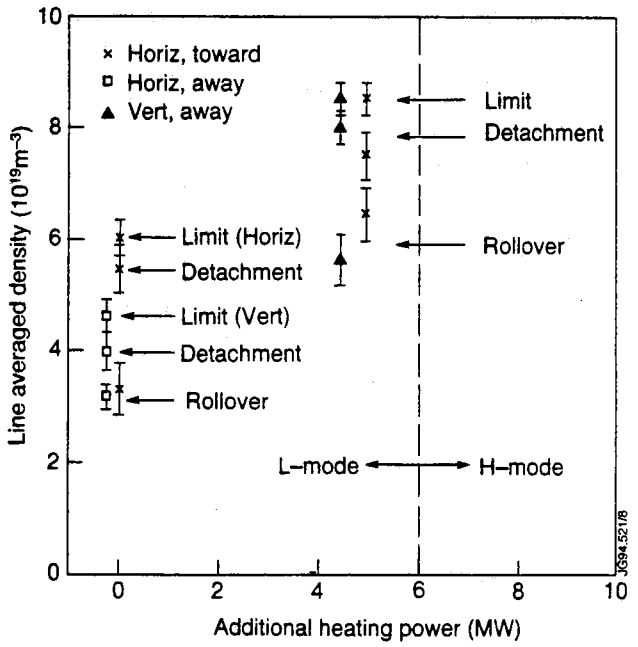

Figure 11 : Line averaged density at which rollover, inner detachment and density limit occur as a function of additional heating power and configuration.

- In Ohmic and L-mode discharges the density limit occurs with the formation of a MARFE. In H-mode it is set by an H- to L-mode transition.
- The rollover in the horizontal configuration occurs at the same density in the ohmic case for both ion-gradB towards(Normal field) and away from (Reversed field) the strike point.
- In the L-mode cases, the rollover, detachment and density limit are the same for both the horizontal, toward and vertical, away cases.

9. REFERENCES

[1] Vlases, G. et al., J. Nucl. Mat., 196-198, 392 (1992)
[2] Keilhacker, M. et al., Physica Scripta, T2/2, 443 (1982)
[3] Stangeby, P. C., personal communication
[4] The JT-60 Team, presented by M. Shimada, IAEA-CN-56/a-1-3, 1, 57 (1993)

ACKNOWLEDGEMENTS

The authors would like to acknowledge the expertise of C. Hogben, G. Kaveney, G. Neill, J. Vince and D. Wilson whose skill and commitment have made such measurements possible.

Single and Triple Probe Operation of the JET Divertor Probe Array

H Y Guo[1], R D Monk[2], G F Matthews, A V Chankin, S Clement, S J Davies, S K Erents, A Loarte.

JET Joint Undertaking, Abingdon, Oxfordshire, OX14 3EA, UK.
[1] INRS-Energie et Materiaux, University du Quebec, Canada.
[2] Royal Holloway College, University of London, UK.

Single and Triple Probe Operation of the JET Divertor Probe Array

H Y Guo[1], R D Monk[2], G F Matthews, A V Chankin, S Clement, S J Davies, S K Erents, A Loarte.

JET Joint Undertaking, Abingdon, Oxfordshire, OX14 3EA, UK.

[1] INRS-Energie et Materiaux, University du Quebec, Canada.

[2] Royal Holloway College, University of London, UK.

1. INTRODUCTION

The new JET Langmuir probe system consists of 171 probe tips distributed in the limiters and divertor regions of the vessel. Of these, there is a dense array of 117 probe tips in the divertor target which can be configured as triple or single probes. The triple probe technique has the advantage of continuously measuring the plasma temperature and density unlike the single probes which require the applied voltage to be ramped for each I-V characteristic.

- To reduce the average power load on the pumped divertor target plates, plasma sweeping is routinely used. Since the strike zones move across the target at a frequency of 4 Hz, the high time resolution of the triple probes has proven essential.

- Assuming no significant evolution in plasma parameters during the sweep, full profiles of electron density and temperature can be constructed.

- The triple probe array also offers the capability of carrying out space-and time-resolved studies of fast phenomena, such as ELMs.

2. OUTLINE

- Comparison of results from single and triple probe operation;
- Modification of the target profiles by ELMs during swept discharges;
- Comparison of target and SOL plasma profiles during plasma detachment.

3. COMPARISON OF SINGLE AND TRIPLE PROBE OPERATION OF THE DIVERTOR TRIPLE PROBE ARRAY

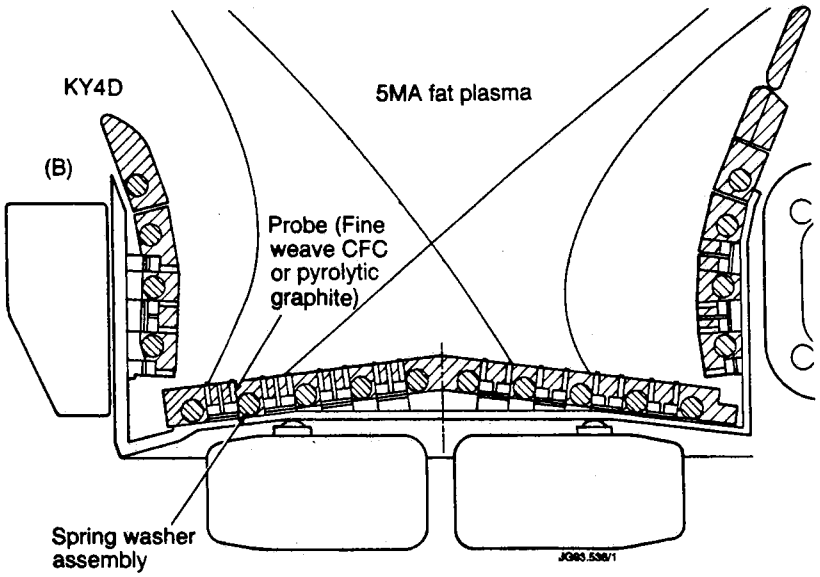

Fig.1 Arrangement of the JET divertor fixed Langmuir probe array

- Langmuir probes are mounted between tiles in both the floor and side panels of the divertor with a radial or vertical resolution of 1 ~ 4 cm (Fig.1).
- The probe tips are tilted with an angle of 7° to 9° relative to the surface of the tiles.
- Maximum time resolution: 0.2 ms.
- The probes can be configured as single probes, or as triple probes with three tips distributed on a toroidal arc (Fig.2).

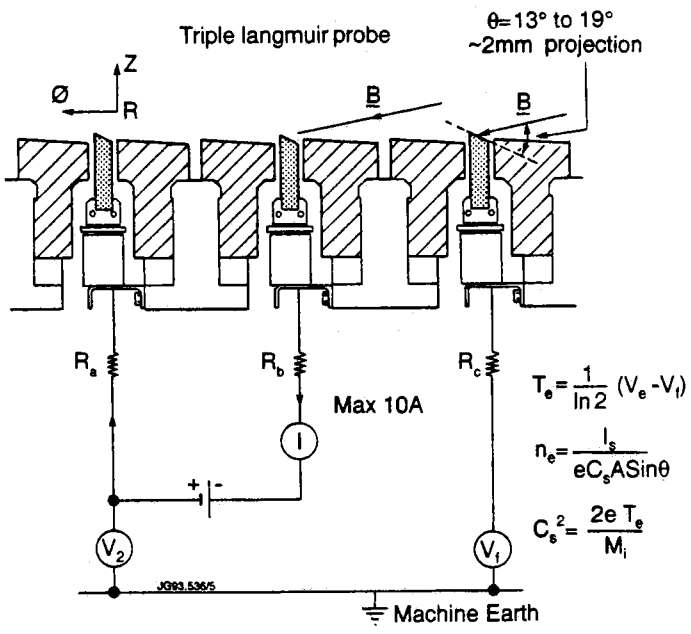

Fig.2 .Set-up of a divertor triple probe system

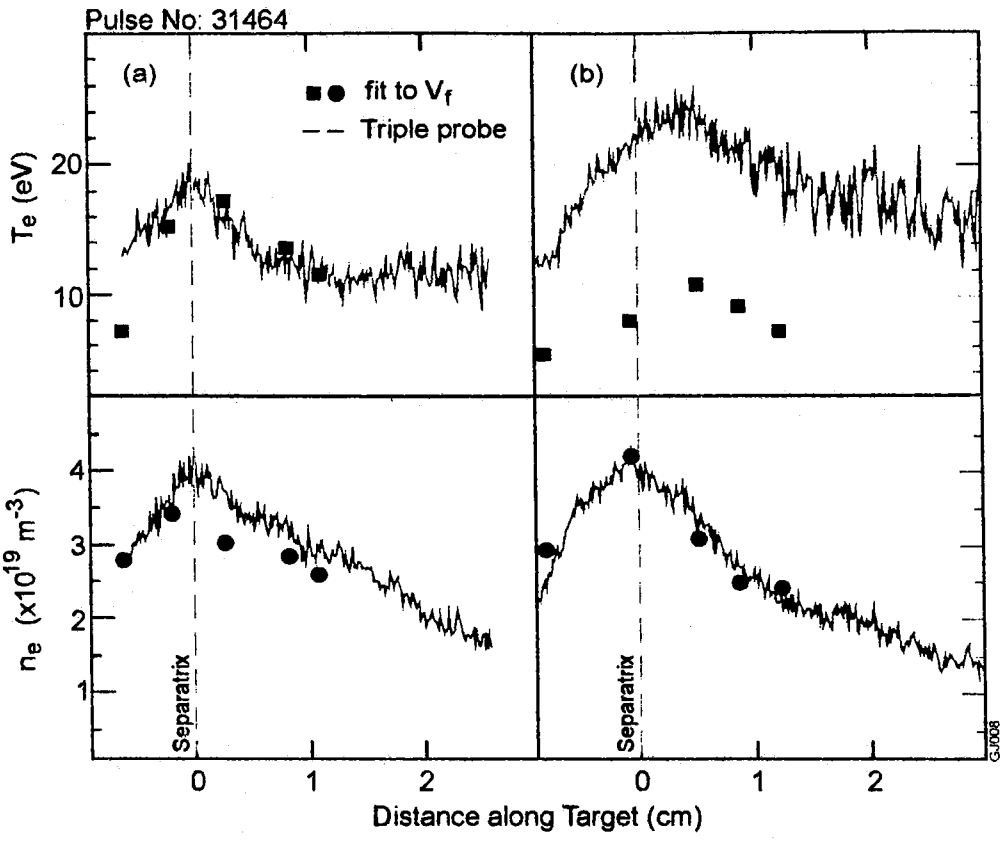

Fig.3 Electron temperature and density at the outer target for the central plasma densities: (a) $3x10^{19}$ m^{-3}; (b) $4x10^{19}$ m^{-3}

- Single probe data shows that the characteristics do not show any significant non-saturation of the ion current.

- At lower plasma densities, agreement between the single and triple probe results is generally good (Fig. 3.a).

- At high densities, triple probes overestimate the electron temperature (Fig.3b), as also observed with fitting I-V characteristics beyond floating voltage with single probes, due to the reduced electron to ion saturation current ratio [1].

- Asymmetric triple probes have been installed to reduce this problem.

4. MODIFICATION OF THE TARGET PROFILES BY ELMS

In the JET pumped divertor configuration, ELMs are regularly observed and this has allowed long pulse, steady state H-modes to be established [2]. The ELM duration is typically 1 ~ 3 ms and the frequency increases with the density and the input power [3]. Divertor plasma parameters between and during ELMs have been measured by the triple probes during swept discharges (Fig.4 and Fig.5).

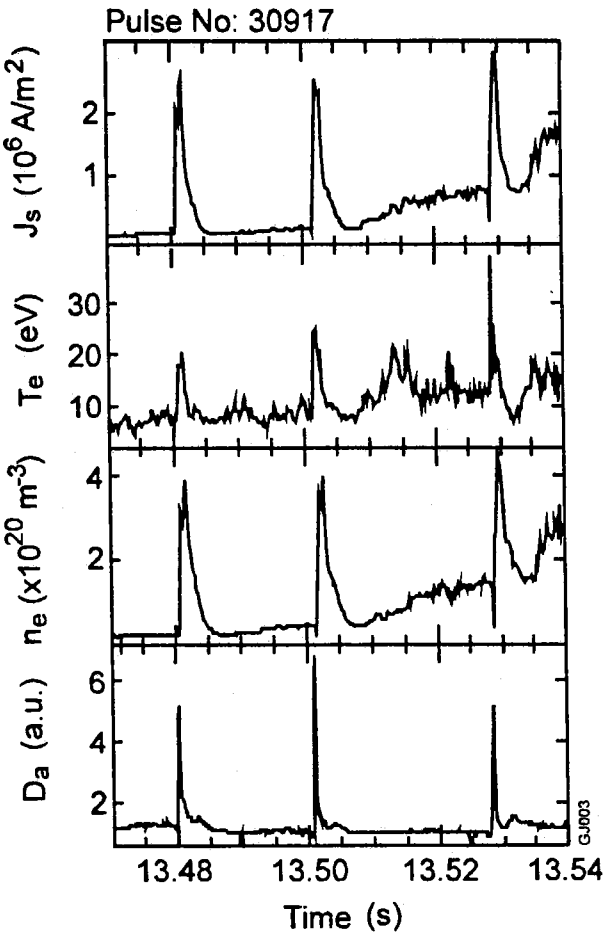

Fig. 4 ELM profiles on the swept plasma at the inner target

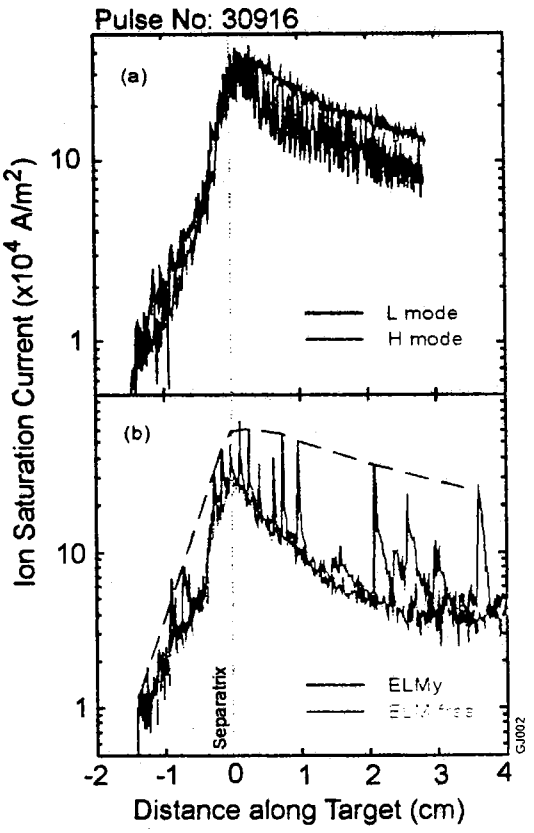

Fig.5 Ion saturation current profiles (outer target): (a) during L-H transition; (b) during ELM free and ELMy phases

- Both the temperature and the density rise during an ELM, and decay quickly to a value even below the background plasma value, as also observed in ASDEX-U [4].

- The temperature spikes are narrower and peaks before the density, as shown in Fig.4.

- The profile during H-mode is narrower, as observed before [5]. Frequent small ELMs are observed during the L-H transition, but have a large amplitude after the ELM free period.

- ELMs lead to a much broader profile, resulting in a spreading of power deposition on the target plates. It has been observed that the peak target temperature during these discharges is lower than in comparable L-mode discharges [6].

At high density and high input heating power, ELMs can significantly modify the asymmetry of the power deposition on the divertor target plates. Fig.6 shows the ion saturation current measured by the inner and outer target probes, the maximum surface temperature of the inner and outer target plates measured by IR thermography, the input power and the plasma central density.

- Particle fluxes during ELMs to the inner target are larger than those on the outer target.

- Power deposition of ELMs on the inner target is significantly larger than that on the outer one (see blow up of Fig.6).

- Consequently, the temperature at the inner target increases more rapidly than the outer target.
  However, different patterns are observed in low density and heating power discharges.

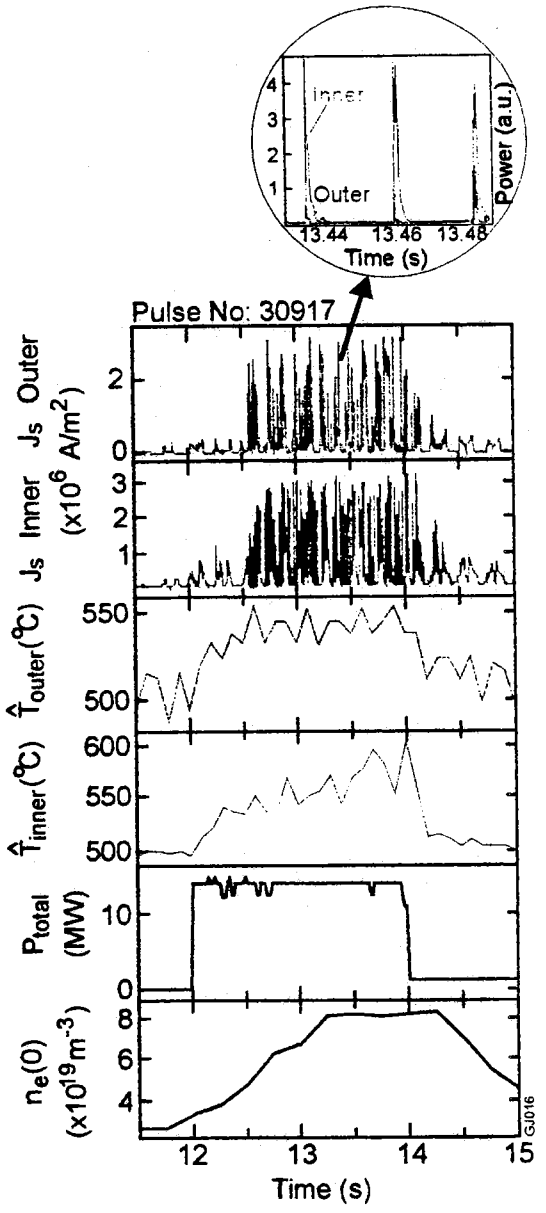

Fig.6 Effect of ELMs on the asymmetry of the power deposition on the target plates

5. COMPARISON OF TARGET AND SOL PLASMA PROFILES DURING A DETACHED PLASMA

Ohmic and L-mode detached plasmas have been established using both pre-programmed density ramps and feedback from the triple probe ion saturation current. The triple probe array is the main diagnostic for these experiments.

Fig.7 shows the time evolution of a swept L-mode detached plasmas on the inner target and the outer target plates with input power of 4 MW (NBI). The peaks in the J_S correspond to the maximum value at the strike point.
The envelope gives the time evolution of the ion saturation current at the separatrix.

- As the core density is increased, the ion saturation current to the inner target probe increases and peaks, then it decreases gradually, this indicates that the plasma is beginning to detach from the inner target.

- The plasma also partially detaches from the outer target, but at a later time.

- The D_α signals in both the inner target and the outer target increase throughout this period. However, bolometer signals from the strike zones decrease and the X-point radiation increases (R.Reichle, this conference).

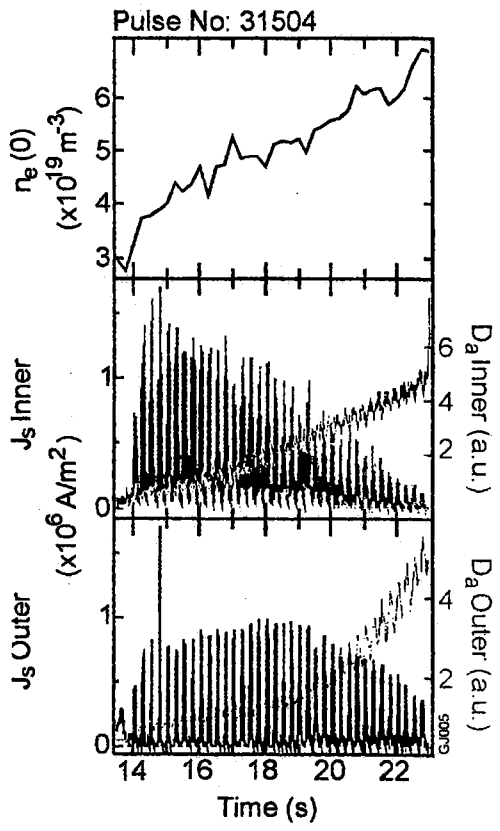

Fig.7 Evolution of the detached plasmas

Fig.8 shows the plasma parameters in the inner divertor target measured with one triple probe at 15s (before detachment) and 21s (after the detachment) as a function of the mid-plane distance to the separatrix (solid lines), which is determined using pressure balance before detachment. This figure also shows the upstream SOL plasma profiles obtained from a fast moving reciprocating probe on the top of the machine (see the poster of S.J.Davies, this conference), represented by symbols.

- The plasma is detached mainly in the vicinity of the separatrix.
- During the detachment, momentum and particle flux to the target plates are substantially decreased.
- The plasma temperature measured on the target is reduced to a value below 5 eV.
- The pressure balance between the upstream and divertor plasma is quite good before the detachment.
- However, after the detachment, the upstream plasma parameters remain very similar to those before the detachment.

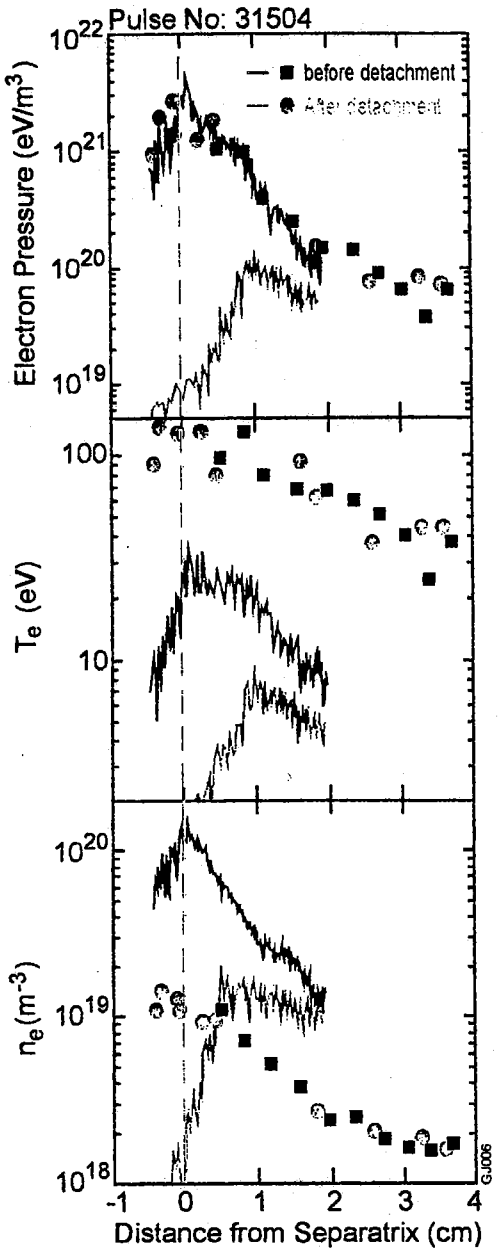

Fig.8 Divertor and SOL plasma profiles before and after the detachment on the inner horizontal target

6. CONCLUSIONS

- The new JET target triple probe array has been used successfully to perform measurements of the divertor plasma under a variety of operational regimes. It offers great potential for the studying of fast phenomena, such as ELMs.

- Agreement between the single and triple probe data is good for low density plasmas. However, in the high density and high recycling divertor plasmas, the temperature is overestimated by triple probe technique due to reduced electron saturation current.

- ELMs lead to broad plasma profiles. During an ELM both the particle flux and the temperature first increase, then decay quickly to a value below the plasma background. Temperature spikes appear to be narrower. At high density and high heating power H mode discharges, ELMs can significantly modify the asymmetry of power deposition on the divertor target plates.

- During plasma detachment, pressure decreases by an order of magnitude and temperature falls below 5 eV on the divertor target. However, upstream profiles do not change significantly.

REFERENCES

[1] J.A. Tagle, P.C. Stangeby and S.K. Erents, Plasma Phys. Controll. Fusion **29**, 297 (1987).

[2] THE JET TEAM (presented by D. Campbell), IAEA-CN-60/A-4-I-4, the proceedings of 15th IAEA conference, 1994

[3] THE JET TEAM (presented by A. Tanga), the proceedings of the 21st EPS Meeting on Controlled Fusion and Plasma Physics.

[4] A. Herrmann, M. Laux, D. Coster, et al., ASDEX-U team, to be published in Journal of Nuclear Materials (Proceedings of 11th PSI, 1994).

[5] J.A. Tagle, S. Clement, A. Loarte, et al., J. Nucl Mater. **196-198**, 409 (1992).

[6] THE JET TEAM (presented by L.D. Horton), IAEA-CN-60/A4-I-5, the proceedings of 15th IAEA conference, 1994

Comparison of High-β_p Regimes between JET and JT-60U on Confinement and Fusion Reactivity

The JET and JT-60U[1] Teams
(presented by S Ishida[1]).

JET Joint Undertaking, Abingdon, Oxfordshire, OX14 3EA, UK.
[1] Japan Atomic Energy Research Institute, Naka Fusion Research Establishment, Naka-machi, Naka-gun, Ibaraki-ken, 311-01 Japan.

Comparison of High-β_p Regimes between JET and JT-60U on Confinement and Fusion Reactivity

The JET and JT-60U[1] Teams (presented by S Ishida[1]).

JET Joint Undertaking, Abingdon, Oxfordshire, OX14 3EA, UK.

[1] Japan Atomic Energy Research Institute, Naka Fusion Research Establishment, Naka-machi, Naka-gun, Ibaraki-ken, 311-01 Japan.

INTRODUCTION

High-β_p regime has become a new paradigm of tokamak fusion reactor developments, since it has the significant potential of enhancing the economical attractiveness in a fusion reactor where the requirement for external sources of non-inductive current drive is very much reduced. The eventual goal of this regime is to maintain a high pressure plasma in a steady state with highly enhanced confinement and stability under a large fraction of bootstrap current. Such a plasma has been extensively developed in JT-60U high-β_p regime [1,2] and JET high-β_p regime [3,4] both with non-circular divertor configurations. In spite of the similar β_p domains explored, there have been many important differences in confinement properties and fusion performance between the two regimes, in particular concerning the steady ELMy plasmas in JET and the ELM-free plasmas in JT-60. This paper aims at comparing these regimes in the two machines including the operational conditions and the plasma characteristics for optimization and further extension of these regimes towards the advanced tokamak reactors.

JT-60U EXPERIMENTS

The high-β_p regime in JT-60U is produced in non-circular divertor discharges with an elongation typically 1.7 and an aspect ratio ~4.3 with the plasma volume V_p~48 m^3, as shown in Fig.1, configured to achieve central deposition of the nearly perpendicular neutral beam injection (NBI) (up to 24 MW). In addition to the perpendicular NBI system, JT-60U has two off-axis tangential NBI system (up to 12 MW) balanced to the co- and counter directions respective to the plasma current.

The experiments have been conducted to create a high performance plasma with a high bootstrap fraction. Control of the edge recycling is a prerequisite and has been achieved by a combination of the divertor action and boronization of the first wall where the vacuum vessel is baked at ~290 degrees. Suppression of sawtooth oscillations, reducing the internal inductance below ~1.2, and avoidance of locked MHD modes are necessary for the improvement in performance.

Under these conditions, the high-β_p mode plasma has been produced with a highly peaked pressure profile by concentration of the central beam fueling and heating and is sometimes combined with H-mode characteristics ("high-β_p H-mode"). As shown in Fig.2, the central electron density increases up to ~6×10^{19} m^{-3} during beam injection from the target plasma density below ~1×10^{19} m^{-3}.

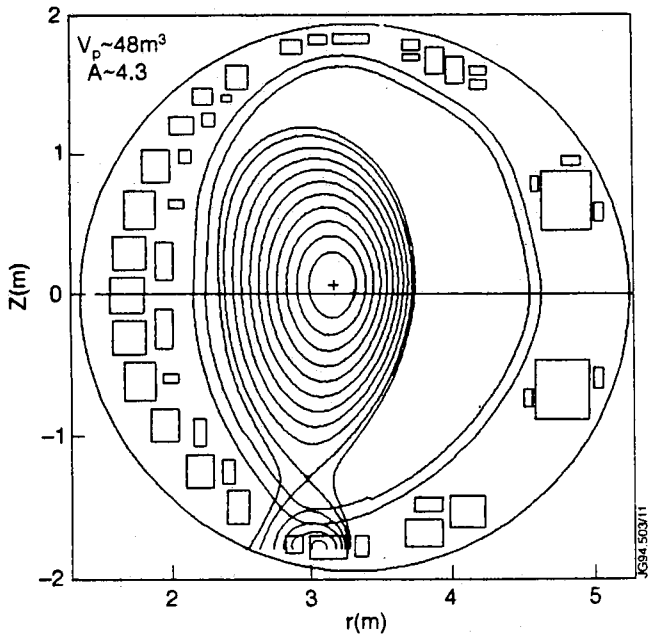

Fig. 1: High-β_p plasma configuration in JT-60U, indicating the plasma volume and aspect ratio of 48 m^3 and ~4.4, respectively.

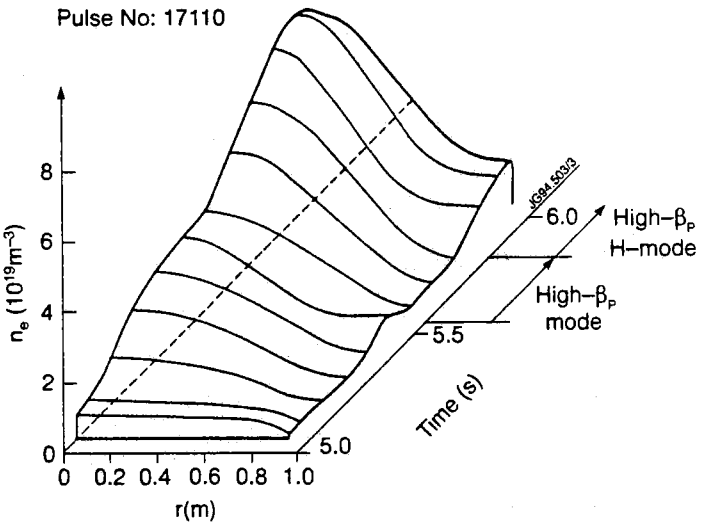

Fig. 2: Typical density evolution of a high-β_p discharge during intense neutral beam injection in JT-60U, where the density profile becomes centrally peaked during the high-β_p mode phase and the edge density also increases during the high-β_p H-mode phase.

JET EXPERIMENTS

The new experimental phase of JET with a pumped divertor configuration started operating in February 1994. The vacuum vessel is baked at ~250 degrees during operations, in which the first wall is conditioned with beryllium-evaporation and helium glow discharge cleaning. In the high-β_p campaign, a steady-state high-β_p regime has been aimed at and achieved with ELMy plasmas.

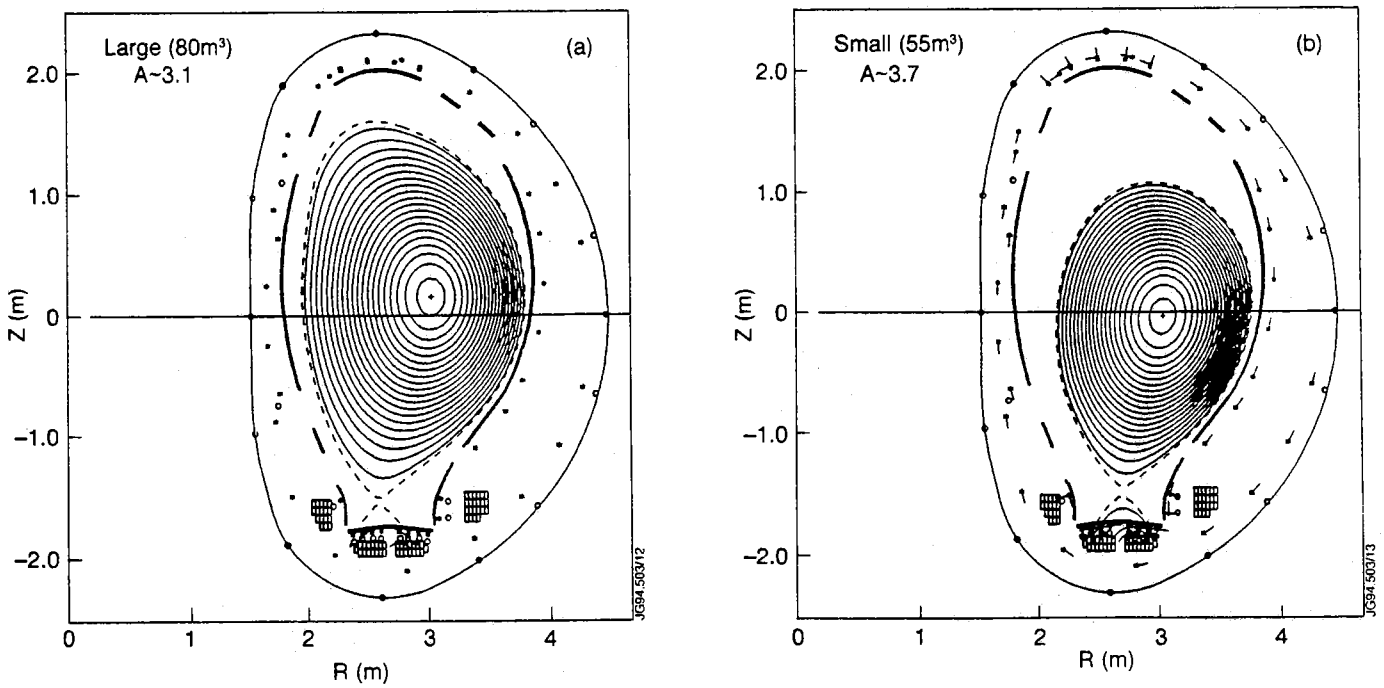

Fig. 3: Typical high-β_p plasma configurations in JET; (a) the 'large' volume configuration with an aspect ratio A~3.1 and a plasma volume V_p~80 m^3, and (b) the 'small' volume configuration with A~3.7 and V_p~55 m^3.

Small volume experiments have been also conducted with NBI heating up to 17 MW and NBI+ICRF combined heating up to 26 MW. While the normal 'large' plasma configuration has a plasma volume V_p~80 m^3, an elongation κ~1.7 and an aspect ratio R_p/a~3.1, the 'small' plasma configuration has Vp~55 m^3, κ~1.6 and a relatively large aspect ratio R_p/a~3.7 as shown in Fig.3. In both configurations, the injected beam lines pass near the plasma center and the outside curvature of the plasma surface is shaped to make the ICRF coupling to the plasma improved.

In comparison with the JT-60U high-β_p operation, generally, there has been marked difference in JET that the target plasma for main beam injection has sawtooth oscillations and relatively high electron density ~2.5×10^{19} m^3 to suppress shinethrough of the tangential beams facing the ICRF antennas. Thus, the electron density profile tends to become flat or even hollow during ELMy H-mode even if the plasma volume is significantly reduced as shown Fig.4.

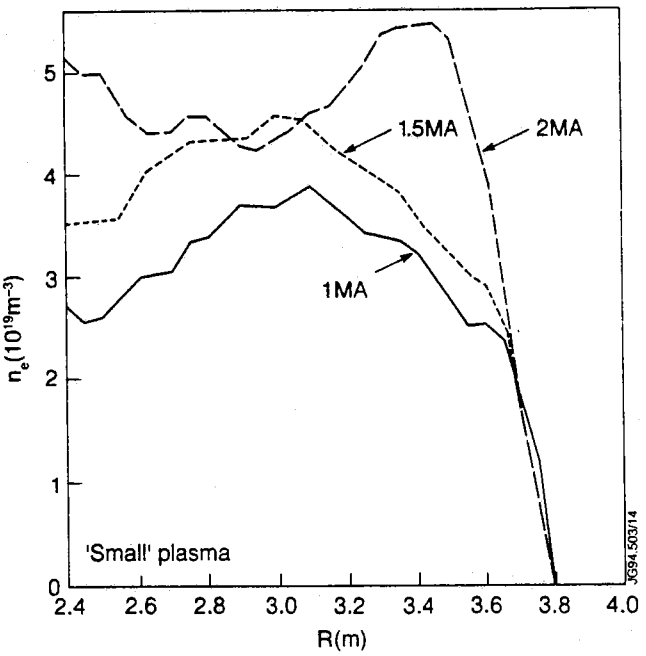

Fig. 4: Electron density profiles during neutral beam injection for the small volume plasma measured by LIDER Thomson scattering system in JET, where the cases at I_p=1.0, 1.5 and 2.0 MA are shown.

SMALL VOLUME PLASMAS IN JET

The small/large volume experiments in JET have been conducted for the range of $\beta_p \leq 1.5$ in the light of size scaling of confinement and comparison with the JT-60U high-β_p regime under the following conditions: 1.5 MA/2.8 T for 'large' case; 1.0, 1.5 and 2.0 MA/2.8 T and 1.0 MA/1.4 T for 'small' case. The NBI and ICRF heating up to P_{NBI}~17 MW and P_{IC}~6 MW, respectively, are applied in power scans. In some cases of the combined heating experiment, preheating by ICRH and/or beams before the main beam injection has been utilized to increase the target electron temperature.

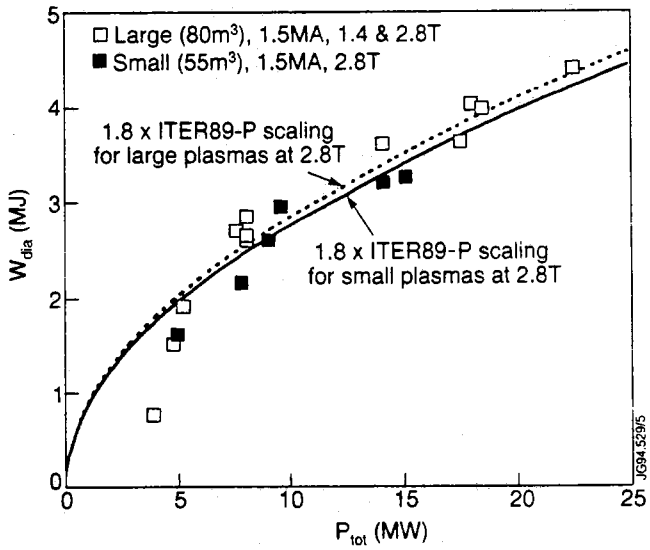

Fig. 5: Diamagnetic stored energy W_{dia} as a function of total heating power P_{tot} for the small and large volume discharges at 1.5 MA along with the predictions from the ITER89-P scaling, in which the confinement is not changed in spite of vast differences in plasma conditions.

The results show that the energy confinement is not changed though the plasma configuration is vastly different at the same radius.The confinement enhancement factor (H-factor) against the ITER89-P L-mode scaling reaches ~1.8 for ELMy plasmas at 2.8T for both plasmas as shown in Fig.5 where the W_{dia} value is plotted against the total heating power at 1.5MA. The evidence suggests that the major radius is the dorminant size parameter for determining the energy confinement for ELMy plasmas at high β_p. The fact of the higher pressure plasma with the same τ_E in the small plasma would also support the argument that the high aspect ratio is beneficial to the fusion triple product in ELMy plasmas at high-β_p, which is quite favorable for advanced tokamak concepts with a high aspect ratio.

ENERGY CONFINEMENT TIMES

Energy confinement times for the two high-β_p regimes in JT-60U and JET are shown in Fig.6 as a function of the H-factor. Noted that the τ_E values have the non-thermal components of the stored energy, typically, ~30% at 2MA in JT-60U and ~20% at 1.5MA in JET and the transient component ($dW/dt/P_{tot}$) up to ~50% in JT-60U whereas this term is negligible in the JET data. The energy confinement in the JET high-β_p regime accords with ~1.8 times the ITER89-P scaling for ELMy plasmas and sometimes exceeds it to some extent when the ELM-free phase is sufficiently prolonged using different plasma shaping such as double-null configurations and higher triangularity (up to $\delta \leq 0.4$).

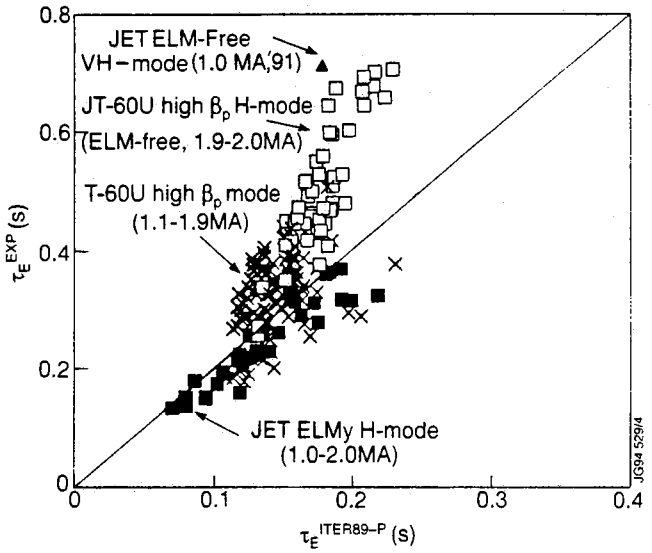

Fig. 6: Energy confinement times magnetically measured as a function of the predicted confinement times from the ITER89-P scaling for the high-β_p discharges in JET and JT-60U.

CONFINEMENT ENHANCEMENT FACTORS

Figure 7(a) shows the dependence of β_p on the H-factor for the JT-60U high-β_p regime. The high-β_p mode is characterized by enhanced core confinement with a peaked pressure profile inside an internal transport barrier [2]. The high-β_p H-mode during ELM-free phase shows higher confinement enhancement than the high-β_p mode for a given β_p value. The JT-60U results are promising for the high-β_p tokamaks since it would be possible to achieve such an enhanced confinement with a large bootstrap current fraction.

In contrast , as shown in Fig.7(b), the JET results for ELMy plasmas in the high-β_p regime show that the confinement enhancement factor is kept constant within βp values up to 2.5, although the long ELM-free H-mode plasmas in the 1991 high-β_p campaign show a similar dependence to the above JT-60U results. While a theoretical model has been proposed to explain such a positive correlation between confinement and β_p or bootstrap fraction [5], the correlation mechanisms are not comprehensively understood yet including these contradictory results.

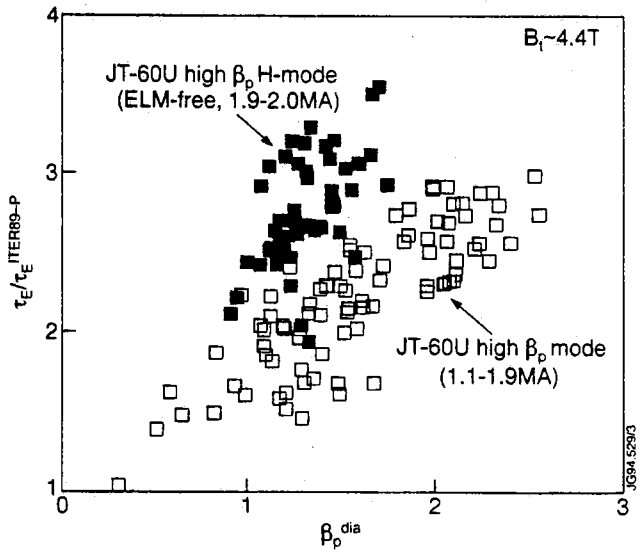

Fig. 7(a): Confinement enhancement factor against the ITER89-P scaling as a function of diamagnetic poloidal beta β_p^{dia} for high-β_p mode and high-β_p H-mode plasmas at 4.4 T in JT-60U.

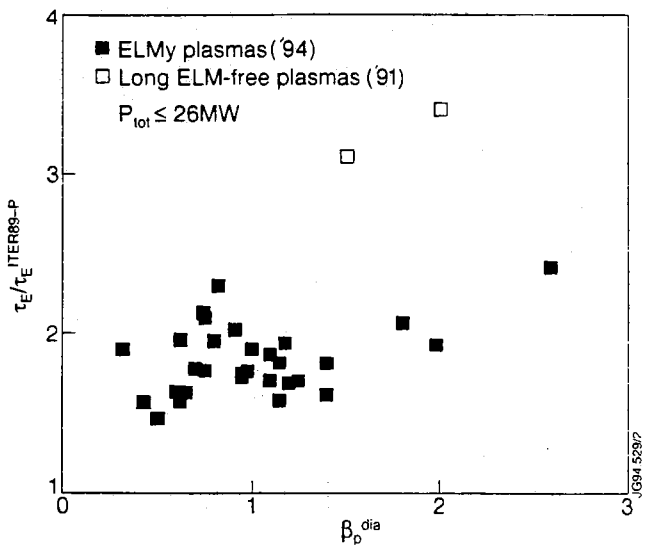

Fig. 7(b): Confinement enhancement factor against the ITER89-P scaling as a function of bpdia for high-β_p discharges with ELMy plasmas ('94) and long ELM-free plasmas ('91) in JET.

FUSION NEUTRON YIELD

An important effect of difference in the profiles between the two regimes in JT-60U and JET is manifest on the DD fusion neutron yield. Figure 8 shows the neutron rate as a function of the total additional power into the plasma in comparison with the JT-60U and JET high-β_p regimes. It is shown here that the peaked profile plasmas obtained in JT-60U produce much higher fusion power than the broad profile plasmas in JET for a given input power at the similar plasma volume and current ranges.

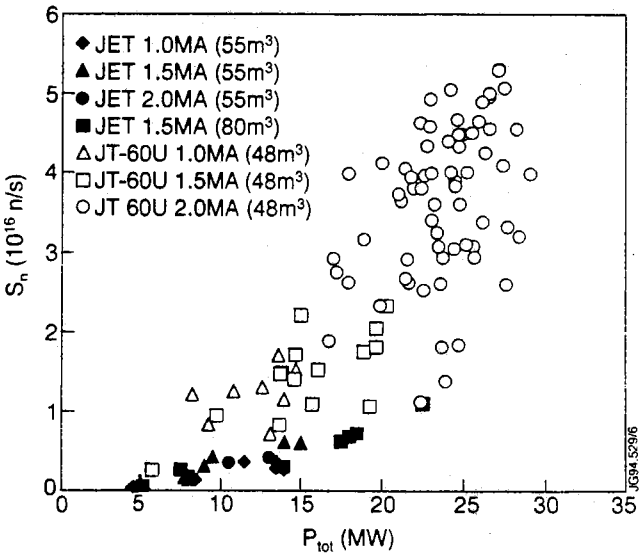

Fig. 8: Neutron emission rate as a function of total heating power for the high-β_p regimes in JT-60U and JET.

When the total ion stored energy is dominant in the plasma stored energy, the DD thermal neutron rate $S_n=(1/2)\int n_D^2\langle\sigma v\rangle dV$ within the central ion temperature of interest can be approximately expressed as $G\langle p\rangle^2 V_p$ where $\langle p\rangle$ is the total volume-averaged plasma pressure and G is a peaking factor of the pressure profile written as $\langle p(r)^2\rangle/\langle p(r)\rangle^2$. Figure 9 shows the neutron rate as a function

of $<p>d_{ia}^2 V_p$ for the JT-60U and JET high-β_p regimes, indicating that the high-β_p plasmas in JT-60U produced higher neutron rates for a given stored energy than the high-β_p plasmas in JET. This evidence may result from the differences not only in the pressure profile but also in the fraction of ion energy and/or non-thermal components of the stored energy.

In the JT-60U high-β_p regime, the concentration of the beam heating and fueling into the plasma center is found to induce a highly peaked ion pressure profile coinciding with significant reduction of ion thermal transport in the core plasma region and sometimes combined with H-mode characteristics at the edge. Without such the condition, the JET results show that the profile becomes broader with the H-mode even at the similar q and β_p regions and the resultant neutron rate is relatively low though the beam power density is increased with decreasing the plasma volume. Characteristics of the peaked profile plasmas are discussed in detail in comparison between the JT-60U high-β_p discharges and the TFTR supershots in Reference [6].

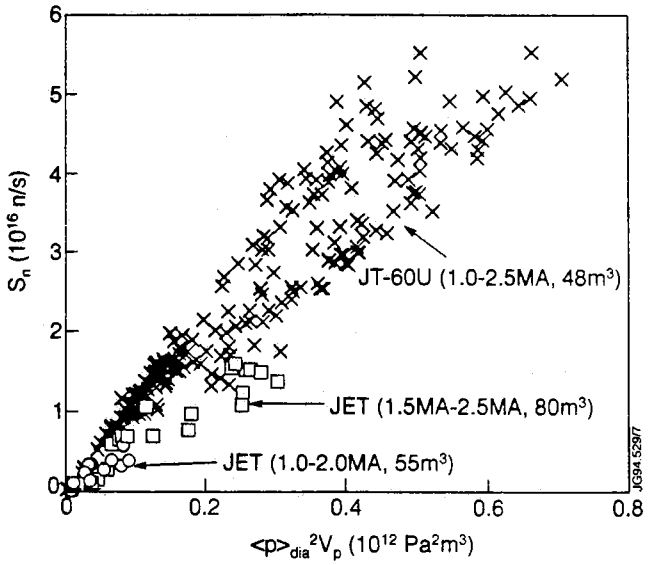

Fig. 9: Neutron emission rate as a function $<p>d_{ia}^2 V_p$ for the high-β_p regimes in JT-60U and JET including high current data up to 2.5 MA of 1994.

LONG PULSE PERFORMANCE AND OPERATING DOMAINS

A very long pulse ELMy discharge with high-β_N has been demonstrated in the JET high-β_p regime as shown in Fig.10, where a plasma at β_N~3 and β_p^{dia}~1.6 is sustained for ~7 sec. On the other hand, a high performance plasma with a peaked profile and continuous ELM activity has been sustained for ~2 sec at 1.8 MA/4.4 T in the JT-60U high-βp regime as shown in Fig.11, where β_p and β_N reached 1.4 and 1.8, respectively. In both machines, the ELMy plasma appears to be beneficial to maintain the plasma performance in a steady state since it could moderate the wall-plasma interaction preserving the core confinement unlike giant ELMs, X-events and other collapses.

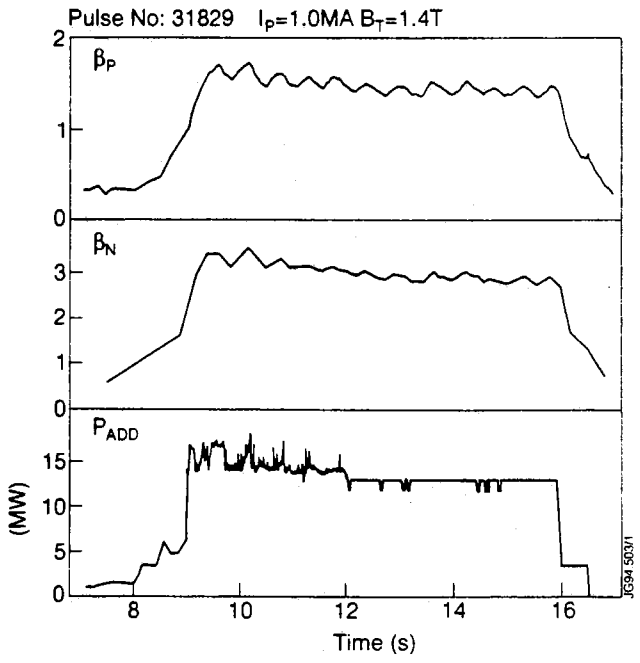

Fig. 10: Time history of a long-pulse high-β_N discharge in JET, where a high normalized beta β_N~3 is sustained for 7 sec.

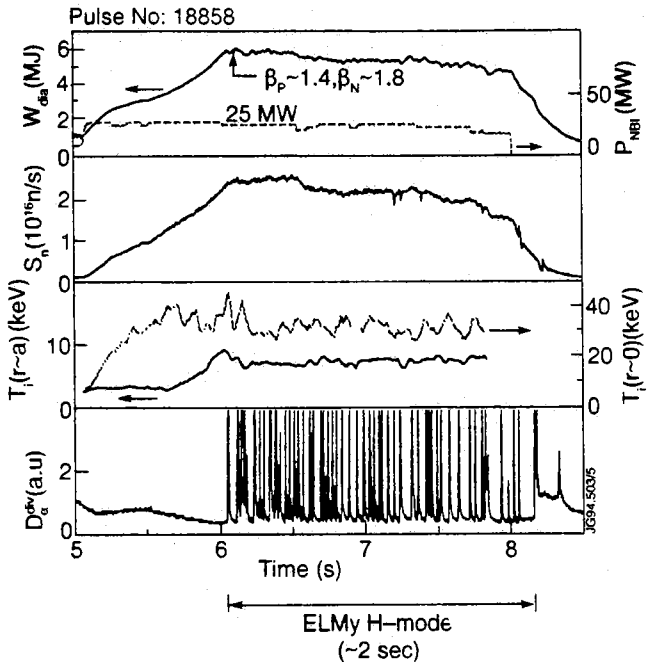

Fig. 11: Time history of a high performance discharge at 1.8 MA/4.4 T in JT-60U, where the performance is maintained for 2 sec until the beams are turned off.

A high-β_p plasma with enhanced confinement (high H-factor) and stability (high β_N) required for the advanced tokamak concepts can be achieved and sustained. However, as shown in JET and JT-60U, it most often occurs when the plasma pressure is reduced at low current and toroidal field, and has not yet been achieved for the highest performance discharges. Indeed, active profile control mechanisms would make it possible to sustain such a high performance plasma in the required β_p and β_N domains, but searching for a stable route to the high-β_p plasma will become a critical issue for the development of advanced tokamak concepts [4].

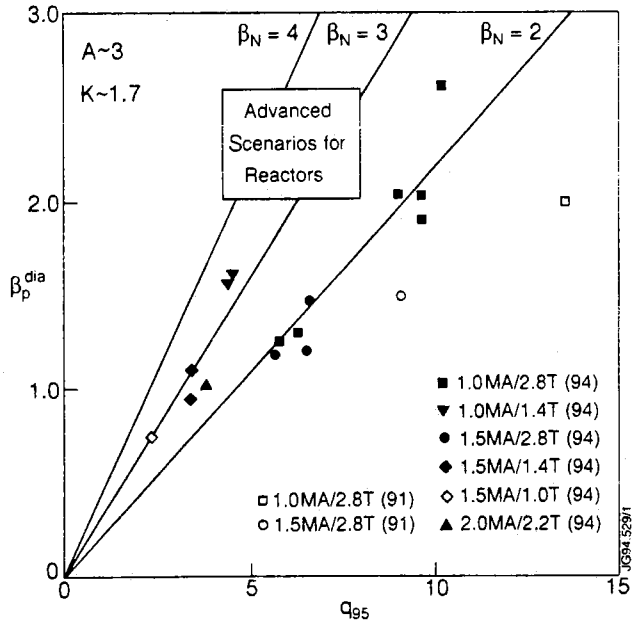

Fig. 12(a): Diamagnetic poloidal beta as a function of q_{95} for the JET high-β_p regime.

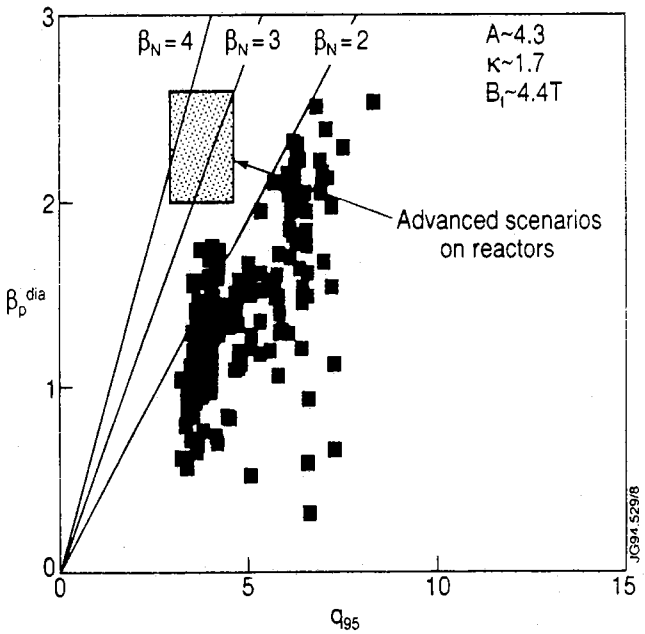

Fig. 12(b): Diamagnetic poloidal beta as a function of q_{95} for the JT-60U high-β_p regime.

The operating domains of the high-β_p regimes in JET and JT-60U are illustrated together with a goal of the advanced scenarios on reactors in Fig.12(a) and (b), respectively. In the JET high-β_p regime, the goal is approached with ELMy H-mode plasmas sustained much longer than the energy confinement times in terms of steady state whereas the JT-60U high-β_p regime aims at the goal with high performance plasmas which are often transiently terminated by MHD β-limits [7]. While there has been the clear differences in the experimental approach between the two regimes, the coincidence of the two approaches will be required for determining whether the reactor scenarios are workable.

CONCLUSIONS

- The high-β_p regimes in JET and JT-60U have for the first time been compared, in which steady state and high performance plasmas at high-β_p have been explored, respectively.
- The confinement enhancement factor against the ITER89-P scaling is significantly increased with β_p for ELM-free plasmas in a transient state both in JT-60U and JET, but is constant for JET ELMy plasmas in a steady state.
- Results from small/large volume experiments in JET show no difference in energy confinement in spite of reducing the plasma volume with the same major radius, suggesting that the major radius can be the dominant size parameter for determining the energy confinement and the high aspect ratio be beneficial to the fusion triple product in ELMy plasmas at high-β_p since the higher pressure $<nT>$ was obtained at the same τ_E values for the high aspect ratio plasma.
- The peaked profile plasmas are found to produce much greater neutron rate than the broader profile plasmas in comparison between the two regimes, which may result from the differences in the ion pressure profile and fraction of ion pressure and non-thermal components in the stored energy.
- A steady state plasma has been produced at β_N~3 and β_p^{dia}~1.6 for ~7 sec in JET. A high performance plasma has been achieved for ~2 sec in JT-60U. However, long sustainment of a high-β_p plasma at high-β_N with high performance has not been demonstrated yet in both machines.

ACKNOWLEDGMENTS

One of the authors (S. Ishida) would like to express his appreciation to the members of the Tokamak Concept Improvements Task Force in JET and the Confinement Theme Group in JT-60U for their contributions and collaborations to this work, and to Drs. H. Kishimoto and J. Jacquinot for their support and encouragement.

REFERENCES

[1] S. Ishida et al., Plasma Phys. and Control. Nucl. Fusion Research (1992), Vol.1, 219 (IAEA, Vienna, 1993)
[2] Y. Koide et al., Phys. Rev. Lett. 72(1994)3662.
[3] C. Challis et al., Nucl. Fusion 33(1993)1097.
[4] C. Gormezano et al., Plasma Phys. and Control. Nucl. Fusion Research (Proc. 15th Int. Conf. Seville, 1994), paper IAEA-CN-60/A-5-I-3
[5] T. Fukuyama et al., Plasma Phys. Control. Fusion 36(1994)1385.
[6] H. Park et al., Plasma Phys. and Control. Nucl. Fusion Research (Proc. 15th Int. Conf. Seville, 1994), paper IAEA-CN-60/A2/4-P-1.
[7] S. Ishida et al., to be published in Proc. 21th European Conference on Controlled Fusion and Plasma Physics, Montpellier, 1994.

High Performance Plasmas with the JET Pumped Divertor in JET

R W T König, S Ali-Arshad, M Bures, J P Christiansen, H P L de Esch, G Fishpool, M von Hellermann, T Hender, O N Jarvis, T T C Jones, K D Lawson[1], P J Lomas, A C Maas, F B Marcus, M F F Nave, R Sartori, B Schunke, P Smeulders, D Stork, A Taroni, P R Thomas, K Thomsen and the JET Team.

JET Joint Undertaking, Abingdon, Oxfordshire, OX14 3EA, UK.
[1] UKAEA Fusion, Culham, Abingdon, Oxfordshire, OX14 3DB, UK.

High Performance Plasmas with the JET Pumped Divertor in JET

R W T König, S Ali-Arshad, M Bures, J P Christiansen, H P L de Esch, G Fishpool, M von Hellermann, T Hender, O N Jarvis, T T C Jones, K D Lawson[1], P J Lomas, A C Maas, F B Marcus, M F F Nave, R Sartori, B Schunke, P Smeulders, D Stork, A Taroni, P R Thomas, K Thomsen and the JET Team.

JET Joint Undertaking, Abingdon, Oxfordshire, OX14 3EA, UK.
[1] UKAEA Fusion, Culham, Abingdon, Oxfordshire, OX14 3DB, UK.

INTRODUCTION

During the shutdown, which ended early this year, internal divertor coils, a new toroidally continuous array of Carbon Fibre Composite (CFC) divertor tiles and a toroidally continuous cryo-pump have been installed, still allowing for operation at up to 6 MA. Since the next DT experiment in JET is planned at the end of 1996 it is necessary to optimise the fusion performance in the new JET pumped divertor configuration in regimes with steady state potential as well as in those with maximum fusion yield.

VESSEL CONDITIONING AND ITS IMPACT ON PLASMA PERFORMANCE

- Util October the JET-PD vessel was only baked and operated at 250 °C (now 320 °C) to avoid the possibility of damage to the divertor coil epoxy (old JET was baked to 350 °C and operated at 300 °C).
- The new divertor tiles are mounted on water cooled supports (kept at ~40 °C between pulses).
- Inner wall is now much less covered with carbon tiles and the outer wall is not at all covered with carbon tiles, except at the locations of the poloidal limiters, which replace the old belt limiters.

A cryo-pump has been installed with a measured speed of 170 m^3s^{-1}. In an experiment, in which the plasma density was held constant by gas-puffing (the result was found to be independent of fuelling position), a max. deuterium removal rate of $8 \cdot 10^{21}$ s^{-1} in an Ohmic plasma with $\langle n_e \rangle = 4 \cdot 10^{19}$ m^{-3} has been achieved [Cam94]. Moving the outer strike point of the plasma across the horizontal and up the vertical target plate by up to 20 cm away from optimum position, resulted in a reduction of the pumping efficiency by a factor of 2. Even 20 cm from the pump entrance the particle removal rate should therefore be high enough to cope with the maximum particle input from the NBI (at P_{NBI} = 18 MW about $1.5 \cdot 10^{21}$ s^{-1}). Pressure measurements during hot- ion ELM-free H-modes suggest pumping of the order of 60 % of the beam fuelling, whilst the average plasma bulk density is rising 1-1.2 times

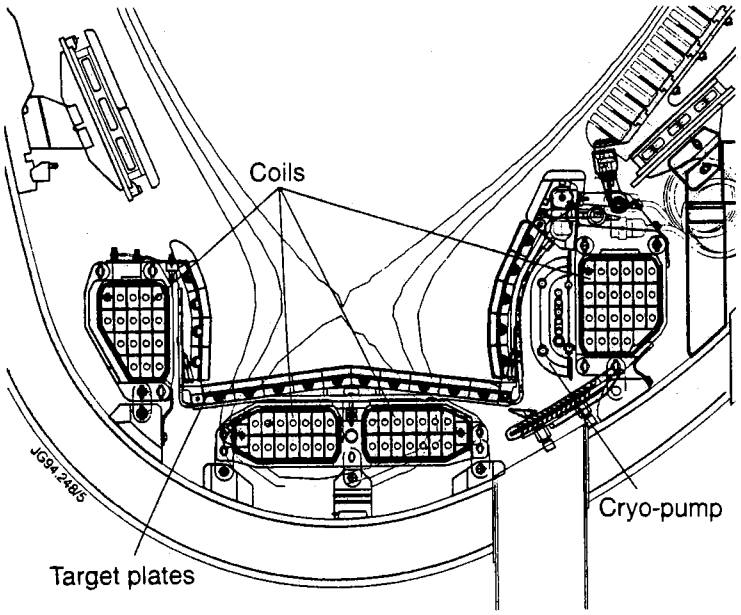

Fig. 1: Cross section of the JET Pumped Divertor showing the major components

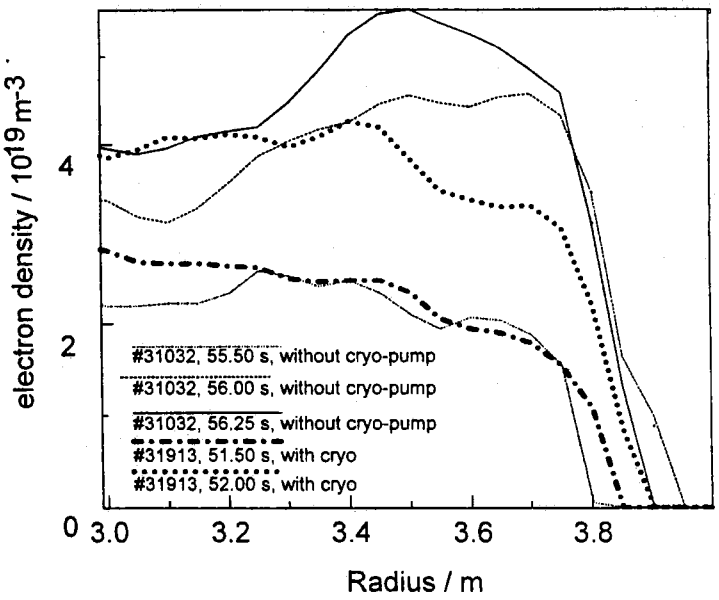

Fig. 2: Evolution of the electron density profiles with full cryo-pump (#31913, P_{NBI} = 15 MW) and without cryo-pump. (#31032, P_{NBI} = 13.5 MW) for hot-ion mode plasmas from the beginning of the high power NBI heating phase onward untill just before the end of the ELM-free period.

the beam fuelling. During the subsequent ELMy phase the pumping can be as large as 9 times the beam fuelling (no gas fuelling), while the core plasma density is constant. Clearly a particle reservoir is being depleted.

- The vacuum conditions are very similar to those in previous campaigns and are even considerably better than previously when the divertor cryopump is used.
- To reduce the main chamber recycling in JET Be-evaporation (2 or 4 heads) plus He GDC is used. The fast density rise and the hollow density profiles during the ELM-free phase give a clear indication that the recycling in the new machine is considerably higher than in the old JET. First the use of half the cryo-pump and later of the full cryo-pump reduced the recycling sufficiently for the neutral beam fuelling to dominate the wall source. This then finally led to the peaked density profiles which are ideal for hot-ion modes due to the increased central beam deposition (Fig. 2).
- A tile heating experiment showed that increasing the divertor surface temperature to 1000 °C has litte effect on the recycling. The subsequent high power ELMy phase was unchanged whether or not sweeping was used to keep the tile temperature down.
- In hot-ion pulses a significantly higher neutral pressure was found in the divertor than in the midplane and following an ELM the pressure rises rapidly in the divertor but much more slowly at the midplane. This suggests that the neutrals arise in the divertor.

TERMINATION OF THE HIGH PERFORMANCE PHASE

Variety of termination scenarios (similar to the types observed in the old machine); these include

- fast terminations where a sawtooth is coupled to an ELM
- slow terminations where the confinement seems to be lost at the outer part of the plasma first and the limitation of the temperatures moves inward to the centre. Fig. 3 shows such a case which is clearly ELM limited.
- slow termination (neither sawtooth nor ELM(s)); in long ELM-free periods rising density and increasing radiation similar to old JET behaviour and ELM-free period often limited by return to L-mode (Fig. 4).
- but **no carbon bloom** as a result of good divertor design (usually $Z_{eff} < 2 - 2.5$)

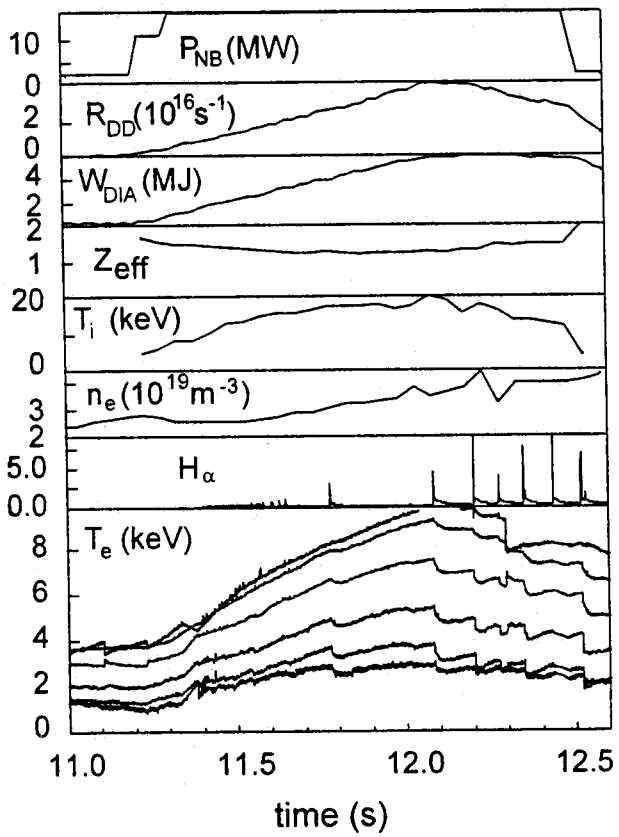

Fig. 3: Time traces for hot-ion pulse #31905 with low main chamber recycling obtained by cryo pumping for a standard fat plasma (δ=0.2).

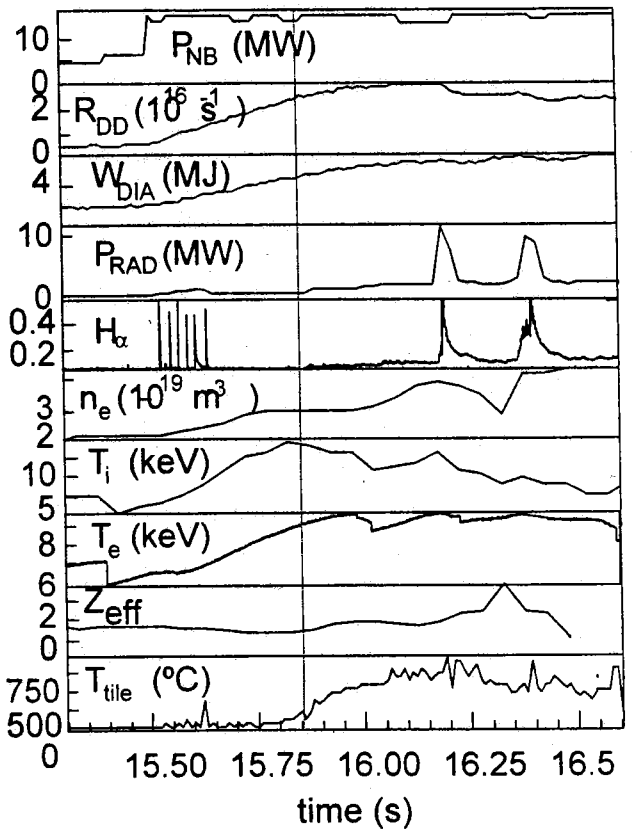

Fig. 4: Time traces for hot-ion pulse #31917 with low main chamber recycling obtained by cryo pumping for a high triangular plasma (δ=0.4).

In the old JET

ELMs rarely found, they were only present just above the L-H transition threshold, with extremely strong gas puffing, at high beta or in hydrogen plasmas.

In the new JET-PD

ELMy H-modes are the norm in the high recycling conditions. Long ELM-free periods are difficult to achieve. ELMs have the characteristics of the 'giant' ELMs identified on DIIID or ASDEX-U. The ELM frequency increases with input power and tends to reduce with plasma current. Experiments have shown that the ELM-free period is hardly influenced by different conditioning schemes, divertor tile heating, X-point to target distance, diverted plasma flux expansion, sweeping, or use of top X-point tiles [Lom94].

ELM-free period can be influenced by:

- minimum gas input to reduce recycling
- use of cryo-pump to reduce recycling
- triangularity (higher values increase edge shear which increases ideal ballooning limit to pressure gradient near the separatrix)
- A scan of elongation, triangularity and strike point location at constant power, plasma current, toroidal field and target density shows that increase of triangularity from 0.2 to 0.35 can extend ELM-free period from 0.3 to 2.0 sec. (high triangularity similar to old JET configurations)
- ELM-frequency increases strongly with power and decreases with plasma current in a similar manner to that observed on ASDEX and DIIID.

present hypothesis: **"Proximity to ideal ballooning limit determines the ELM-free period."**

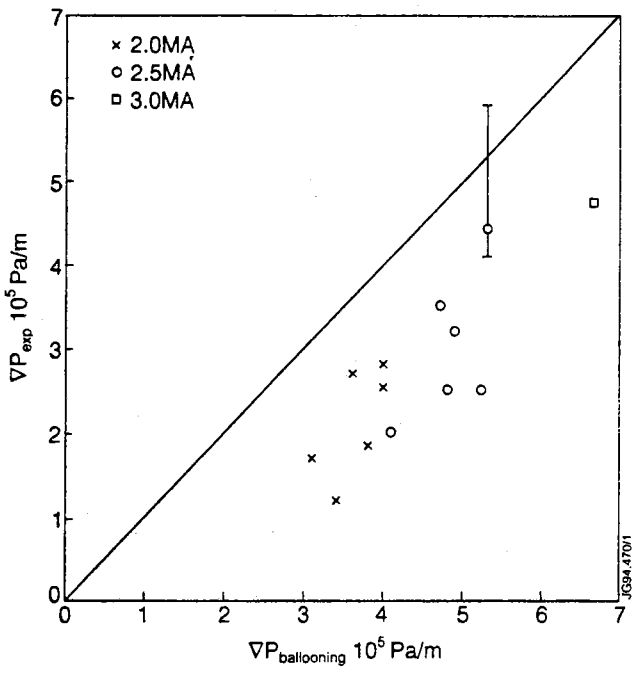

Fig. 5 Best estimate of the edge pressure limit against the calculated ideal ballooning limit. The upper limit of the error bar is the gradient one would get if the fall-off length were 3 cm

The theoretical pressure gradient limit has been calculated at 95% flux surface using EFIT reconstructions of plasma equilibria. Fig. 5 shows how close the gradients calculated from the outermost 3 LIDR points (5 cm resolution) are to the calculated Ballooning limit. The hypothesis is further supported by the fact that one also finds some of the right systematic dependencies like:

a) ELM stability (i.e. the time between the L-H transition till the first ELM) seems to be improved by increased edge shear

b) ELM stability is improved by increasing the triangularity of the equilibrium

If hypothesis is correct the ELM-free period is determined by the time to reach the edge ballooning limit.

CORRELATION BETWEEN GIANT ELMS AND FLUCTUATIONS

1. Magnetics

a) giant ELMs have long lived high frequency precursors (Fig. 6), which often saturate in amplitude before the ELMs. That means no direct cause and effect is observed between the precursor and the ELM.

b) giant ELMs also have low frequency precursors with a low n character

c) giant ELMs themselves have a strong low frequency low n component

During the ELM-free periods high frequency modes (>30 kHz) are observed. These modes, which have a complex frequency structure, appear with the L to H transition and disappear at the end of the H-mode. The modes are modulated by giant ELMs and are saturated in high triangularity discharges (Fig. 7).

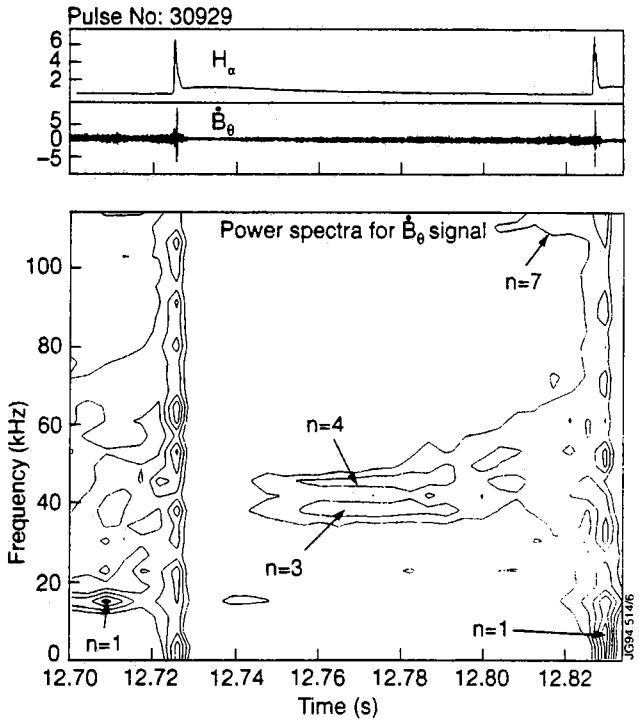

Fig. 6: High frequency precursor

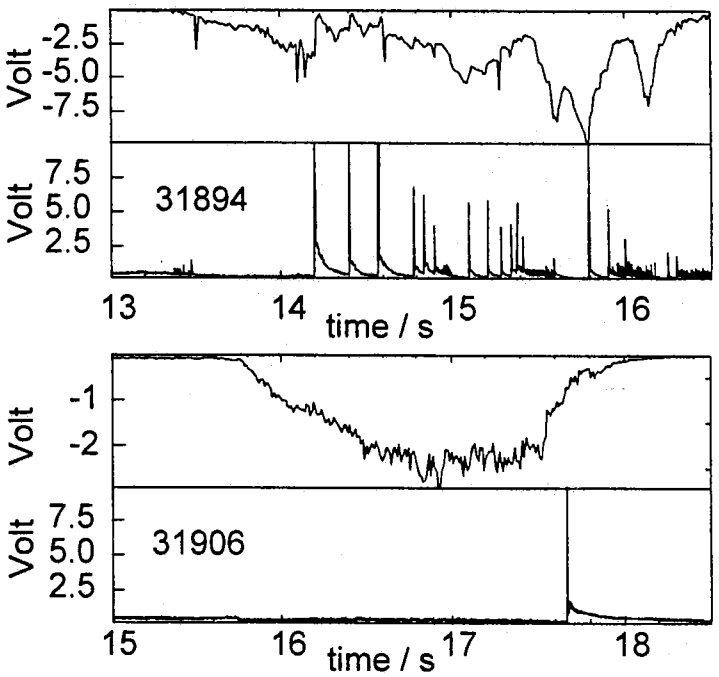

Fig. 7: Comparison of high frequency mode amplitudes (here at 43 kHz)for a low triangularity (δ=0.2) plasma (#31894) and a high triangularity (δ=0.4) plasma (#31906).

2. Reflectometer data analysis

a) high frequency precursor appears to move radially outwards

b) amplitude peaks near the plasma edge (chan 3 or $n_e = 1.06 \cdot 10^{19}$ m^{-3})

c) high frequency precursor causes a flattening of the density profile near the edge [Col93]. The larger gradients at the edge of the plateau, created by the high frequency precursor, could then destabilise other modes.

d) the broad frequency band is short lived (<1ms) and finishes when H_α reaches the maximum; apart from the low frequencies the ELM is followed by a quiescent period over a certain radial range (Fig. 8). The broad band is mostly observed within the last 6 reflectometer channels (<10cm) although the ELM may be affecting T_e and T_i right through the plasma centre (Fig. 3).

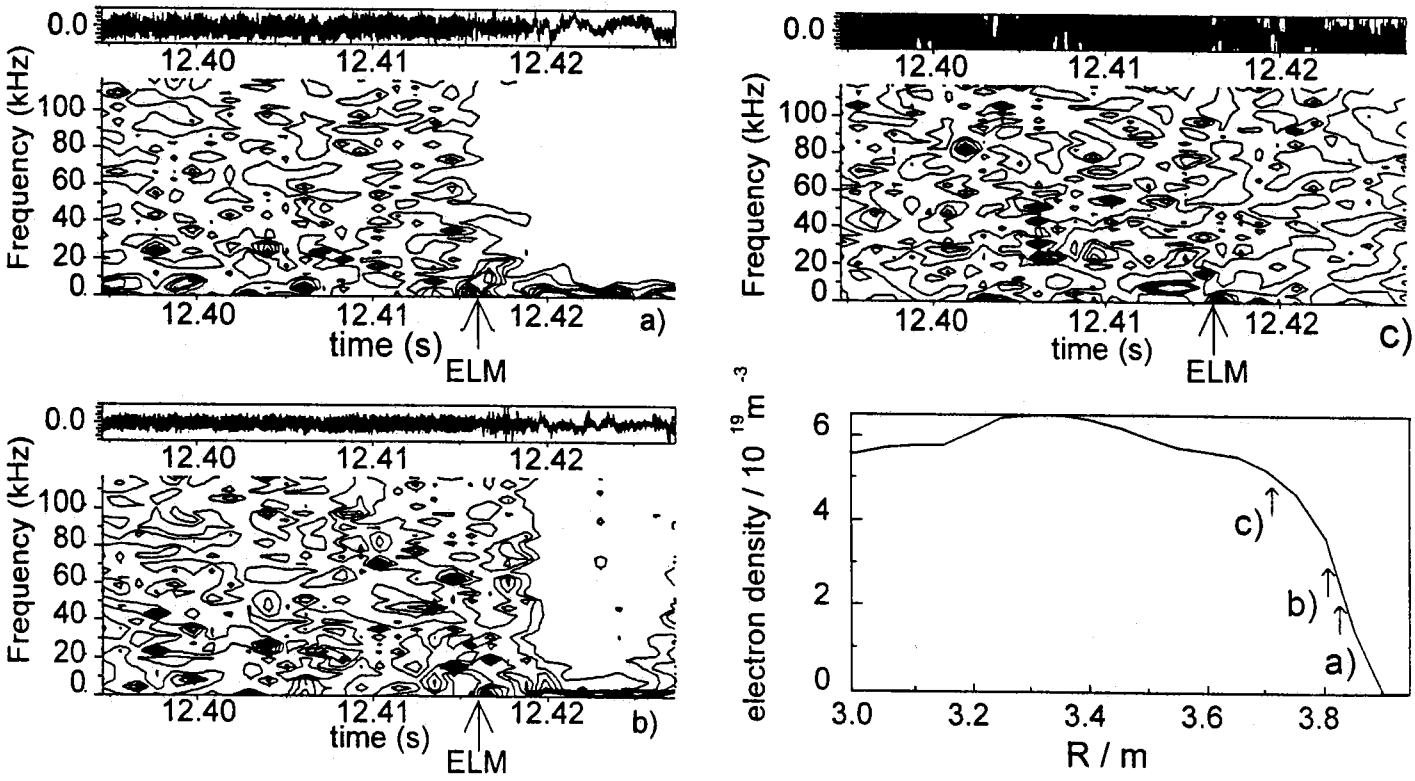

Fig. 8: A broad band of high frequency fluctuations is observed with the reflectometer just before the ELM (#31906). a) shows channel 6 which is representative for all other channels further outside (chan 1-5). At b) (chan 7) the quiescent period after the ELM starts to disappear while from chan 8 onward the quiescent period disappears totally. c) shown above corresponds to chan 9.

FUSION PERFORMANCE

Operating space

operated at I_p = 1 - 4 MA and B_T = 1 - 3.4 T in different configurations

L to H transition power threshold

essentially unchanged from the 1991/2 carbon tile campaign with grad **B** drift towards the X-point (normal drift direction) and slightly lower than the old data with reversed grad **B** direction

Performance

The $n\tau T$-diagram in figure 9 shows the fusion performance that has been achieved so far with the new JET-PD in comparison with the old machine [Sto94]. The best 4MA/3.4T shot from this year is one of the best non hot ion modes achieved so far, obtained with 18 MW NBI heating. It would have $Q_{DT} \sim 0.1$ for a 0:50 D:T plasma mixture during the ~2 s ELMy phase. The best hot-ion H-mode discharge in the new machine has reached $n\tau T = 5.6 \cdot 10^{20}$ m^{-3} s keV which is about 60% of best previous value, $Q_{DT} \sim 0.6$.

Energy confinement in ELMy and ELM-free H-modes

The energy confinement time: over the range from 1 to 4 MA and toroidal fields from 1 to 3.4 T appears to be between 90 and 100 % of the ELM-free H-mode predictions (ITERH93-P). Fig. 10 shows a comparison of the measured diamagnetic energy confinement time versus the ITER89-P scaling for ELMy and ELM-free H-modes.

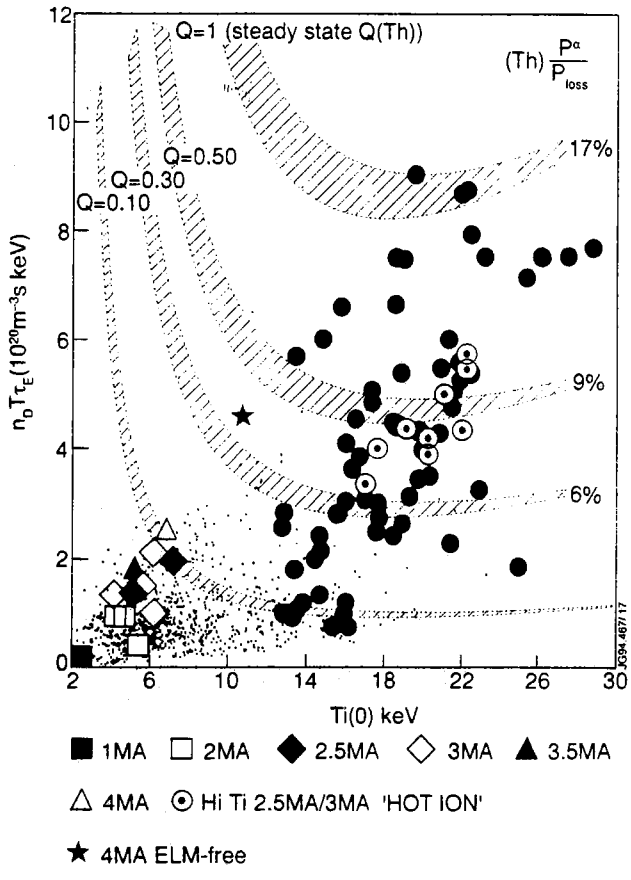

Fig. 9: Triple fusion product plotted against central ion temperature (Ti(0)) The JET-PD hot-ion H-modes are marked with open circles with a dot. The filled circles represent the 1991/92 hot-ion H-modes . The remaining data are JET-PD steady-state (>4τ_E) H-modes.

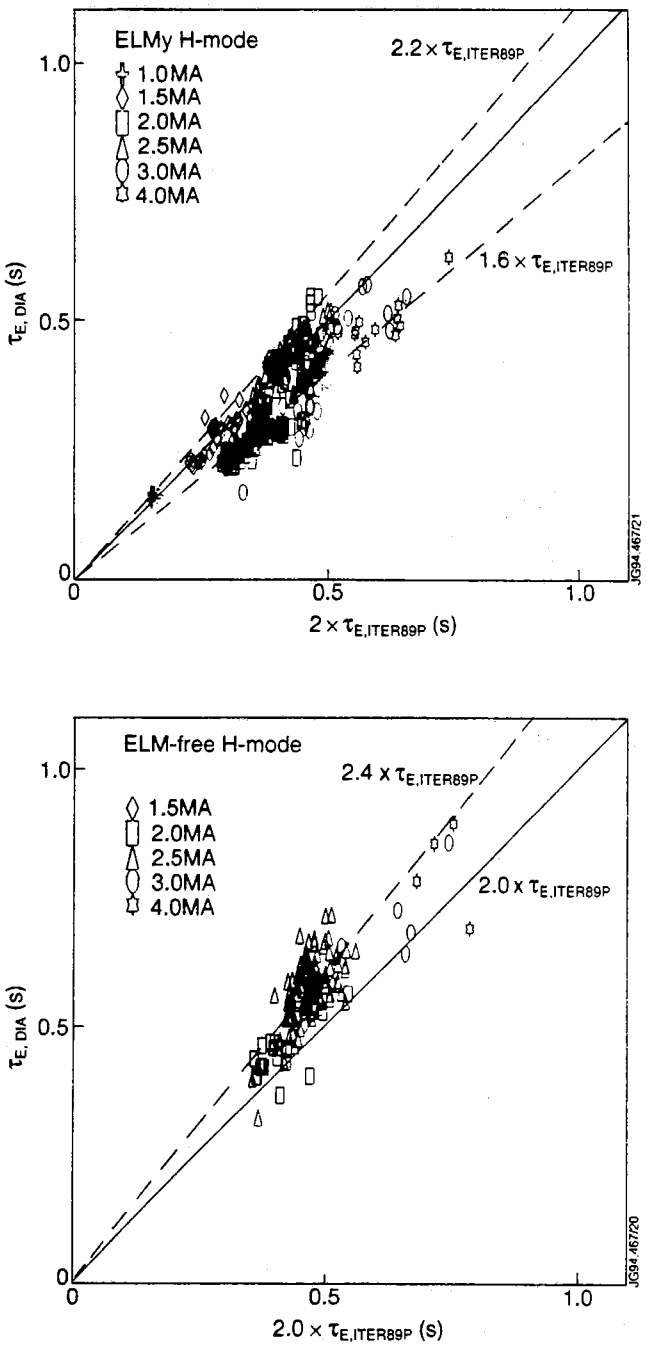

Fig. 10: Measured diamagnetic energy confinement time for the JET-PD ELMy and ELM-free H-mode dataset (t-ELM-free > 0.5 s) plotted against 2x the prediction from the ITER89-P scaling law. The ELM-free data selected have dW/dt < 0.4 P_{in}, the ELMy data dW/dt < 0.1 P_{in}.

Hot-ion H-modes

The hot-ion H-modes were optimised for high fusion yield for the PTE1 experiment in 1991. They were developed to a regime which showed VH-mode confinement (H-fact. >3 rel. to L-mode). It has been tried to regain that regime with the new JET-PD by optimising the 2.8T/2.5MA discharge (PTE: 2.8T/3.2MA).

a) Ion temperatures of $T_i(0) > 20$ keV have been reached with $T_i(0) > 2\ T_e$ for up to 0.75 sec. The preparation of slightly peaked target density profiles by careful gas and pumping programming as well as the use of the cryo-pump is essential for the good beam penetration needed to achieve high central parameters and neutron yields. T_i and T_e values similar to those of the best 1991/2 shots were reached, but only about half the stored energy and neutron yield have been achieved. The highest DD reaction rate reached this year was $4.5 \cdot 10^{16}\ s^{-1}$.

b) It seems that with the new JET-PD VH-mode confinement has not yet been achieved.

Possible reasons:

- still higher edge density gradients than in 1991/2 due to higher recycling
- edge plasma is not generating the levels of bootstrap current required for unconstrained access to the second stable region against ballooning modes, which has been identified as a signature of the VH-mode in JET and DIIID. The hot-ion H-modes produced in with the new machine stand out from the rest of the ELM-free dataset as having enhanced confinement. The highest value reached so far in the new JET-PD is $2.9 \cdot \tau_{E,\ ITER89\text{-}P}$ (triang. δ=0.1-0.3, old JET δ=0.35-0.5).

CONCLUSIONS

Up to now H-mode divertor operation has been demonstrated at plasma currents up to 4 MA and in the hot-ion H-modes about half the performance of the best ones with the old machine have been achieved. In contrast to the old machine in which it was difficult to produce ELMs, the H-modes in the new JET-PD are typically either ELMy with steady state density and confinement close to ELM-free values or have an early ELM-free period, the length of which can be influenced, during which the density rises very fast due to the, for reasons which are still not understood, considerably higher recycling in the new machine. Due to the good divertor design the performance of JET is no longer limited by the carbon bloom.

REFERENCES

[Cam94] D Campbell, IAEA Conference 1994, IAEA-CN-60/A-4-I-4

[Col93] A Colton, Ph. D thesis, Riso National Laboratory Report Riso-R-700(EN), 1993

[Lom94] P Lomas. IAEA Conference 1994, IAEA-CN-60/A-2-I-4

[Sto94] D Stork, IAEA Conference 1994, IAEA-CN-60/A-1-I-3

Comparison of Vertical and Horizontal Target Plate Operation with the JET Mark I Divertor

C G Lowry, D O'Brien, D J Campbell, S Clement, S Davies, H Y Guo[1], J de Haas, P J Harbour, L D Horton, J Lingertat, A Loarte, G F Matthews, K McCormick[2], R D Monk[3], G J Radford, G R Saibene, A Taroni, G C Vlases.

JET Joint Undertaking, Abingdon, Oxfordshire, OX14 3EA, UK.
[1] INRS-Energie et Materiaeux, University du Quebec, Quebec, Canada.
[2] Max-Planck-Institut für Plasmaphysik, EURATOM Association, 85748 Garching, Germany.
[3] Royal Holloway College, University of London, London, UK.

Comparison of Vertical and Horizontal Target Plate Operation with the JET Mark I Divertor

C G Lowry, D O'Brien, D J Campbell, S Clement, S Davies, H Y Guo[1], J de Haas, P J Harbour, L D Horton, J Lingertat, A Loarte, G F Matthews, K McCormick[2], R D Monk[3], G J Radford, G R Saibene, A Taroni, G C Vlases.

JET Joint Undertaking, Abingdon, Oxfordshire, OX14 3EA.

[1] INRS-Energie et. Materiaeux University de Quebec, Quebec, Canada.

[2] Max-Planck-Institut für Plasmaphysik, EURATOM Association, 85748 Garching, Germany.

[3] Royal Holloway College, University of London, London, UK.

ABSTRACT

In the JET new Mark I divertor it is possible to operate with the divertor plasma strike zones on either the horizontal or vertical target plates. In the former case, the recycling neutrals are reflected away from the separatrix, and in the latter, towards it. 2D modelling [1] predicts differences between the two cases with respect to divertor recycling patterns, plasma temperature and density at the target, neutral leakage, midplane SOL density profiles, and access to the detached divertor regime. Experimentally, ohmic discharges have shown little difference in the gross behaviour, with detachment occurring at a similar core density. Langmuir probes imbedded in the target have been used to measure profiles of electron temperature and particle flux at its surface, these show many of the qualities predicted by the codes. Experiments with additional heating have also been performed, including an attempt to control the gas input by feedback on the ion saturation current to a target probe. The level of fluctuations in heated discharges has made it difficult to compare the different target orientation. In this poster data is presented for both horizontal and vertical target configurations and compared to the trends given by the modelling.

CONFIGURATIONS

- All-round high clearance to vessel wall.
- Vertical target case has twice X-point height of horizontal target case (46cm and 24cm).
- Plasma current is 2MA.
- B_T is negative (z is upwards). Ion ∇B drift is towards the target.

- Gas fuelling is toroidally uniform from modules positioned in the centre of the target.
- The strike points can be swept across the target in both configurations.

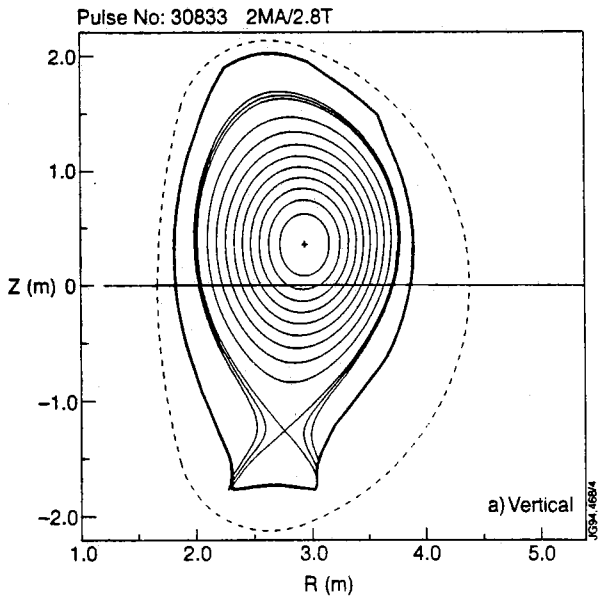

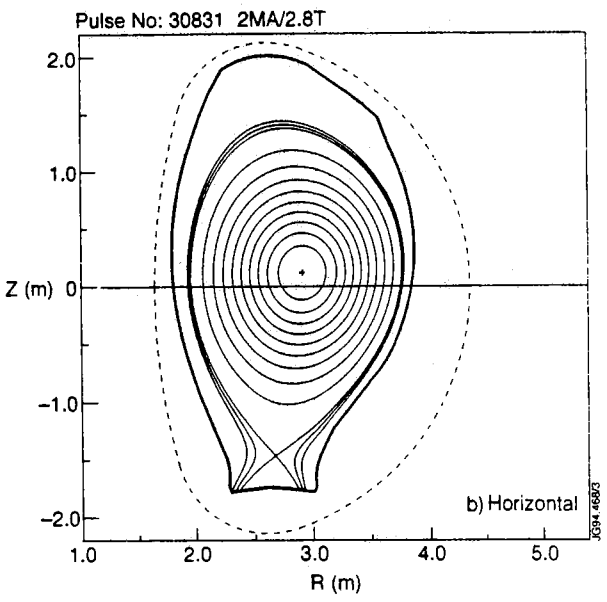

OHMIC DETACHMENT

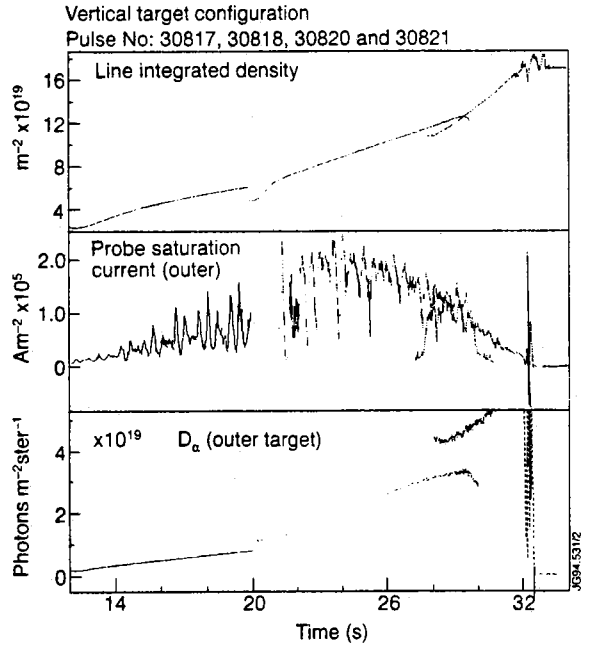

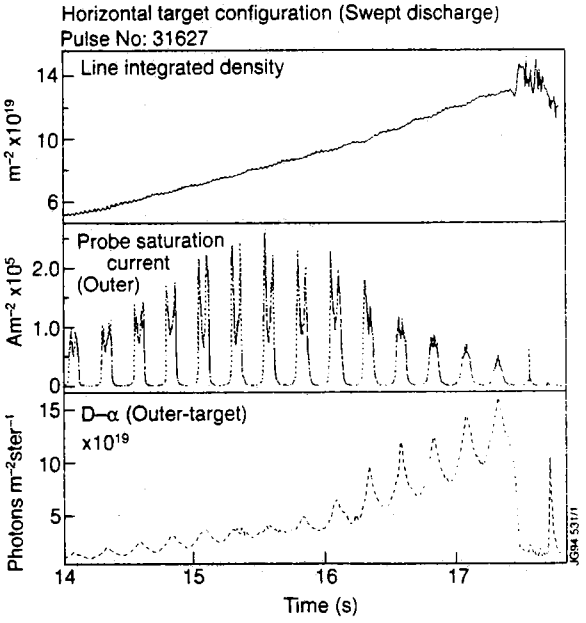

A density ramp in each configuration is shown. The vertical target case is constructed from four consecutive discharges which are similar except for the gas fuelling rate. An offset has been applied to the time axis to display most clearly the detachment. The horizontal target case is a discharge in which the strike points were swept across the target. The spikes in the ion saturation current trace are therefore the peak values in the profile. The two configurations are indistinguishable in their behaviour. Initially the ion saturation current and D_α increase with the line integrated density, then the ion saturation current rolls over whilst the D_α and density continue to increase. Finally a MARFE forms and the D_α signal drops dramatically. Although not shown, it is observed that the roll-over in ion saturation current occurs first at the inner strike region.

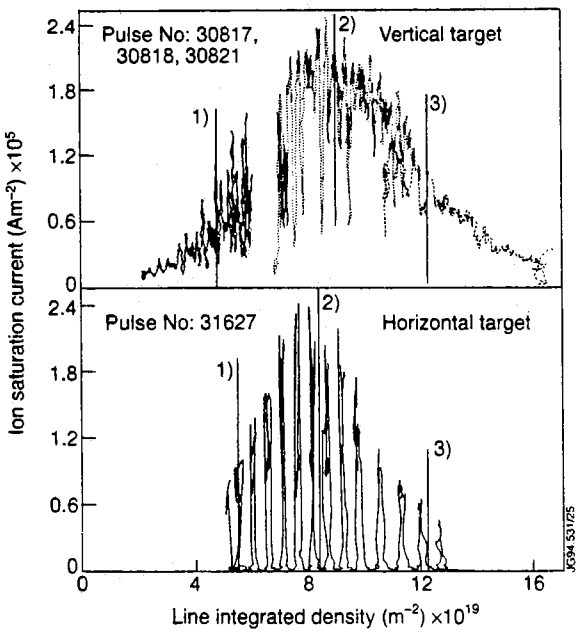

- The roll over in ion saturation current occurs at a similar core density for horizontal and vertical target discharges.

VERTICAL TARGET

Target Profiles

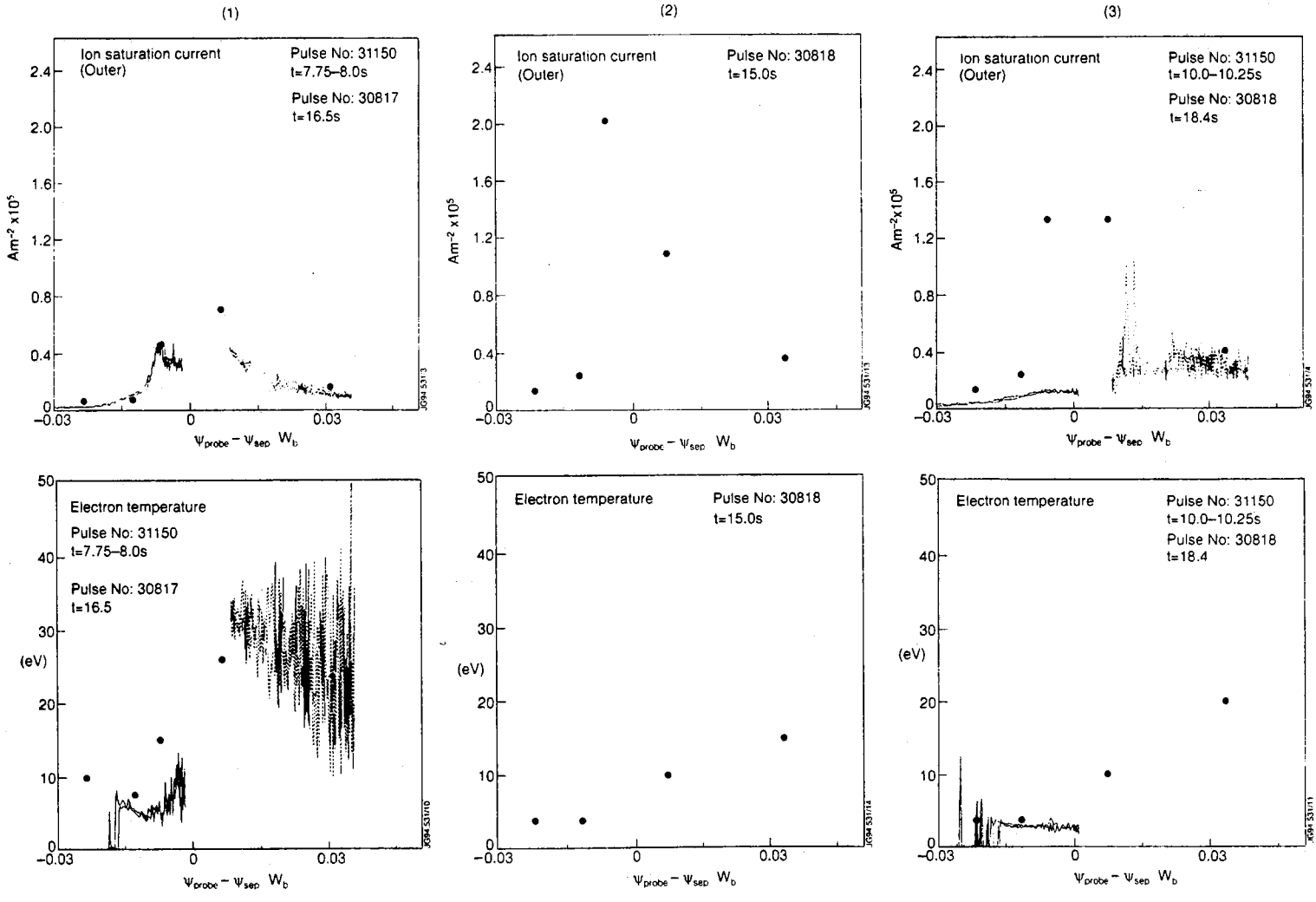

Ion saturation current and electron temperature profiles at the outer target are plotted as a function of magnetic flux from the separatrix for three density slices; 1/ increasing ion saturation current, 2/ ion saturation current roll over, 3/ decreasing ion saturation current. The solid points are the data from the unswept discharges previously shown (30817-30821); these are supplemented by data from a similar swept discharge for the increasing and decreasing ion saturation current. No swept data was available at the roll over with negative toroidal field, but data taken with positive toroidal field does show similar profiles (see below).

- Inverted electron temperature profile.
- Absolute positioning of separatrix subject to large uncertainties

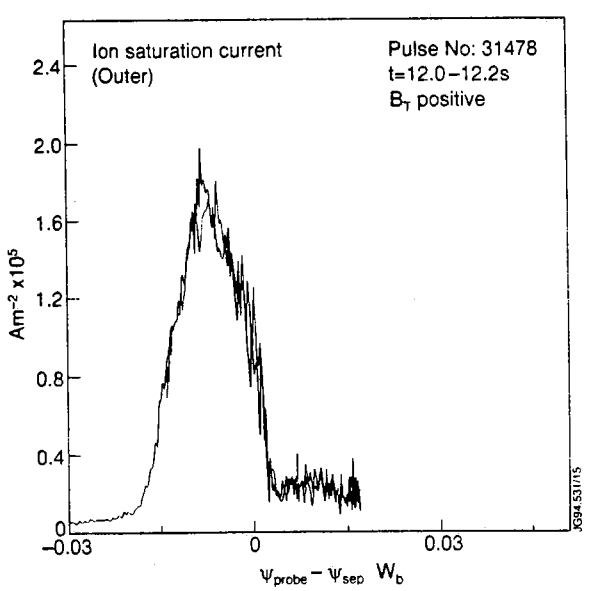

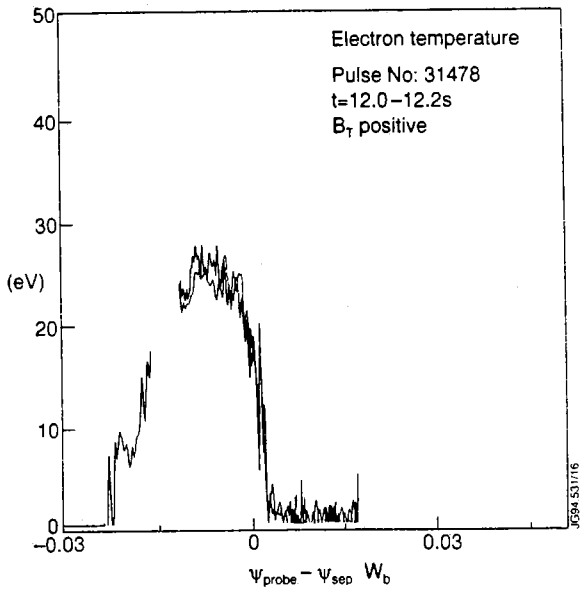

Target profiles of electron temperature and ion saturation current for a positive toroidal field case at a similar density to that of roll over in the above cases.

HORIZONTAL TARGET

Target Profiles

Companion profiles for those on the vertical target measured in the swept discharge shown (31627).

- Electron temperature profiles generally quite broad.
- Inverted electron temperature profile at high density.

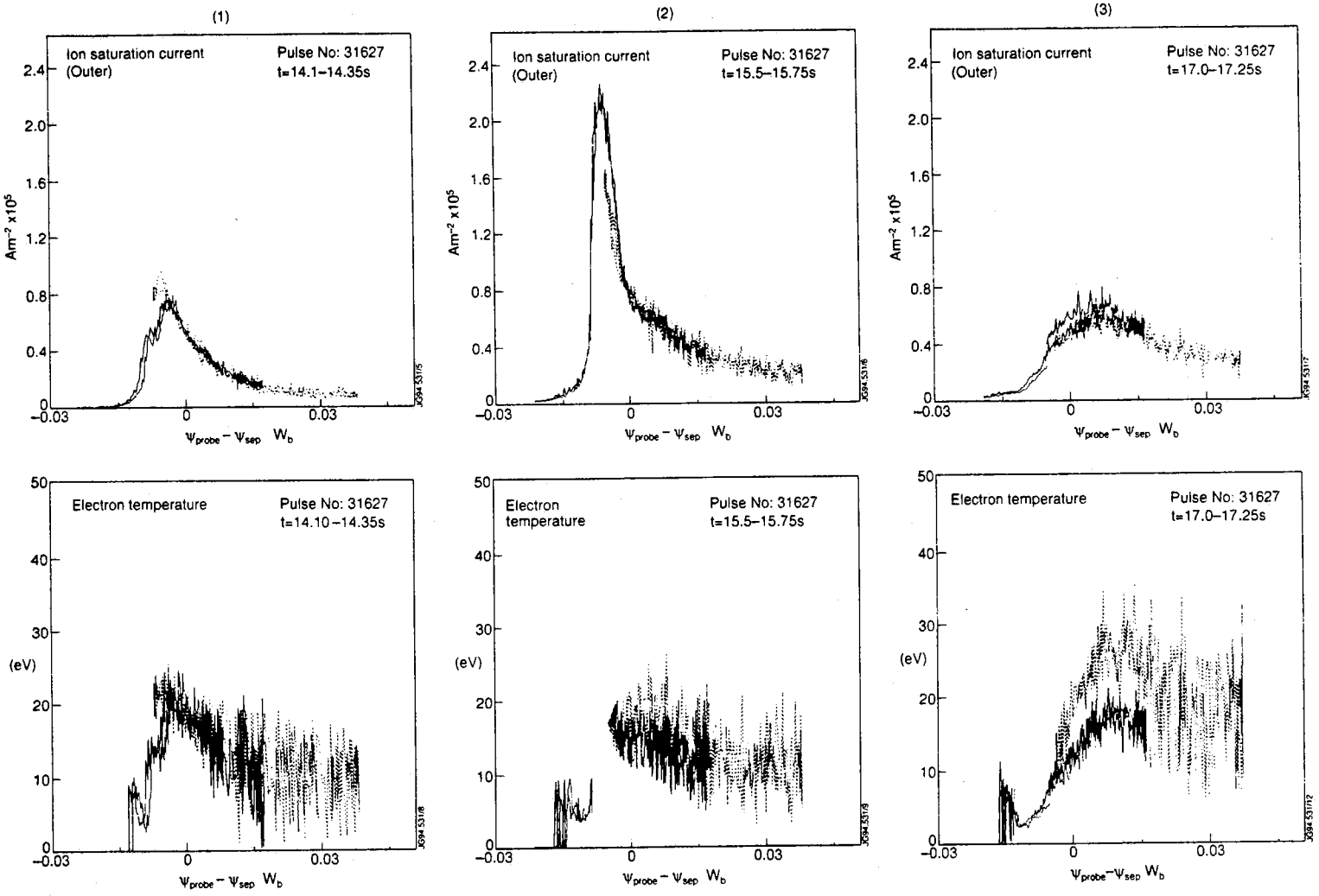

MODELLING

- EDGE2D/U 2D fluid code linked to NIMBUS monte-carlo neutral code
- $D = 0.1\ m^2s^{-1}$; $\chi = 1\ m^2s^{-1}$ in all cases, no pinch term.
- Negligible impurity radiation enhancement used (0.125MW).
- Power into scrape-off layer constant (P_e=P_i=0.5MW).
- Prescribed inventory determined from line integrated density and scaling obtained using reciprocating probe at top of vessel.

Detachment

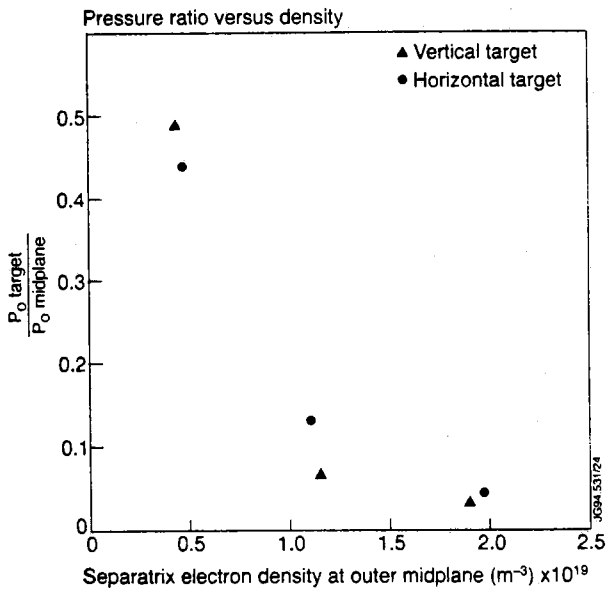

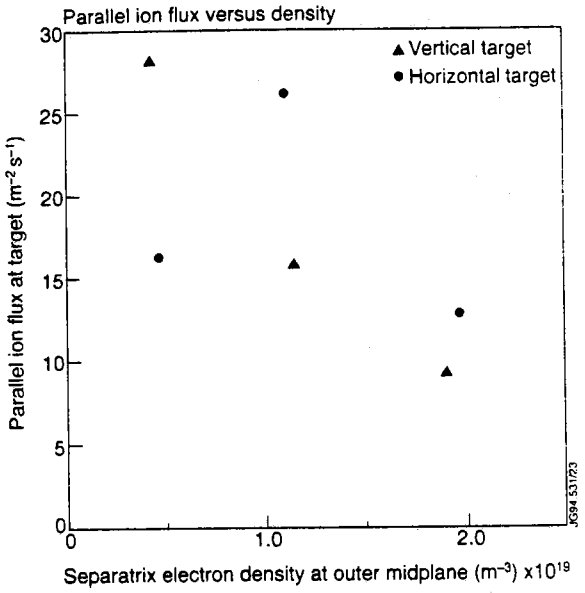

A measure of detachment used in modelling is the pressure ratio between the target and the stagnation point. This plot shows this ratio at the separatrix for simulations using an inventory consistent with the experimental data for horizontal and vertical target discharges.

- The model shows pressure detachment to occur at lower density than the ion saturation current roll over.
- Ion saturation current roll over consistent with experimental observation.

Target Profiles

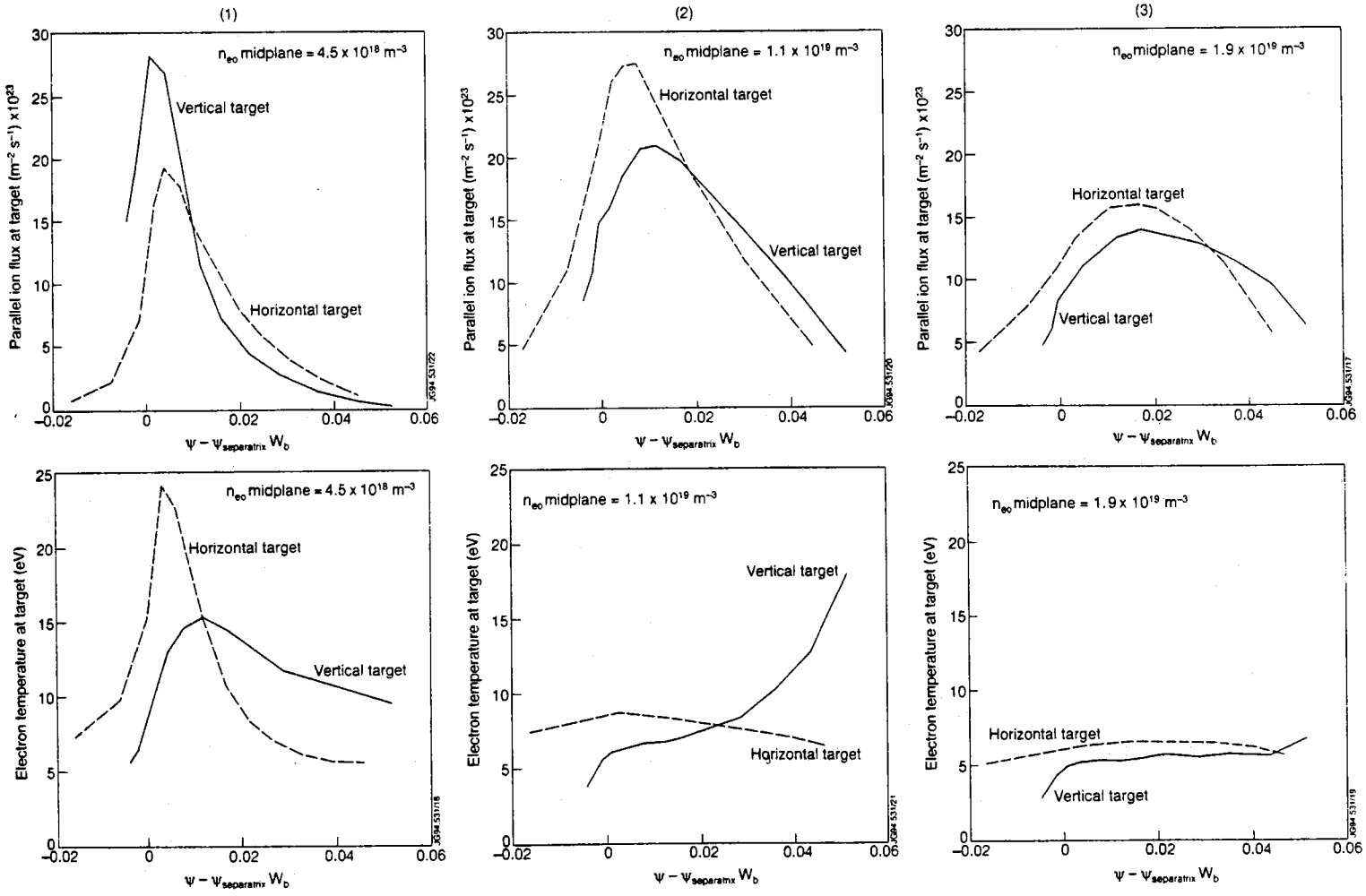

Agreements

- The code shows the ion saturation current to roll over with increasing density for horizontal target case.
- Inverted electron temperature profiles are predicted for vertical target cases.

Disagreements

- At moderate and high density the target temperatures are predicted to be much lower than is measured by the probes.
- The code predicts, for the vertical target configuration, a monotonic decrease in I_{sat} with increasing density over range investigated.
- The code predicts higher ion saturation currents than are measured.

ADDITIONALLY HEATED DISCHARGES

Both configurations have been operated in L and H-mode, but the presence of elms in the H-mode cases and similar fluctuations in the L-mode cases have rendered most of the target profile information unusable for such a simple comparison [2].

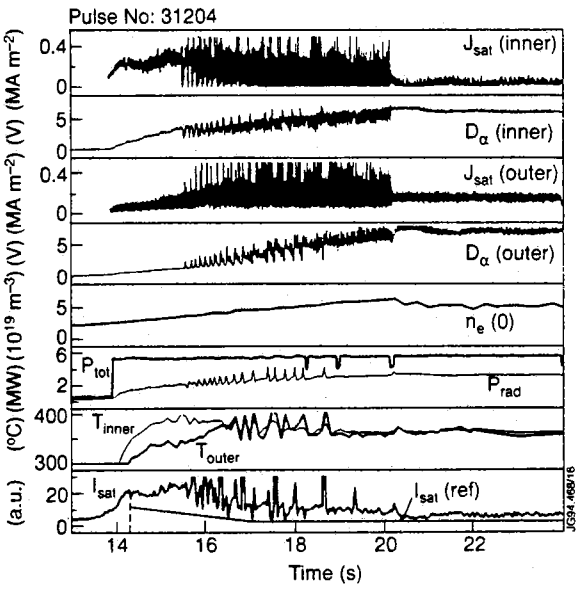

By puffing deuterium into an L-mode discharge one is able to reduce the amplitude of these fluctuations and obtain an ion saturation current less than for a lower density at the same input power, at least at the inner target. By filtering such a signal from a target probe we have been able to feedback the gas flow rate such as to reduce the ion saturation current.

So far we have only managed to drive H-mode discharges in to the L-mode by deuterium puffing, and are now investigating the use of impurities to increase divertor radiation in H-mode discharges.

Radial Profiles

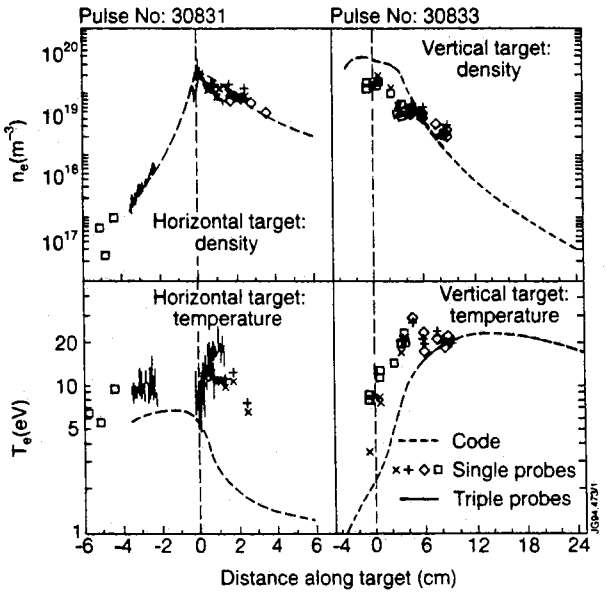

A comparison between measured and modelled target profiles for L-mode discharges in both configurations. In these cases the perpendicular transport coefficients, particle inventory, and radiation terms in the model were adjusted to give the best fit to the experimental data.

- The vertical target case is for 9 MW of Injected power (NBI), and just prior to an L-H mode transition.
- The horizontal target case is for 6.5 MW of injected power (NBI).
- In both cases the profiles are taken about 200 ms after the power switch on, before the typical fluctuations have been established.

CONCLUSIONS

- The global behaviour of discharges on Horizontal and Vertical target plates is similar, especially with respect to detachment. This is not in good agreement with the code.
- The detailed plasma profiles at the target are different in the two configurations, and agree fairly well with the code.

REFERENCES

[1] A.Taroni et. al., Proc. 11th PSI Conf., Mito, Japan, May 1994.
[2] D.J.Campbell and the JET Team, IAEA-CN-60/A-4-1-4.

Divertor Radiation in JET

R Reichle, N A C Gottardi[1], R M Giannella,
H J Jäckel, A C Maas.

JET Joint Undertaking, Abingdon, Oxfordshire, OX14 3EA, UK.
[1] Present address: European Commission, Luxembourg.

Divertor Radiation in JET

R Reichle, N A C Gottardi[1], R M Giannella, H J Jäckel, A C Maas.
JET Joint Undertaking, Abingdon, Oxfordshire, OX14 3EA, UK.
[1] Present address: European Commission, Luxembourg.

INTRODUCTION

With large fusion machines one of the main problems is overheating of the target plates. The most promising technique to overcome this problem is to increase radiation losses in order to reduce the power conducted to the target. Preferably the radiation losses should occur outside the separatrix in the divertor region. To diagnose the effectiveness of this technique JET uses bolometers. First results are reported here.

EXPERIMENTAL DETAILS

Lines of sight

The old JET Bolometer [1] has been modified (fig. 1) and a new system has been added (fig. 2).

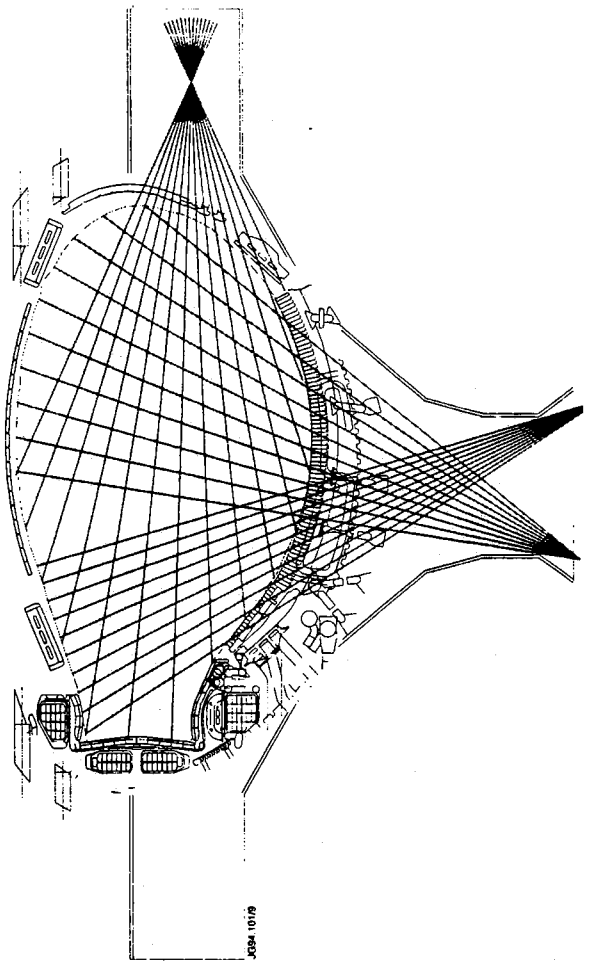

Fig. 1: Lines of sight of the modified old bolometer KB1.

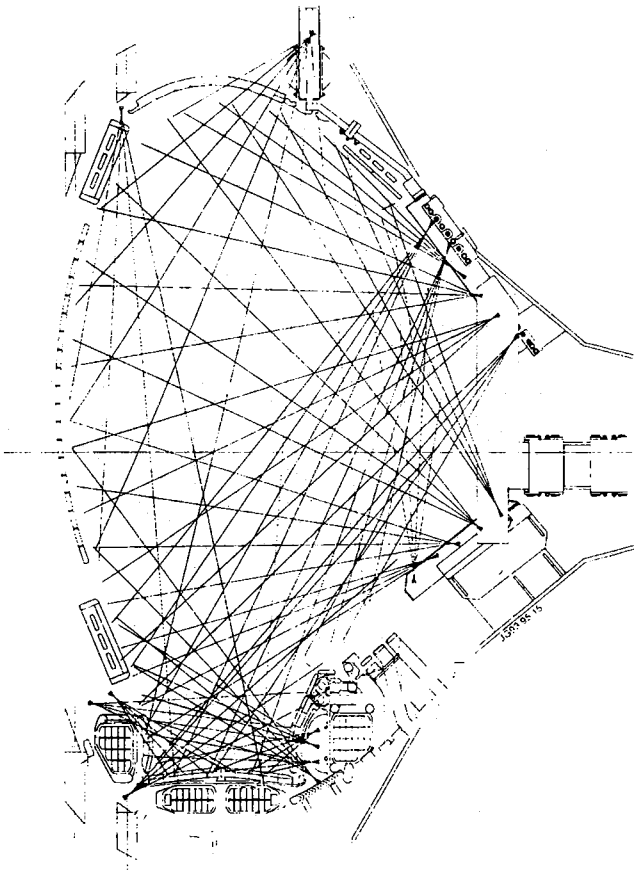

Fig. 2: Lines of sight of the new bolometer KB3D and KB4.

New high temperature detectors

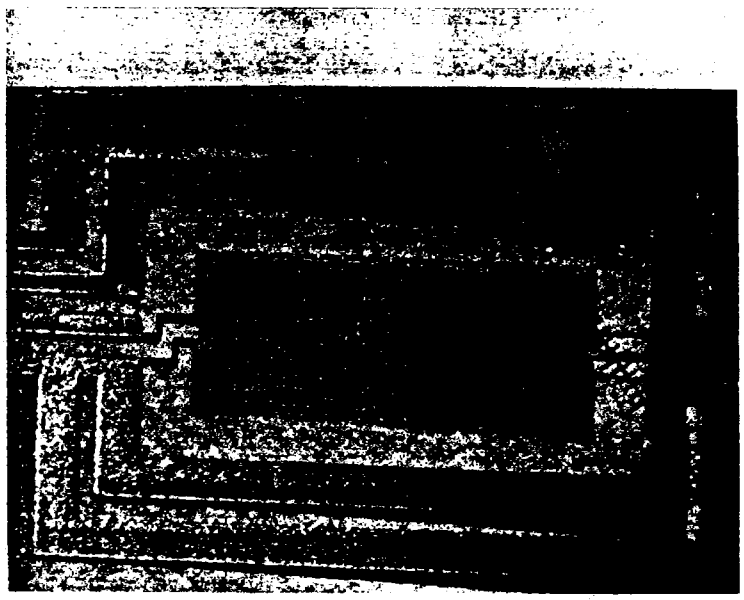

Fig. 3: Detail of the detector foil

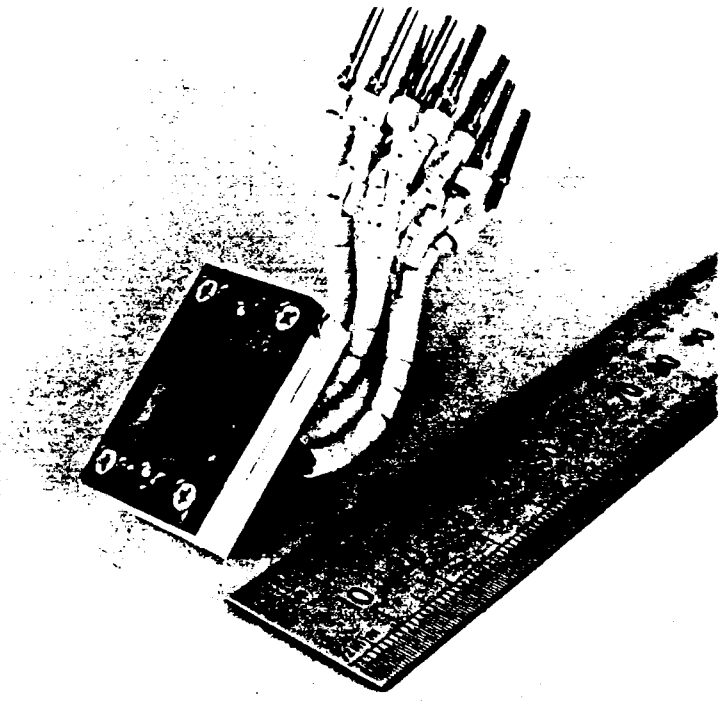

Fig. 4: 4-channel detector in high temperature version

Based on an IPP design [2,3], JET has developed a **high temperature version** of this detector type (fig. 3 and 4).

Detector specifications:

Resistor material:	gold
Thickness:	200 nm
Resistance:	200 Ω ± 50 Ω
Substrate:	mica
Front-plate:	copper
Back-plates:	SHAPAL-M
Wire connections:	Bonding
Blackening:	Aquadag
Annealing temperature:	420°C
Operating temperature:	320°C
Sensitivity:	at 20°C: 1.0 /W
	at 250°C: 0.5 /W

Cables, Shielding and Screening

Two twisted pairs of mineral insulated cables, twisted around each other are used inside the vessel to serve one channel of the detectors. The feed through at the port of the vacuum vessel is used as common ground. The cables and detectors are screened inside an electrically isolated 5 mm thick Inconel steel enclosure

Electronics

Of the new bolometer channels 16 are presently equipped with data acquisition electronics. Synchronous detection at 20 kHz is used to avoid low frequency noise interference.

OBSERVATIONS

Ohmic heated discharge - detachment from vertical target plates

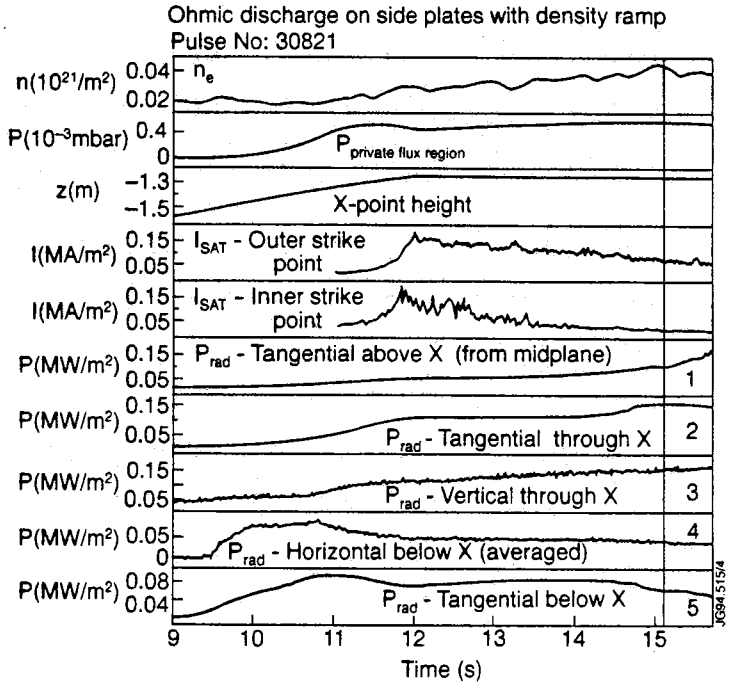

Fig. 5: Overview of discharge 30821.

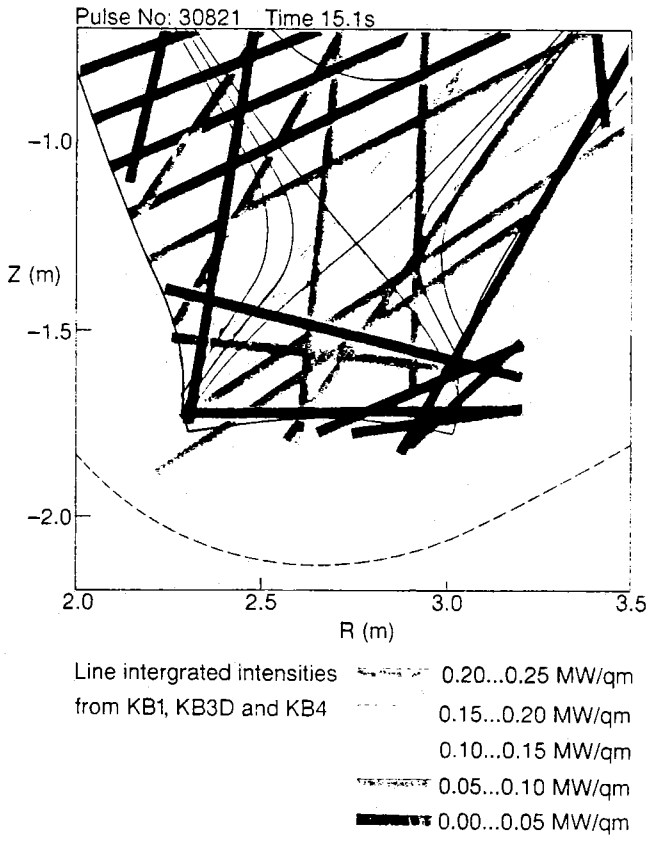

Fig. 6: Line of sight integrated radiation (30821, 15.1 sec).

Discharge 30821 is an example of a discharge **on the vertical target plates** that has a detached radiation pattern.

The radiation has a maximum at the X-point already at the start of the X-point-phase. The intensity of the X-point radiation rises and falls below the X-point falls as the total density and the pressure in the private flux region increase (fig. 5).

The **radiation maximum** at the end of the density ramp is clearly located **around the X-point** (fig. 6 and fig. 7)

Figure 6 gives the measured integrated line intensities at 15.1 sec. in steps of 0.05 MW/m^2, in the sequence blue, green, yellow, orange.

Figure 7 is an emissivity distribution deduced from the line of sight integrals shown in figure 6.

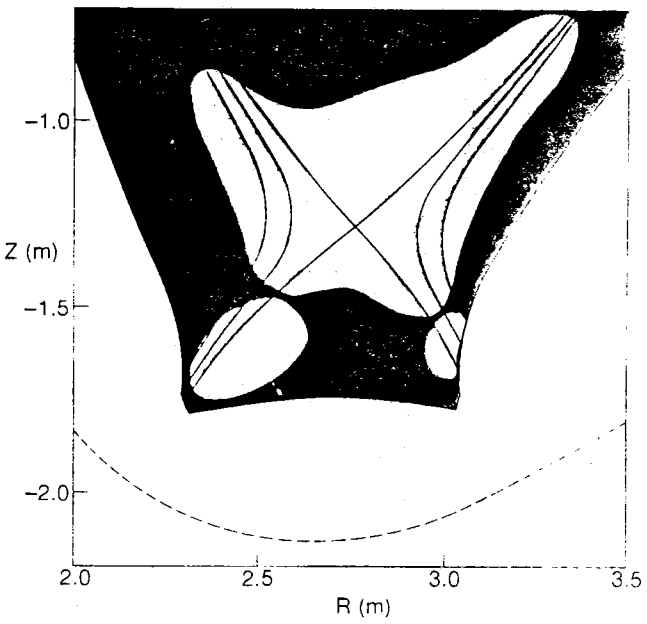

Fig. 7: Deduced emissivity distribution (30821, 15.1 sec).

Ohmic heated discharge - detachment from horizontal target - radiation maximum above the X-point

Discharge 30829 is an example of a discharge sitting **on the horizontal target plates.**

The radiation at the X-point and above the X-point rises while it decays below the X-point as the line integrated density and the pressure in the private flux region go up (fig. 8).

The **radiation maximum** at the end of the density ramp is clearly located **above the X-point** (fig. 9 and fig .10)

Figure 9 gives the measured line intensities at 15.1 sec. in steps of 0.05 MW/m^2, in the sequence blue, green, yellow, orange and red.

Figure 10 is a emissivity distribution deduced from the line of sight integrals shown in figure 9.

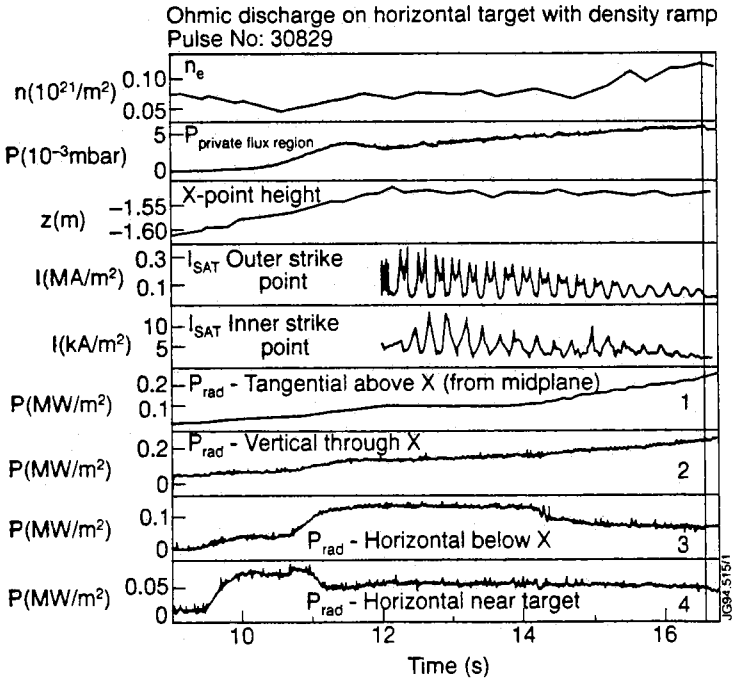

Fig. 8: Overview of discharge 30829.

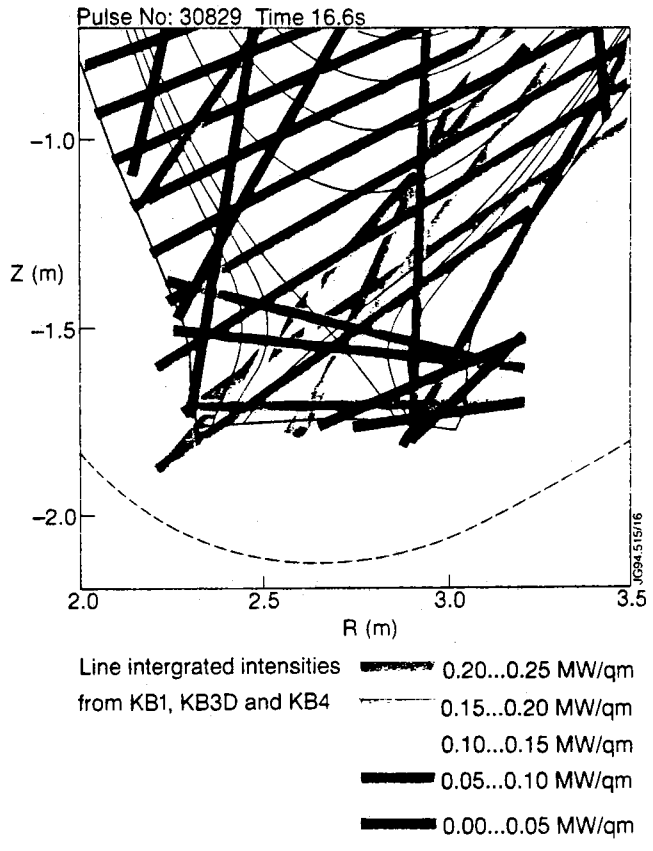

Fig. 9: Line of sight integrated radiation (30829, 16.6 sec).

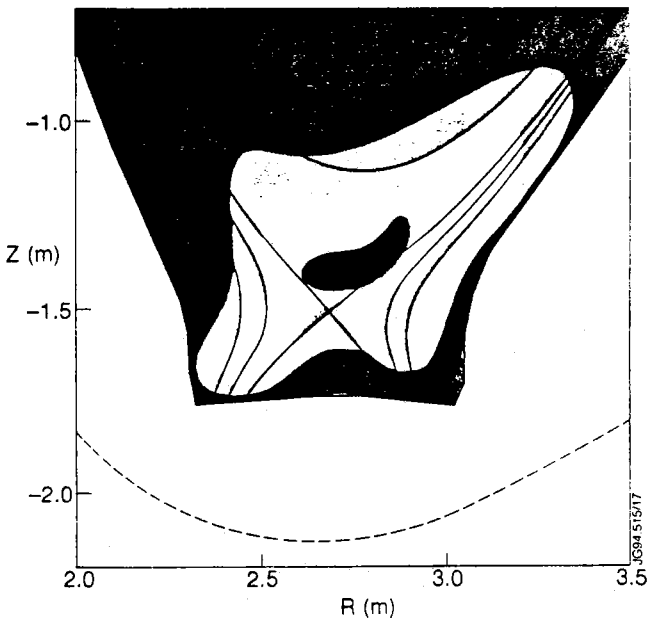

Fig. 10: Deduced emissivity distribution (30829, 16.6 sec).

Detachment with low power additional heating

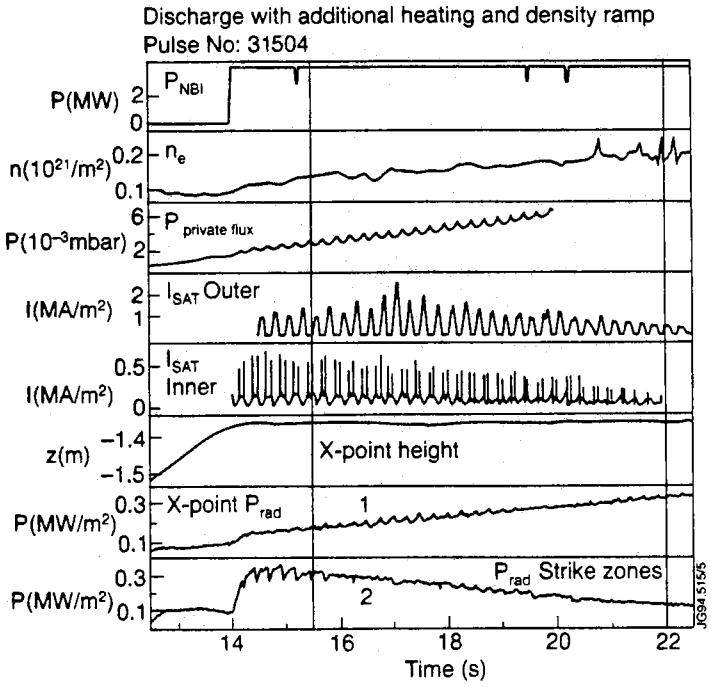

Fig. 11: Overview of discharge 31504.

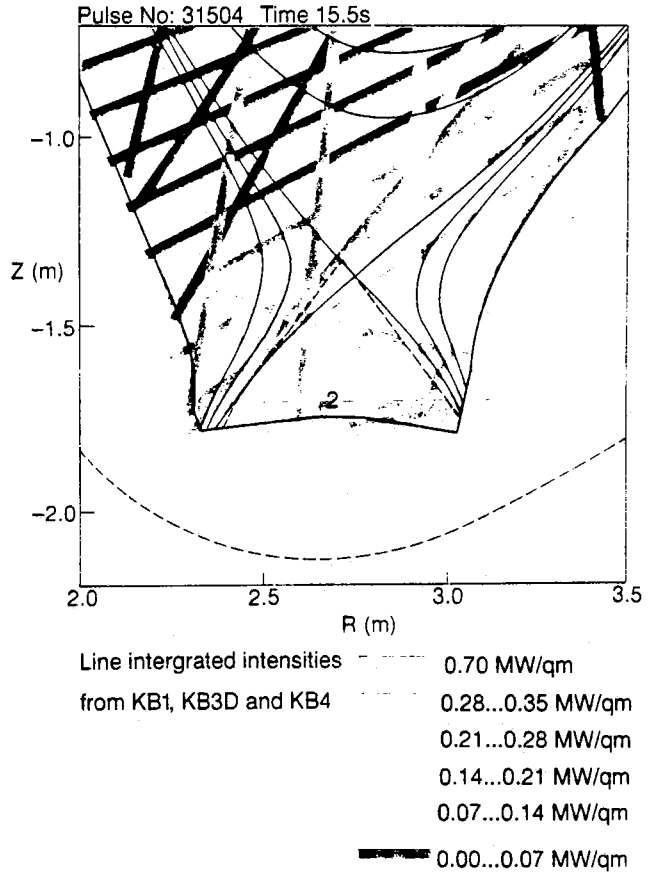

Fig. 12: Line of sight integrated radiation (31504, 15.5 sec).

Discharge 31504 is an example of a discharge with **4 MW heating and a density ramp** up to the density limit. The **radiation at the start** of the additional heating is **high at the strike zones** and low at the X-point. In the course of the density rise this ratio is reversed (fig. 11).

The measured line integrated radiation at the start of the density ramp is shown in figure 12. Magenta indicates 0.7 MW/m^2, the other colours (blue, green, yellow, orange, red) cover 0 to 0.35 MW/ m^2. Note in particular the **high intensity near the inner strike zone.**

Figure 13 shows the deduced emissivity distribution.

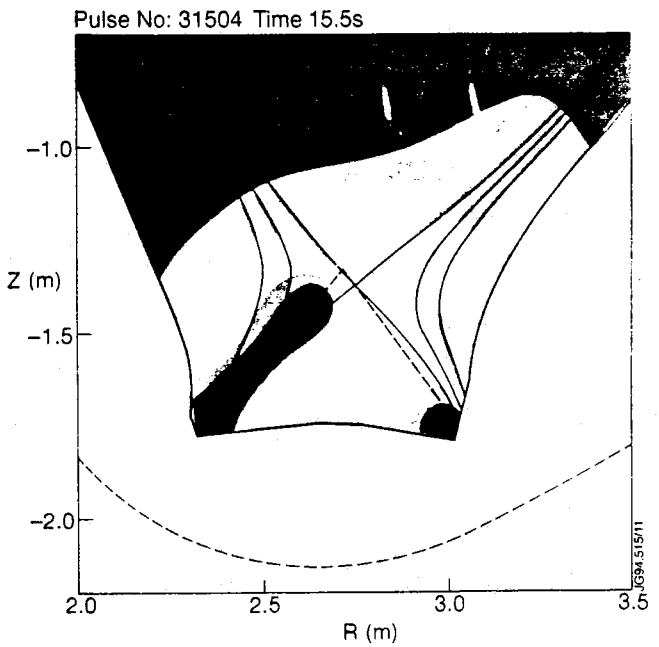

Fig. 13: Deduced emissivity distribution (31504, 15.5 sec).

The line integrated radiation at the **end of the density ramp** is shown in figure 14. Note in particular **high intensity near the X-point.** Figure 15 shows the deduced emissivity distribution.

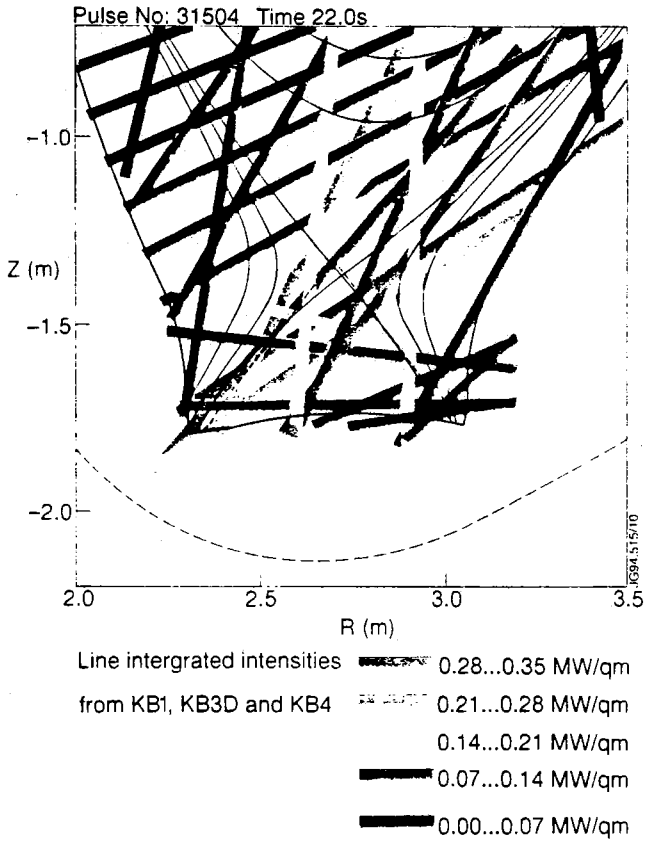

Fig. 14: Line of sight integrated intensities (31504, 22.0 sec)

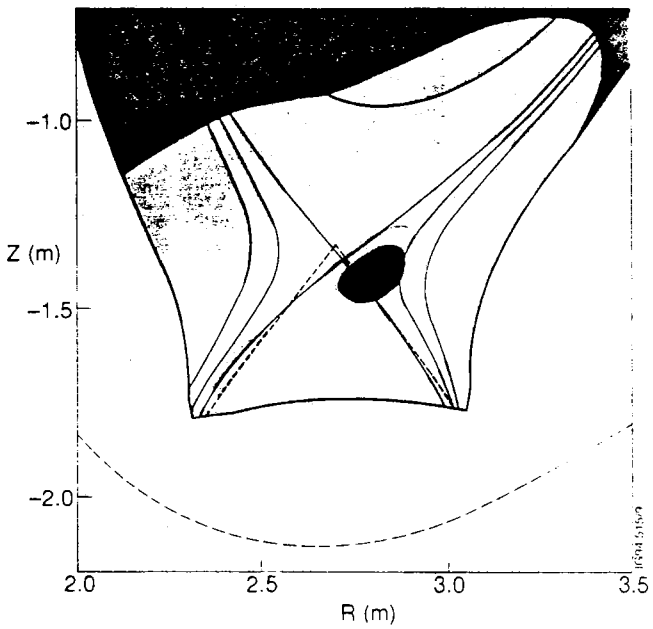

Fig. 15: Deduced emissivity distribution (31504, 22 sec).

Higher power operation - no detachment

Fig. 16 gives an overview of a discharge with 6 MW NBI heating and the strike points on the **horizontal target.**

The **radiation pattern is affected up to the X-point by** the horizontal **sweeping** of the strike zones (fig. 16).

Fig. 17 is the emissivity distribution deduced from line of sight integrals of this discharge.

Fig. 18 is the emissivity distribution in an similar discharge operated on the **vertical target plates.**

In both cases the region where the **radiation** is emitted **extends up the divertor leg** but no detachment has occurred yet.

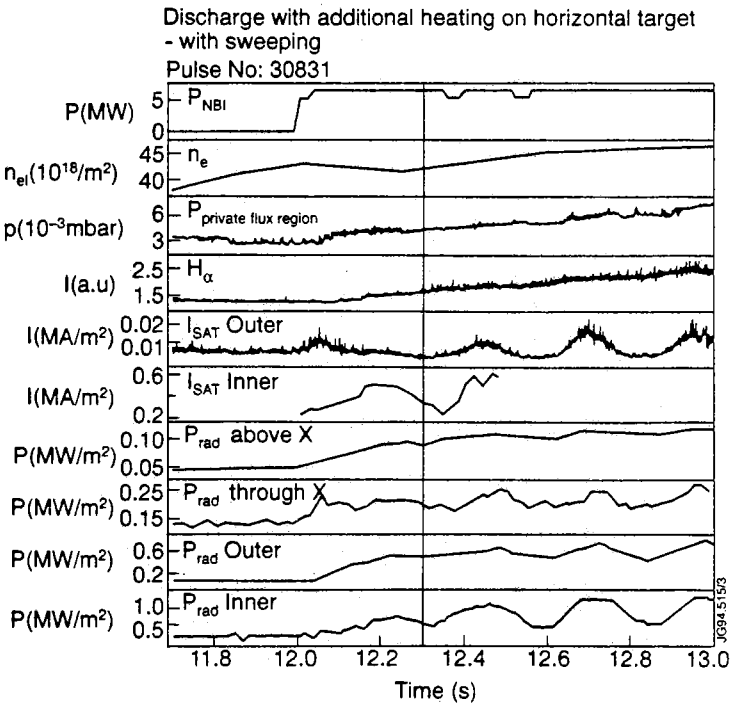

Fig. 16: Discharge with 8 MW additional heating.

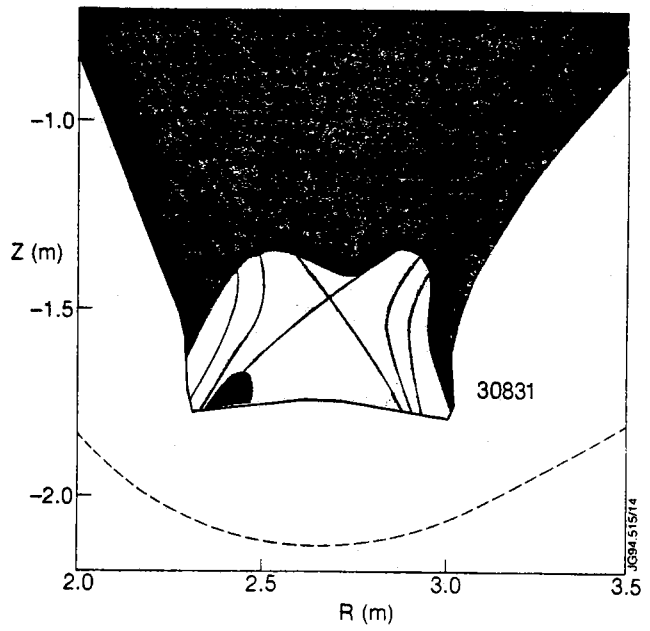

Fig. 17: Radiation distribution - 6 MW NBI - horizontal target

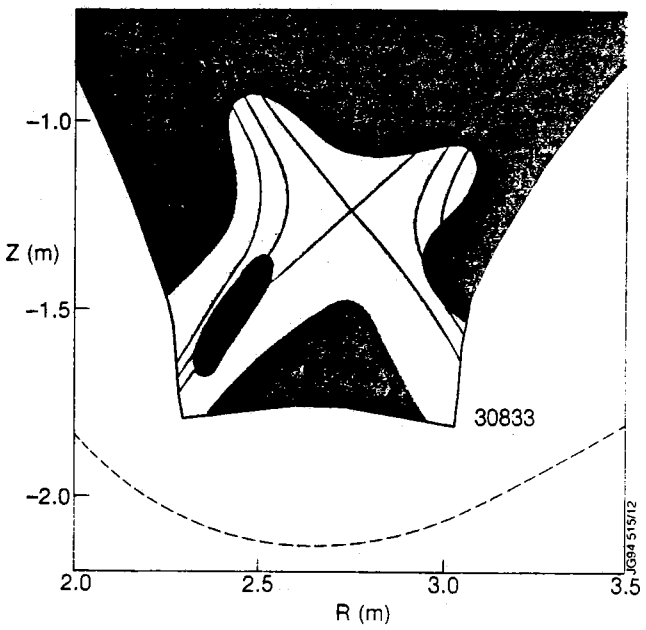

Fig. 18: Radiation distribution - 8 MW NBI - vertical target

High power - H-mode - ELMs

Figure 19 shows a discharge which moves from L-mode (I) into H-mode (II) with giant ELMs (III). The radiation distribution stretches in this process more and more up the divertor leg (fig. 20).

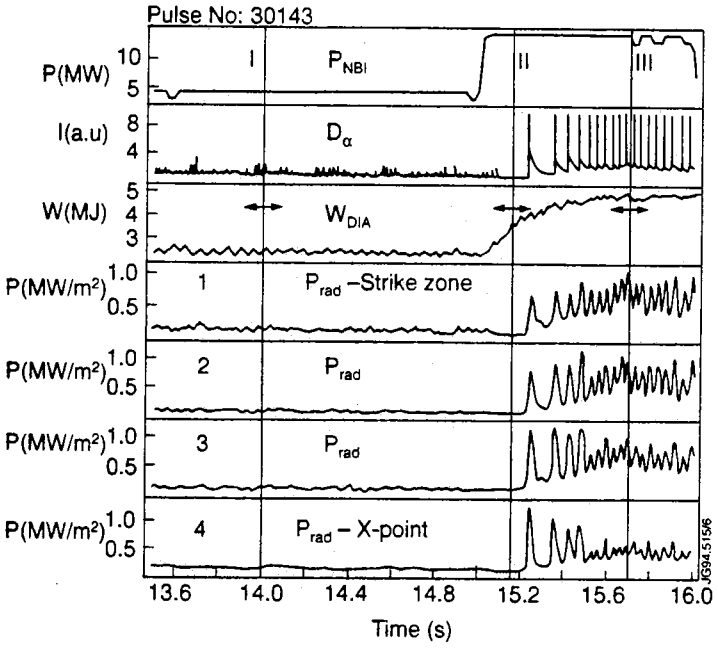

Fig. 19: Discharge with L/H transition and giant ELMs (30150)

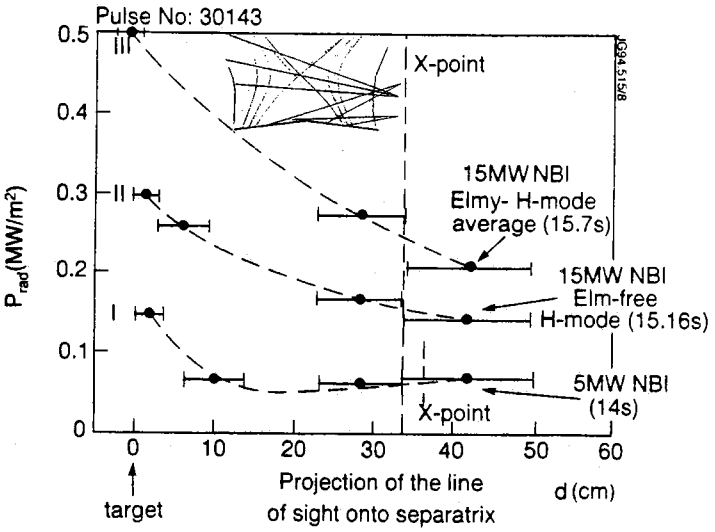

Fig. 20: Divertor leg radiation: I) L -mode, II) H- mode III) giant ELMs

Components of giant ELMs

In giant ELMs it is observed that the radiation pattern has **a fast decaying component** and a **slowly decaying component**. Fig. 21 shows the lines of sights which allow to distinguish the components. Fig. 22 shows that the fast component is coincident with a lateral widening of the radiation pattern in the target region.

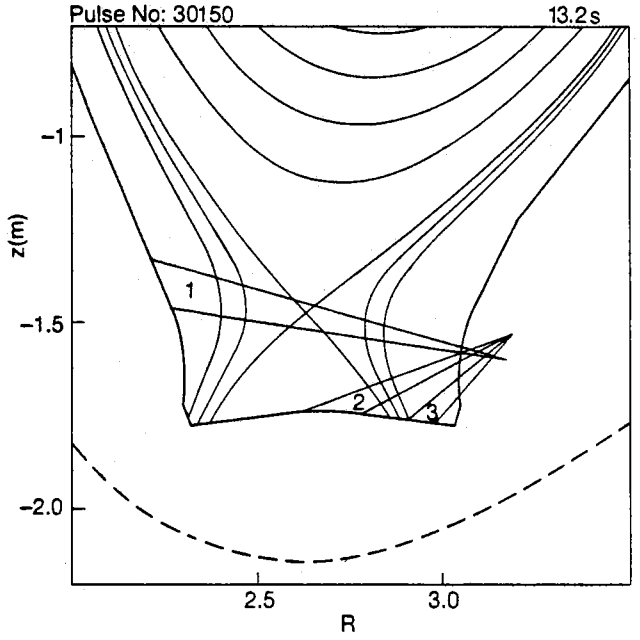

Fig. 21: Lines of sight for fast ELM component study

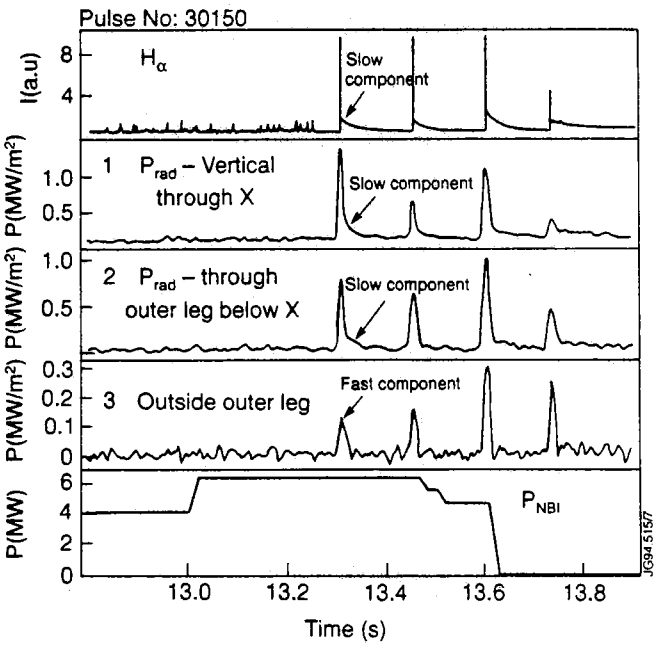

Fig. 22: Temporal evolution of radiation pattern in giant ELMs

SUMMARY

Observed features are:

- Detachment is achieved with high density low power discharges. With rising density the radiation moves up from the strike point to the X-point and in some cases it is seen to move even beyond the X-point inside the separatrix.
- In high power discharges the radiation region extents up the divertor leg.
- Giant ELMs have a fast component of laterally extending radiation at the target apart from the normal slow component.
- Sweeping the strike zones has an effect on the radiation pattern upstream up to the X-point.

ACKNOWLEDGEMENT

We thank S. Dillon and E. McCarron for the design of the new bolometers, R. Wirth of PTS GmbH for the detector development, the Divertor task force for running the detachment discharges, and J de Haas, J. Ehrenberg, R. Monk and M. Stamp for advice on their diagnostics. It is also noted with pleasure that C. Fuchs is presently at JET installing his Anisotropic Diffusion Model Tomography program [4].

REFERENCES

[1] K.F. Mast, H. Krause, Rev. Sci. Instr. 56(5), 1985, p. 969

[2] IPP 1/224 E.R. Müller, G. Weber, K.F. Mast, G. Schramm, E. Buchelt, C. Andelfinger, Max-Planck-Institut für Plasmaphysik, Garching, Oct. 1985

[3] K.F. Mast et al., Rev. Sci. Instr. 62(3), 1991, p. 744

[4] J.C. Fuchs, K.F. Mast, A. Hermann, K. Lackner et al. , Contrib. 21st EPS, Montpellier, France, June 27- July 1, 1994, Poster C107

Parametric Dependencies of JET LIDAR Profiles: Comparison of Ohmic-, L- and H-Modes

B Schunke, K Imre[1], K S Riedel[1].

JET Joint Undertaking, Abingdon, Oxfordshire, OX14 3EA, UK.
[1] New York University, 251 Mercier Street, New York, NY 10012-1185, USA.

Parametric Dependencies of JET LIDAR Profiles: Comparison of Ohmic-, L- and H-Modes

B Schunke, K Imre[1], K S Riedel[1].
JET Joint Undertaking, Abingdon, Oxfordshire, OX14 3EA, UK.
[1] New York University, 251 Mercier Street, New York, NY 10012-1185, USA.

1. INTRODUCTION

A statistical analysis has been performed upon sets of Ohmic, L-Mode and H-Mode electron temperature and density profiles obtained from the LIDAR Thomson Scattering Diagnostic [1] of the JET tokamak. The objective of the analysis was to determine whether the profiles could be represented in terms of the normalised flux parameter ψ and a set of the engineering parameters like plasma current I_p, toroidal field B_T, line averaged electron density $\bar{n}$, inductance ℓ_i, elongation , loop voltage V_{loop} , the edge safety factor q_{95} and z_{eff}. We intend to use the same models to predict the profile shapes for D-T discharges in JET and in ITER.

2. THE LOG-ADDITIVE PROFILE MODELS

Assuming that the electron temperature and density profiles in a tokamak depend only on the global parameters, we adopt generalised log-additive models to describe the profiles [2]. The technique is described in the following for the case of the electron temperature profile. We adopt the ansatz:

$$\ln[\theta(\psi,\bar{u})] = f_o(\psi) + \sum_{l=1}^{L} f_l(\psi) h_l(\bar{u})$$

with θ being the modelled temperature and $h_l(\bar{u}) = \left(\ln[I_p], \ln[B_t], \ln[\bar{n}], \ln[\kappa], \ldots\right)$.

To estimate the unknown coefficients $f_l(\psi)$ we expand in B-splines: $f_l(\psi) = \sum_{k=1}^{K} \alpha_{lk} \beta_k(\psi)$ using cubic spline functions $\beta_k(\psi)$. The control variables $\bar{u}$ are normalised to their mean values in the data set and both the temperature shape and the magnitude are fitted at the same time. All spline coefficients are fitted simultaneously with a penalised least squares regression, choosing λ_l so that

$$\sum_{i,j} \left(\frac{\ln[T_i(\psi_j^i)] - \theta(\psi_j^i, \bar{u}_i)}{\sigma_{i,j}} \right)^2 + \sum_{1} \lambda_l \int_0^1 |f_1(\psi)|^2 d\psi \text{ is minimised.}$$

$T_i(\psi_j')$is the jth radial measurement of the ith measured temperature profile and $\sigma_{i,j}$ is the associated error. The second term is the smoothness penalty function, which damps down artificial oscillations in the estimated $f_1(\psi)$.

We use the Rice criterion to estimate the total error, which consists of variance plus smoothing bias plus the model bias (the error arising from the use of an incorrect model). The Rice criterion differs from a least square fit by the denominator and enables us to compare models and optimise a given model with respect to the smoothing parameter. Adding one parameter at a time during a sequential selection procedure and minimising

$$C_R = \frac{\sum_{i,j}\left(\left(\ln\left[T_i\left(\psi_j^i\right)\right] - \theta\left(\psi_j^i, \bar{u}_i\right)\right)/\sigma_i\right)^2}{(N - 2 \times \textit{degrees of freedom})}$$ then defines a set of dominant variables.

The same fitting process is carried out for the density profiles. Since the line average density is a control variable, we normalise the density profiles to $\bar{n}$.

Advantages of log-additive models:

- Discharge specific phenomena are eliminated by fitting all profiles simultaneously.
- Physics insight into which global variables influence profiles.
- Compact representation for a class of discharges.
- The fitted profiles may easily be input into analysis codes.
- Extrapolation to new values of engineering parameters possible.
- Self consistent errors, including discharge variability, are estimated using repeated measurements.

3. JET ELECTRON DENSITY AND TEMPERATURE PROFILE PARAMETERISATION

We have compiled and, using the fitting method described above, statistically analysed a 43-profile Ohmic data set, a 51-profile L-Mode data set and a 51-profile H-Mode data set. The data were taken from experimental campaigns from 89 to 92. Table 1 shows the parameter ranges of the JET operating space covered.

Table 1	Ohmic	L - Mode	H-Mode
I_p / MA	1.0 - 5.0	1.0 - 4.9	2.1 - 3.2
B_T / T	1.1 -3.4	1.4 - 2.9	1.4 - 29
q_{95}	2.8 - 12.4	3 - 17	3 - 7
P_{RF} / MW	0	0 - 9.7	0 - 9.7
P_{NB} / MW	0	0 - 10.0	0 -12.4

Each profile is measured at 50 locations (every 5 cm) along the mid-plane of the JET vessel. The raw profile data show much radial structure and vary slowly in parameter. We remove the outermost points near the inner wall, where the dumping of the laser light causes a spurious spike on the profile. As the spatial resolution of the diagnostic is about 10 cm, the measurement errors are autocorrelated, and we are able to fit the data with smaller residual errors.

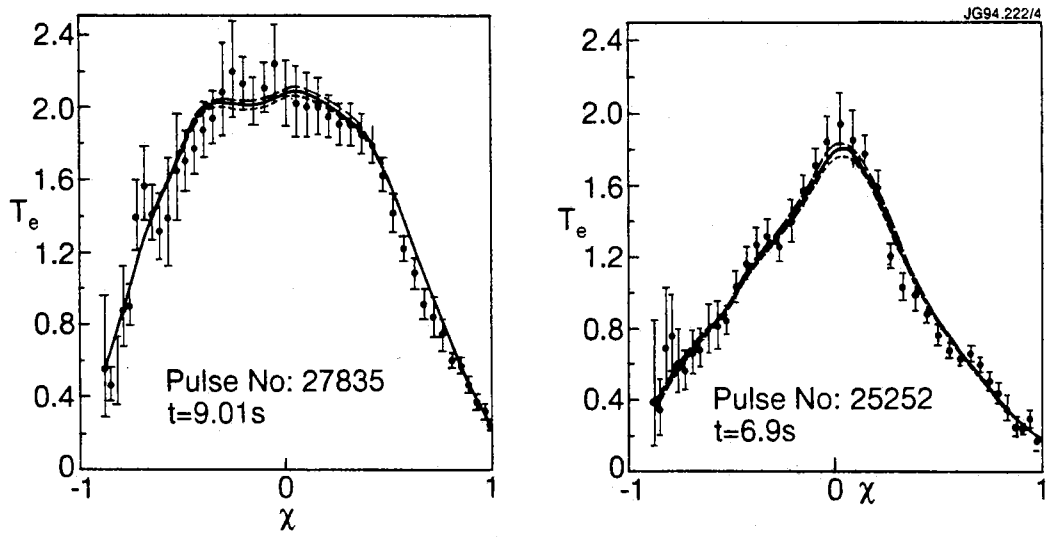

Figure 1: Examples of predicted temperature profile from model with raw data

3A. ANALYSIS OF OHMIC DISCHARGES

Table 2 visualises the selection procedure of the dominant control variables for the Ohmic data set. Fitting all candidates in a one variable fit, one finds that the current I_P minimises C_R. This parameter is then selected and paired with all other variables in a two variable fit. The variable that minimises C_R in combination with I_P is then selected as second parameter, and so on for third and fourth variable.

This sequential selection procedure shows that I_P is the most important variable in determining the plasma temperature, followed by the toroidal field B_T, the line average density $\bar{n}$ and q_{95}. Adding a fifth variable does not appreciably decrease C_R, so we choose the four variable model.

Table 2: *Rice table for Ohmic data set - temperature profiles*

Vars in model	1 Var	2 Var	3 Var	4 Var	5 Var
$\ln[\bar{n}]$	4.64	1.73	**1.12**	seed	seed
$\ln[q_{95}]$	3.04	1.78	1.36	**0.885**	seed
$\ln[I_p]$	**1.93**	seed	seed	seed	seed
$\ln[B_T]$	3.96	**1.58**	seed	seed	seed
$\ln[\kappa]$	4.30	1.94	1.56	1.10	0.875
a	4.60	1.91	1.58	1.11	0.865
R	4.47	1.88	1.58	1.06	0.869
V_{loop}	4.63	1.92	1.53	1.10	0.875
$Z_{eff,1}$	4.01	1.91	1.55	1.06	0.872
$Z_{eff,2}$	4.37	1.79	1.57	1.11	0.85
ℓ_i	4.21	1.63	1.48	1.05	0.875
Time	4.58	1.876	1.52	0.923	0.793

The resulting model for the JET Ohmic temperature profile is:
$\ln[T(\psi)] = f_0(\psi) + f_1(\psi)\ln[I_p / 2.552] + f_B(\psi)\ln[B_T / 2.710] + f_n(\psi)\ln[\bar{n} / 2.1712] + f_q(\psi)\ln[q_{geo} / q]$
with $q_{qgeo} = q_{95} I_p / B_T$ the geometric part of the safety factor q_{95}.

As seen in Figure 2 the electron temperature profile broadens and becomes slightly hollow with increasing current when the other parameters are held constant. The same effect is also seen with decreasing toroidal magnetic field for constant current. Since $f_1(\psi) \neq c - f_B(\psi)$ the profile shape does not depend exclusively on the ratio I_P/B_T. The Rice table shows that the plasma inductance is not particularly influencing the temperature.

Goodness of fit

Our best fit for Ohmic temperature profiles has an average error of 187 eV, which is 12.8 % of the typical line average temperature. The error bar for predicting new measurements is larger than the typical residual fit error. With C_R1.5 the error bar for predictions is 22% larger than the typical measurement error.

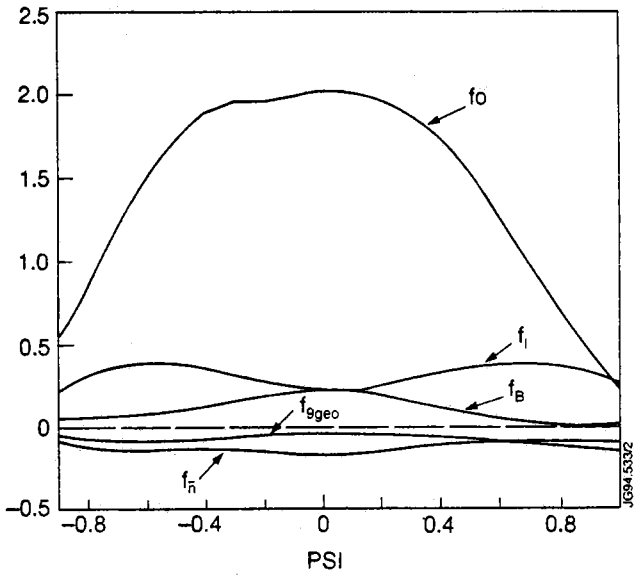

Figure 2: Spline functions for Ohmic electron temperature profiles

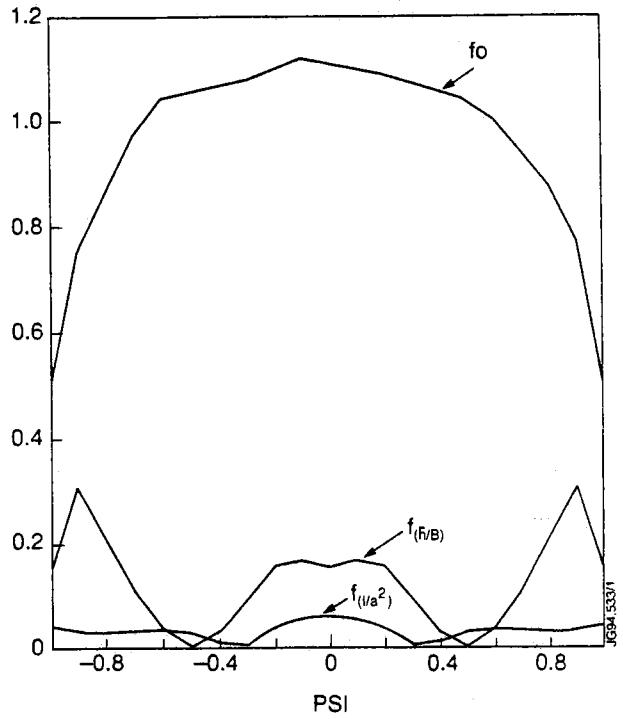

Figure 3: Spline functions for Ohmic electron density profiles

Table 3 presents the model selection criteria for Ohmic density profiles. Compared to the temperature fewer variables are necessary to model the profiles. The normalised Ohmic density profile depends significantly only on a single parameter: $\bar{n}$ / B_T, which strongly resembles the Murakami parameter, and broadens for higher $\bar{n}$ / B_T. The average current density divided by the elongation I/a^2 is the next important variable, but its influence is so minor (Figure 3), that we are inclined to drop it from the final model and instead adopt the simple expression:

$$\ln[n(\psi)/\bar{n}] = f_0(\psi) + f_{n/B}(\psi)\{\ln[\bar{n}/B_t] + 0.2215\}$$

Due to the normalisation of the density profiles, the fit error is 6.65 %, which is greatly reduced compared to the fitting of the temperature profiles. Including I/a^2 in the discription reduces the error to 6.47%.

Table 3 : Rice table for Ohmic data set - density profiles

Vars in model	1 Var	2 Var	1spline 1ct	3 Var
$\ln[\bar{n}]$	1.664	1.460	1.469	1.405
$\ln[q_{95}]$	1.799	1.424	1.472	1.396
$\ln[I_p]$	1.788	1.417	1.472	seed
$\ln[B_T]$	1.877	1.460	1.470	1.405
$\ln[\kappa]$	1.923	1.439	1.473	1.404
$B / \bar{n} R$	1.841	1.424	1.470	1.392
$q_{95} I_{95}/B$	1.878	1.444	1.471	1.387
V_{loop}	1.884	1.432	1.465	1.375
$Z_{eff,}$	1.816	1.362	1.469	1.332
I / a^2	1.775	**1.413**	1.472	1.394
l_i	1.774	1.445	1.472	1.407
Time	1.906	1.437	1.437	1.379
$\bar{n}$ / B	**1.470**	seed	seed	seed

3B. ANALYSIS OF L- AND H-MODE DISCHARGES

We use similar log-additive model for L- and H-mode discharges, fitting unnormalised temperature and normalised density profiles. In each case, we determined the selection of control variables by minimising the Rice criterion. In particular we find

in the case of L-Mode profiles:

The dominating parameter is the heating power P_{aux} , followed by the magnetic field B_t and again the line average density.

Best fit model:

$$\ln[T(\psi)] = f_0(\psi) + f_B(\psi)\{\ln[B_t] - 0.9447\} + 0.3\{\ln[P_{aux}] - 1.3504\} - 0.4\{\ln[\bar{n}] - 0.7809\}$$

As in the case of the Ohmic discharges, the line average density is also the most important parameter for L-mode. The profiles flatten with increasing line density. We also observe a weak dependency on the elongation, (Figure 4), which is surprising as the parameter varies relatively little in the dataset. It influences mainly the edge region of the profile where the density profile decreases rapidly at higher elongations. The resulting model is:

$$\ln[n(\psi)/\bar{n}] = f_0(\psi) + f_n(\psi)\{\ln[\bar{n}] + 1.0784\} + f_\kappa(\psi)\{\ln[\kappa] - 0.51017\}$$

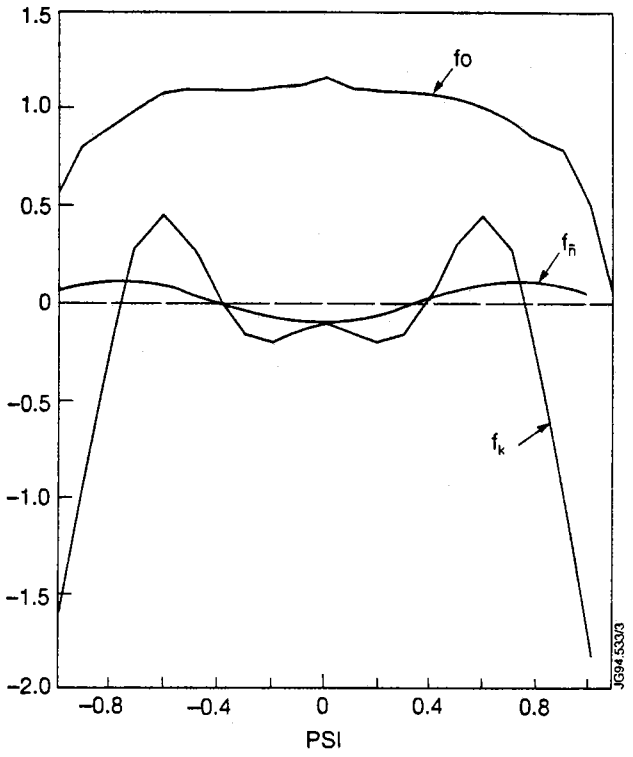

Figure 3: Spline functions for L-Mode electron density profiles

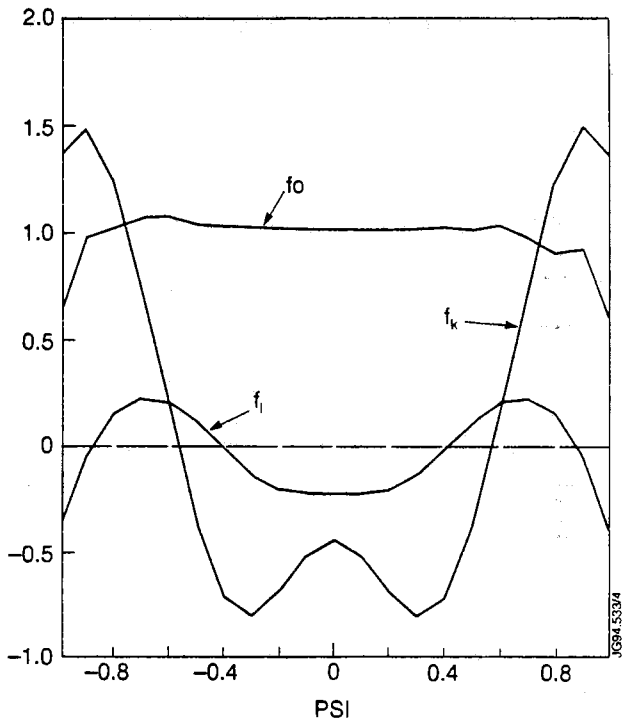

Figure 4: Spline functions for H-Mode electron density profiles

in the case of H-Mode profiles:

The H-mode temperature shape depends primarily on I_P as in the Ohmic case' followed by Z_{eff} and the additional heating power P_{aux} and q_{95}:

Best fit model:

$$\ln[T] = f_0(\psi) + 2.234\ \ln\{[I_p] - 0.9775\} + 0.1556\{Z_{eff} - 0.2633\} + 0.118$$
$$\{\ln[P_{aux}] - 0.1960\} + f_q(\psi)\{\ln[q_{95}] - 0.1619\}$$

The current I_p is the most important control variable for the normalised H-mode density, followed by the elongation . Increasing Ip results in less peaked, sometimes hollow profiles. Increasing extends

the flat regions of the profile, resulting in sharper gradients in the edge region. The range of variation of is small (14.5% for H-mode) in the dataset and the effect might be weaker in a larger sample size.
Best fit model:

$$\ln[n(\psi)] = f_0(\psi) + f_1(\psi)\{\ln[I_p] + 0.9775\} + f_\kappa(\psi)\{\ln[\kappa] - \}$$

4. FUTURE WORK

Extension of JET profile data base to further clarify parametric dependencies. Especially include and compare to profiles from new divertor configuration.
Multimachine database for extrapolation to ITER performance possible.
Testing of alternative log-additive diffusivity model for plasma profiles, with the temperature profile shape resulting from a radial distribution of sinks and sources.

Hierarchy of models

Profile resilience and diffusivity profile resilience strongly suggest that the appropriate empirical models for local profile dependencies are the additive log-temperature model and the additive log-diffusivity model. We therefore distinguish four classes of empirical transport models:

1) Global confinement models: τ_E = f (engineering variables)
2) Semiparametric profile models: T = f (ψ,engineering variables)
3) Semiparametric diffusivity models: χ = f (ψ,engineering variables)
4) First principal transport models: T = f (physics variables), possibly given by theoretical expressions.

5. REFERENCES:

[1] H.Salzmann, J.Bundgaard, A.Gadd, et.al., Rev.Sci.Instrum.**59**, 1451(1988)
[2] McCarthy, P.J., Riedel, K.S., Kardaun, O.J.W.F., Murmann, H., Lackner, K., Nuclear Fusion, **31**, 1595 (1991)

Fast Particle Losses due to Toroidal Alfvén Modes in JET

S Sharapov, L C Appel[1], D Borba, T C Hender[1],
G T A Huysmans, W Kerner, S D Pinches[2].

JET Joint Undertaking, Abingdon, Oxfordshire, OX14 3EA, UK.
[1] UKAEA Government Division, Fusion, Culham Laboratory, Abingdon, Oxfordshire, OX11 3DB, UK.
[2] University of Nottingham, Nottingham, UK.

Fast Particle Losses due to Toroidal Alfvén Modes in JET

S Sharapov, L C Appel[1], D Borba, T C Hender[1], G T A Huysmans, W Kerner, S D Pinches[2].

JET Joint Undertaking, Abingdon, Oxfordshire, OX14 3EA, UK.

[1] UKAEA Government Division, Fusion, CUlham Laboratory, Abingdon, Oxfordshire, OX14 3DB, UK.

[2] University of Nottingham, Nottingham, UK.

INTRODUCTION

- Toroidal Alfven Eigenmodes (TAEs) can be destabilized in JET by resonant interaction with high energy particles (e.g. α-particles, neutral beam particles, RF-heated ions).

- Resonant interaction leads to exchange of momentum and energy between particles and wave, which can cause:
  - * 'anomalous' losses of fast particles due to TAEs [1, 2],
  - * radial redistribution of fast particles and the plasma heating profiles.

- In hot ion JET discharges a spectrum of Kinetic TAE-modes [3] (KTAEs) can appear and be driven unstable, so fast particle particle transport due to KTAEs also has to be taken into account.

- An analysis of fast particle losses in the presence of finite-amplitude TAEs and KTAEs in JET (which are supposed to be driven unstable) is the aim of the present work.

TWO CODES ARE USED IN THIS ANALYSIS

- TAE-spectra and mode structure of TAEs are calculated by the toroidal linear spectral code CASTOR [4] (resistive MHD code for general geometry and finite-pressure plasma equilibrium). KTAE-spectra are calculated by CASTOR in the "complex resistivity" approximation [5].

- CASTOR eigenfunctions together with associated equilibrium provide the electromagnetic field input for a new guiding centre particle following code HAGIS [6].

JET TAE SPECTRA

- α-particle driven TAEs were analysed in a high-performance Deuterium JET discharge (#26087), assuming $n_D = n_T$.
- It was found that a modest decrease in density would destabilise TAEs, with the most likely candidates for TAE instability n = 3 modes.
- Three n = 3 TAE modes have been recognized for JET equilibrium.

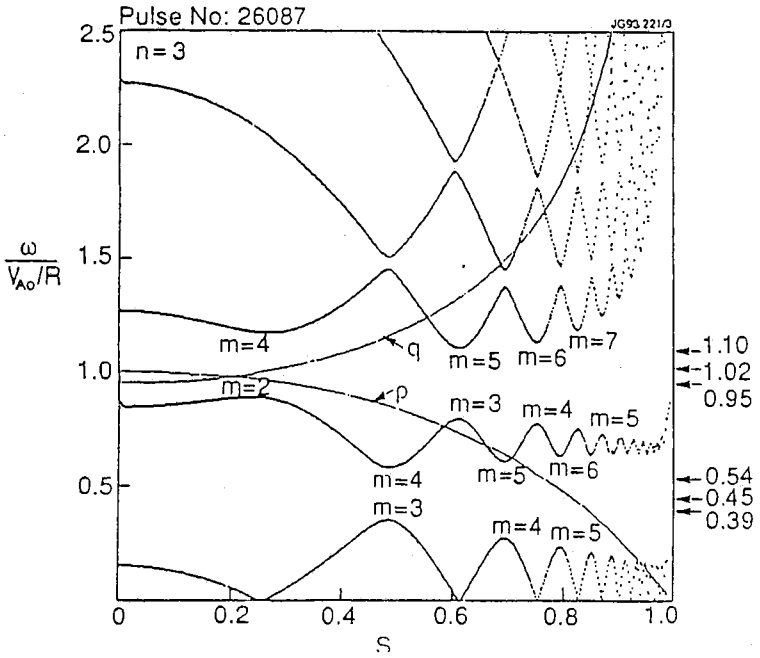

Fig. 1 Ideal MHD Spectrum for n = 3, $s = \psi^{1/2}$

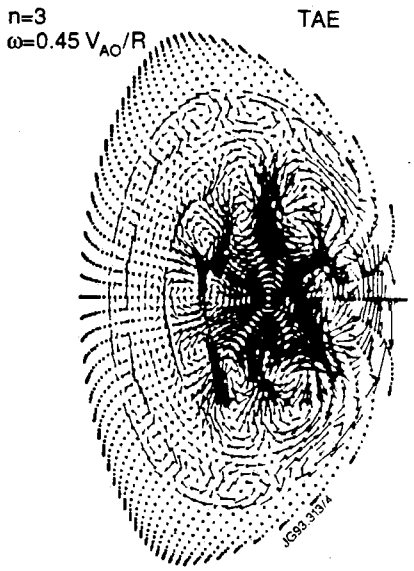

Fig. 2 n = 3 TAE eigenfunction

COMPLEX RESISTIVITY APPROXIMATION FOR KTAE IN CASTOR CODE

- In hot-ion JET plasmas non-ideal effects due to Finite Larmor Radius of core ions become important to give the following corrections to the vorticity equation.

$$\underbrace{(\vec{b}\nabla)\left(\nabla_\perp^2(\vec{b}\nabla)\phi\right)+\nabla\left(\frac{\omega^2}{v_A^2}\nabla_\perp\phi\right)}_{\text{Ideal MHD Part}}+\underbrace{\frac{3}{4}\frac{\omega^2}{v_A^2}\rho_i^2\nabla_\perp^4\phi}_{\text{FLR}}+\underbrace{(1-i\delta(\nu_e))\frac{\omega^2}{v_A^2}\rho_s^2\nabla_\perp^4\phi}_{E_\parallel\neq 0\ \text{Term}}=0$$

- In resistive MHD, analysed by CASTOR for $|\eta k_r^2/\omega| << 1$, the vorticity equation has a form

$$\underbrace{(\vec{b}\nabla)\left(\nabla_\perp^2(\vec{b}\nabla)\phi\right)+\nabla\left(\frac{\omega^2}{v_A^2}\nabla_\perp\phi\right)}_{\text{Ideal MHD Part}}+\underbrace{(\vec{b}\nabla)\left(\frac{i\eta}{4\pi\omega}\nabla_\perp^4(\vec{b}\nabla)\phi\right)}_{\text{Small resistivity}}=0$$

- In resistive term we put for KTAE $(\vec{b}\nabla)\approx\frac{i}{2qR}$ and introduce a "complex resistivity"

$$\eta=4\pi\omega\rho_s^2\delta(\nu_e)+4\pi i\omega\left(\frac{3}{4}+\frac{T_e}{T_i}\right)\rho_s^2\,.$$

This allows to analyse Kinetic TAE-spectrum with the aid of CASTOR.

JET KTAE SPECTRA

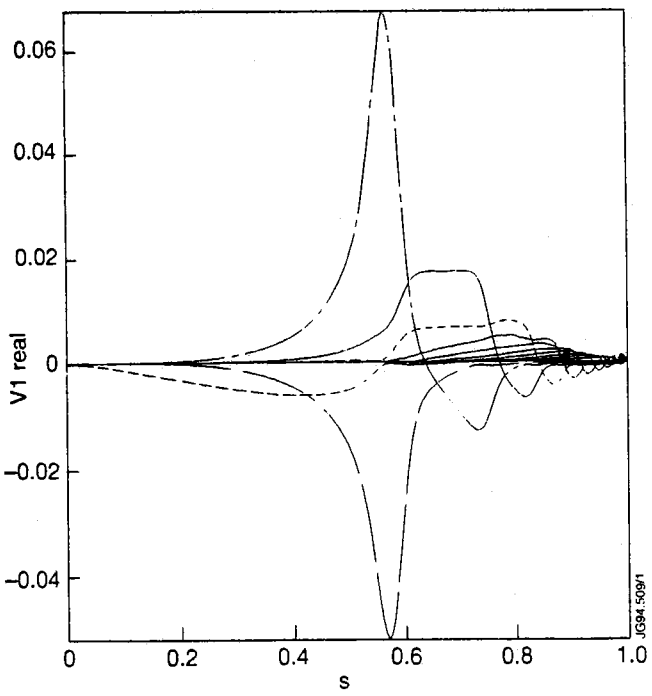

a) p = 0; ω/ω_A = 0.6768; γ/ω - 0.16%;

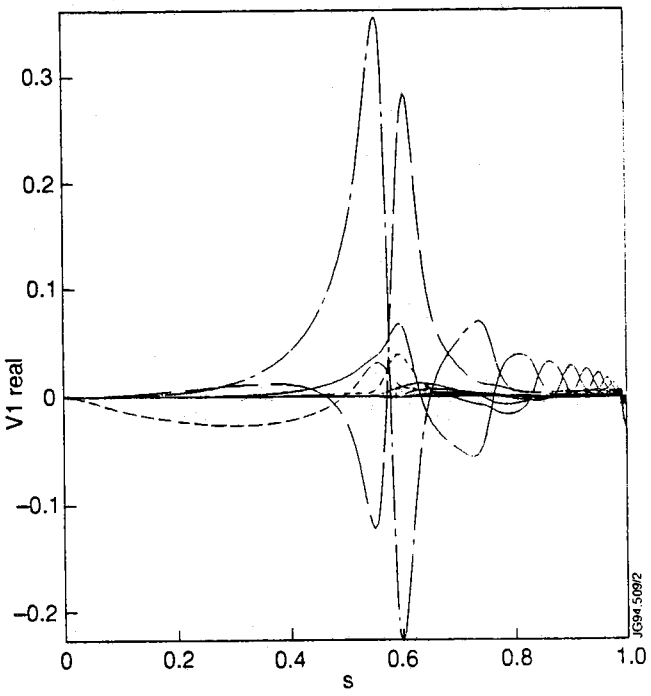

b) p = 1; ω/ω_A = 0.6901; γ/ω - 0.275%;

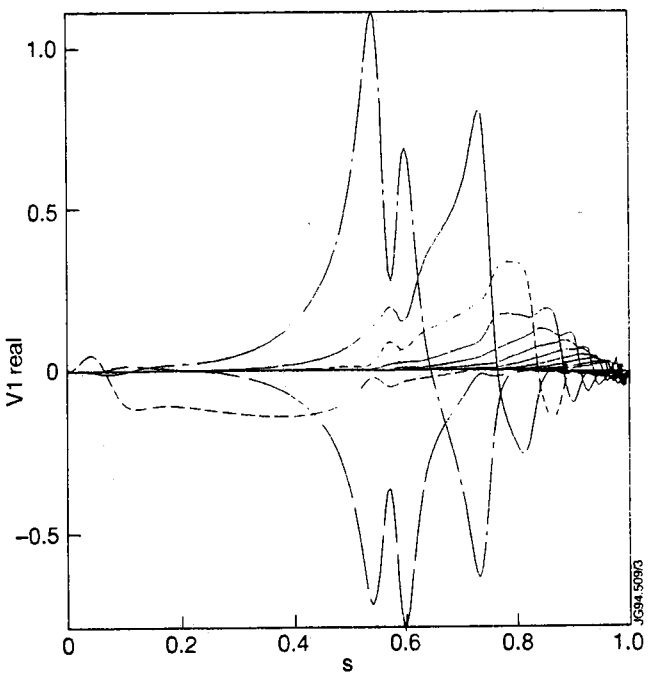

c) p = 2; ω/ω_A = 0.7170; γ/ω - 0.36%;

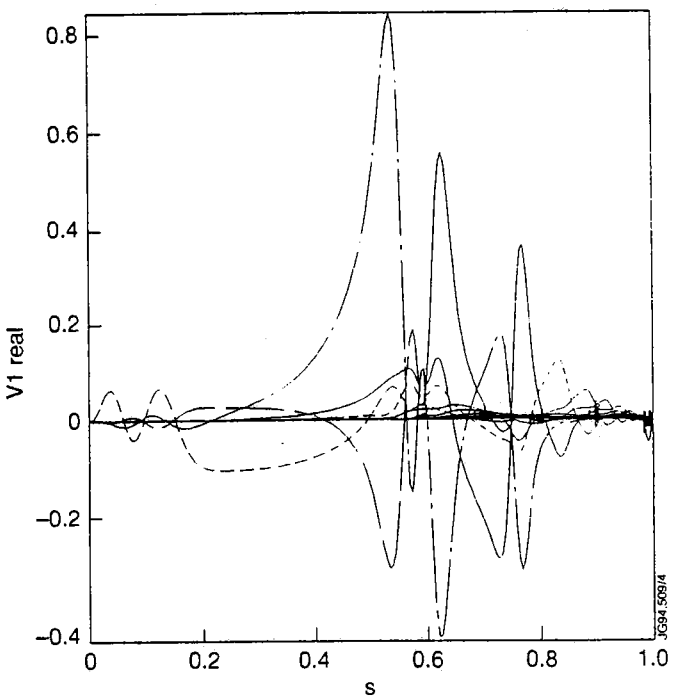

d) p = 3; ω/ω_A = 0.7365; γ/ω - 1.26%;

$\omega_A \equiv v_A(o) / R$.

Fig. 3 Kinetic TAE modes (n = 3) in JET: p is the quantum number of KTAE eigenvalue.

GUIDING CENTRE CODE HAGIS

(Hamiltonian Guiding Centre System)

Code follows particles within a plasma with general magnetic field under the influence of time-dependent electromagnetic perturbations.

- This code is based on a Hamiltonian formalism to enhance numerical accuracy.
- Without TAE perturbations for worst case (Pinch orbit) invariants of particle energy E and toroidal angular momentum P_φ conserved typically $0(10^{-10})$ over a poloidal transit.
- With TAE perturbation, the invariant $E-\omega P_\varphi/n$ is conserved $0(10^{-6})$ per transit.

FAST PARTICLE LOSS MECHANISIMS

- As in Ref. [1] two mechanisms for fast particle loss due to TAEs have been identified for JET cases studied:
- TAE-induced prompt losses near loss boundaries. These losses scale linearly with the applied TAE perturbation.
- Stochastic radial diffusion of fast particles occurs in the presence of finite-amplitude TAE when the particle excursions due to the primary and side-band TAE resonances overlap. For several excited TAEs global stochastic diffusion into loss cones may occur.

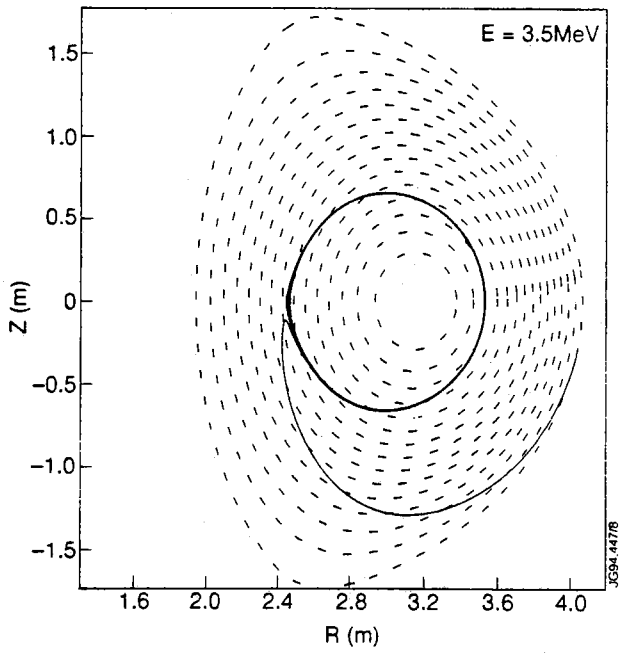

Fig. 4 Conversion of a barely passing particle into lost banana.

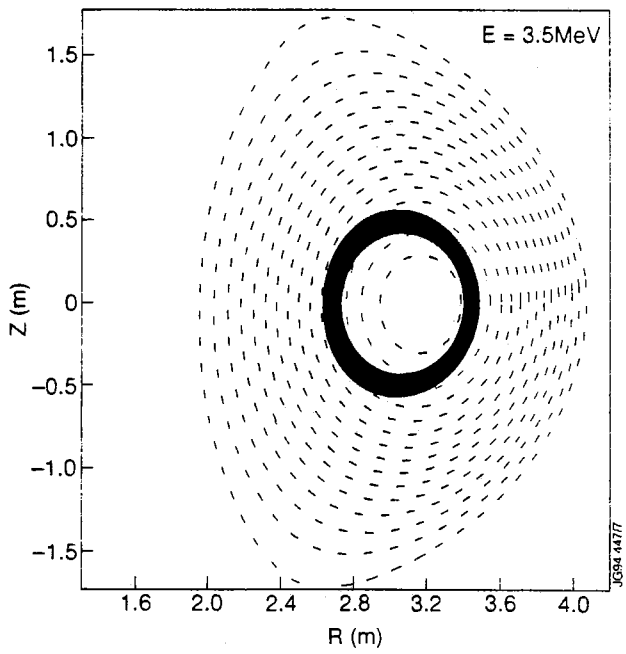

Fig. 5 Stochastic diffusion due to single n = 3 TAE.

TRANSITION FROM REGULAR TO STOCHASTIC PARTICLE MOTION DUE TO TAE

- For a single TAE mode the stochasticity threshold was analysed by examining the particle islands in a frame of reference which moves at the TAE frequency (i.e. $\zeta - \omega t/n$).
- Fairly high stochasticity threshold $\delta B_r / B \approx 3 \times 10^{-3}$ was found to be typical for single n = 3 mode, localised in the low shear region.

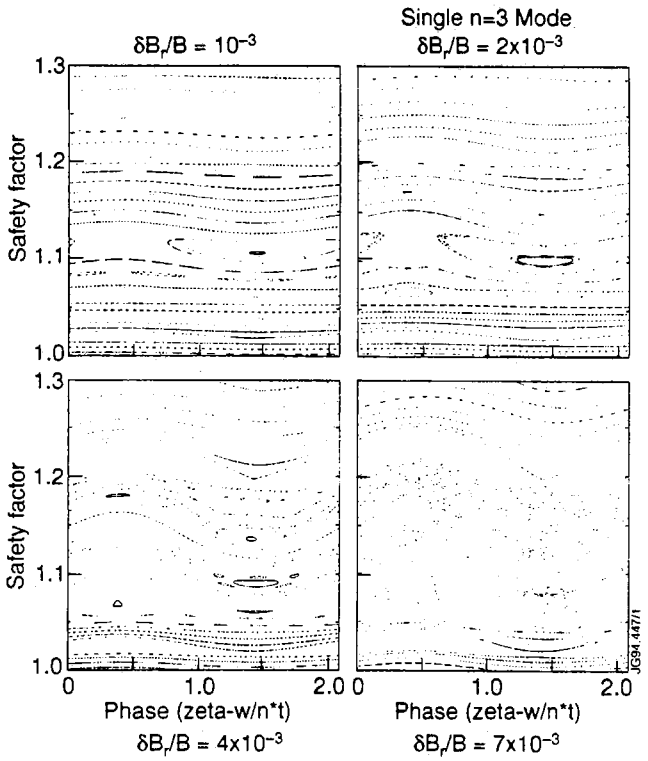

Fig. 6 Particle islands in the q = 0 plane plotted versus the phase (ζ–$\omega t/n$). The total (i.e. all poloidal harmonics) $\delta B_r/B_0$ values are: (a) 10^{-3}, (b) 2×10^{-3}, (c) 4×10^{-3} and (d) 7×10^{-3}.

- For multiple n = 3 TAE pertubations (of different frequency) the stochasticity threshold was found to be $\delta B_r / B \sim 10^{-3}$.

FAST PARTICLE LOSSES DUE TO TAE

- To study particle losses Monte-Carlo simulations of 50,000 α-particles have been made.
- α-particles have a slowing down distribution with 1.5 MeV $\leq E \leq$ 3.5 MeV, a radial distribution α $(1-\Psi)^3$ and a random distribution in pitch angle, poloidal angle and toroidal angle.

- Three n = 3 TAE modes (ω/ω_A = 0.41, 0.51 and 0.58) have been used.

- These Monte-Carlo simulations show two distinct classes of lost α-particles with different time scales:
  * TAE-induced prompt losses (in ~20 μs) of particles born near a loss boundary.
  * Above a global stochasticity threshold continued long term loss of α-particles by stochastic diffusion into a loss boundary.

- Lost fast particle flux has a maximum at the outboard mid-plane, due to co-directed trapped and passing particle orbits intercepting the 'wall'.

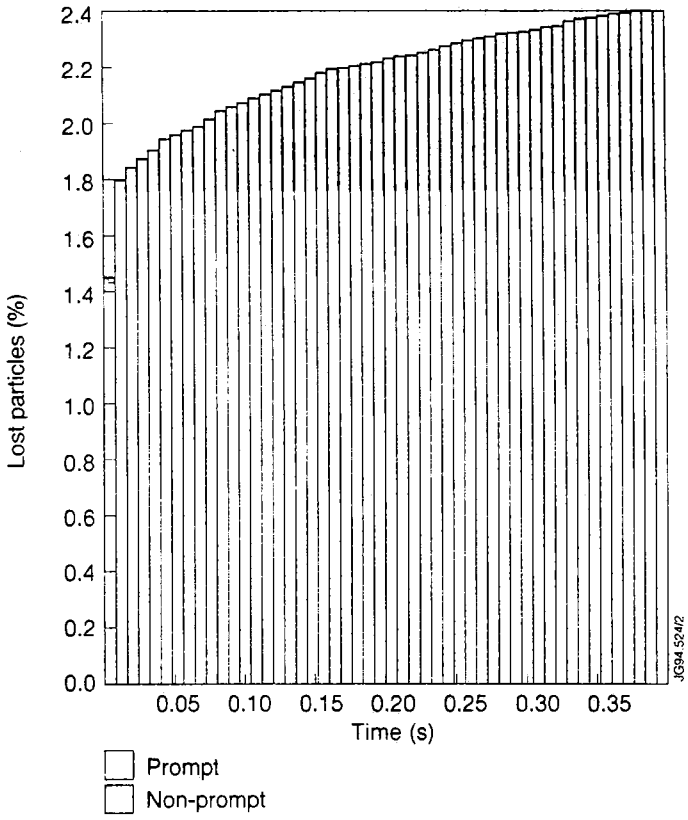

Fig. 7 Total number of lost particles versus time for $\delta B_r/B = 3\times10^{-3}$.

STOCHASTIC DIFFUSION DUE TO KTAE

- TAE- and Kinetic TAE-modes have different poloidal localization and eigenfrequency spectrum, so that fast particle transport due finite amplitude KTAEs has to be studied separately from TAE.

- A particle diffusion coefficient due to n = 3 KTAE-spectrum (p = 0, ..., 3-modes) and n = 3 TAE-spectrum was measured as a particle distribution spread $\langle \Delta P_\varphi^2 \rangle = \langle P_\varphi^2 \rangle - \langle P_\varphi \rangle^2$ in time ($\langle\ \rangle$ = ensemble average).

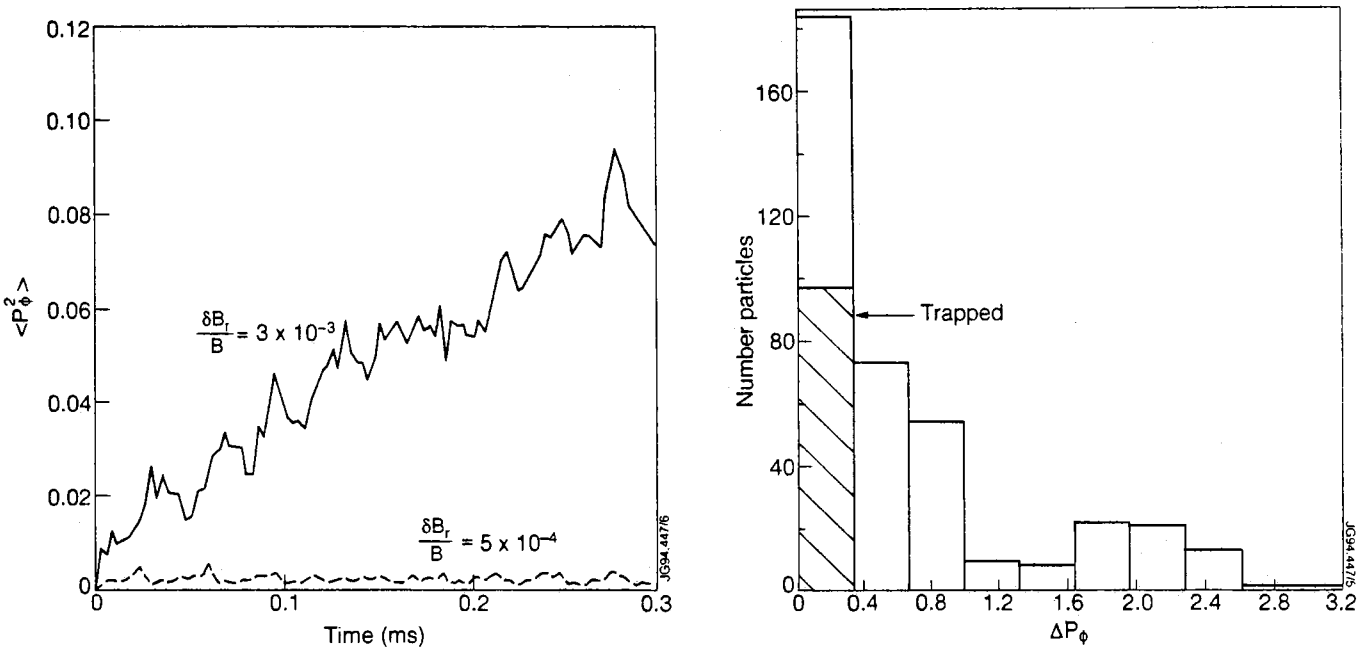

Fig. 8 (a) Variation of $\langle \Delta P_\varphi^2 \rangle \times 10^{40}$ with time for $\delta B_r/B = 3 \times 10^{-3}$ and 5×10^{-4} for TAE-case.
(b) Number of particles with given $\Delta P_\phi \times 10^{20}$ for $\Delta B_r/B = 3 \times 10^{-3}$, the shaded bars are trapped particles

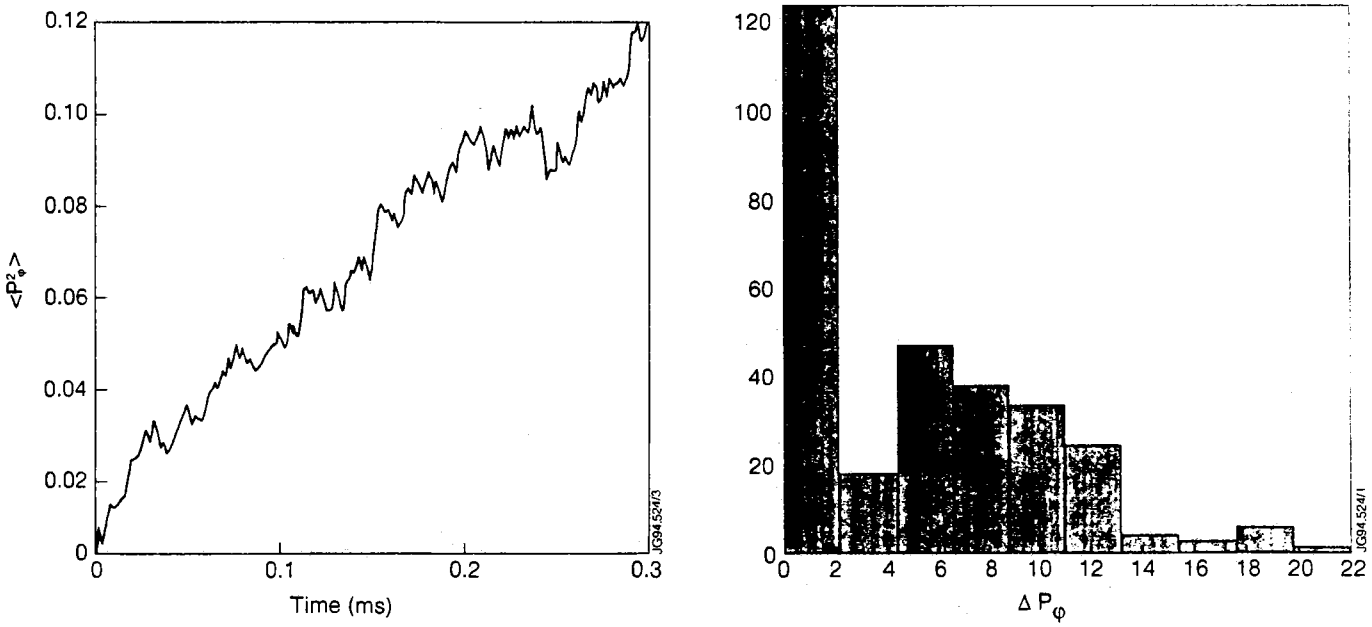

Fig. 9 (a) Variation of $\langle \Delta P_\varphi^2 \rangle \times 10^{40}$ with time for $\delta B_r/B = 4 \times 10^{-3}$ for KTAE-case.
(b) Number of particles with given $\Delta P_\phi \times 10^{20}$ for $\delta B_r/B = 4 \times 10^{-3}$.

- At the same amplitude per mode $\delta B_r/B = 10^{-3}$ KTAE-induced diffusion was found to be DKTAE ~ 1.5DTAE.

SUMMARY

- An extension of CASTOR code for the "complex resistivity" case has been developed to obtain the Kinetic TAE-spectrum in JET plasmas.

- A guiding centre particle following code HAGIS has been developed to study fast particle motion in the presence of unstable TAE and Kinetic TAE modes in JET.

- Additional 1% of α-particles are lost due to the studied n = 3 TAE-mode of $\delta B_r/B = 3 \times 10^{-3}$.

- KTAE-induced collisionnless fast particle diffusion was found to be DKTAE ~ 1.5DTAE at the same amplitude per mode $\delta B_r/B = 10^{-3}$.

- In cases studied alpha-particle losses due to TAE/KTAE cannot lead to the degradation of global confinement in JET, but can be unfavourable for first wall /divertor due to high localization of losses in poloidal direction.

- Possible anomalous radial redistribution of fast particle heating profile due to TAE/KTAE might be important and has to be studied in self-consistent approximation.

REFERENCES

[1] D.J. Sigmar, C.T. Hsu, R. White, C.Z. Cheng, Phys. Fluids B4 (1992) 1506.
[2] H.L. Berk, B.N. Breizman, H. Ye, Phys. Fluids B5 (1993) 1506.
[3] R.R. Mett, S.M. Mahajan, Phys. Fluids B4 (1992) 2885.
[4] W. Kerner , D.Borba, G.T.A.Huysmans, F.Porcelli, S.Poedts, J-P. Goedbloed and R.Bett, Plasma Physics and Controlled Fusion 36, (1994), 911.
[5] J.W. Connor, R.O. Dendy, R.J. Hastie, D. Borba, G. Kuysmans, W. Kerner, S. Sharapov, Proc. 1994 EPS Montpellier.
[6] W. Kerner, L.C. Appel, M. Cox, T.C. Hender, G.T.A. Huysmans, M.R. O'Brien, S.D. Pinches, S. Sharapov, F. Zaitsev, IAEA Conf., 1994, IAEA-CN-60/D-P-II-4.

ICRF Heating of Plasmas in the New JET Divertor Configuration

A C C Sips, M Bures, G Cottrell, C Gormezano,
R Goulding[1], J Jacquinot, P Lamalle, M Lennholm,
F Nguyen[2], E Righi, F Rimini, D Start, B Tubbing, T Wade.

JET Joint Undertaking, Abingdon, Oxfordshire, OX14 3EA, UK.
[1] Oak Ridge National Laboratory, Oak Ridge, Tennessee 37831, USA.
[2] CEN, Cadarache, France.

ICRF Heating of Plasmas in the New JET Divertor Configuration

A C C Sips, M Bures, G Cottrell, C Gormezano, R Goulding[1], J Jacquinot, P Lamalle, M Lennholm, F Nguyen[2], E Righi, F Rimini, D Start, B Tubbing, T Wade.

JET Joint Undertaking, Abingdon, Oxfordshire, OX14 3EA, UK.
[1] Oak Ridge National Laboratory, Oak Ridge, Tennessee 37831, USA.
[2] CEN, Cadarache, France.

ABSTRACT

A new ICRH system has been installed at JET for the pumped divertor configuration:

- Four antennas consisting each of four straps which can be phased independently.
- The main experiments have used $0\pi0\pi$ phasing (dipole) in a D(H) scenario in which the best heating results are observed.
- The coupling on the inner straps is lower compared to the coupling on the outer straps.
- Using dipole phasing the ICRH power to the plasma was raised to 13 MW in combination with 13 MW of NBI power in Elmy H-mode plasmas.

1. INTRODUCTION

The new ICRH system has been used to study a wide variety of reactor relevant Fast Wave heating and Current drive scenarios (see Fig.1). It has the following specifications [1]:

- Each strap is fed by a 2 MW tetrode amplifier.
- With four antennas this gives a total generator power of 32 MW.
- The frequency range is between 25 MHz and 55 MHz.
- The $k_{//}$ spectrum is narrower by a factor of 2-3 compared to the previous ICRH system.
- Real time automatic tuning on the frequency, line length and stub length.
- Feedback on the plasma position to maintain a requested coupling resistance.

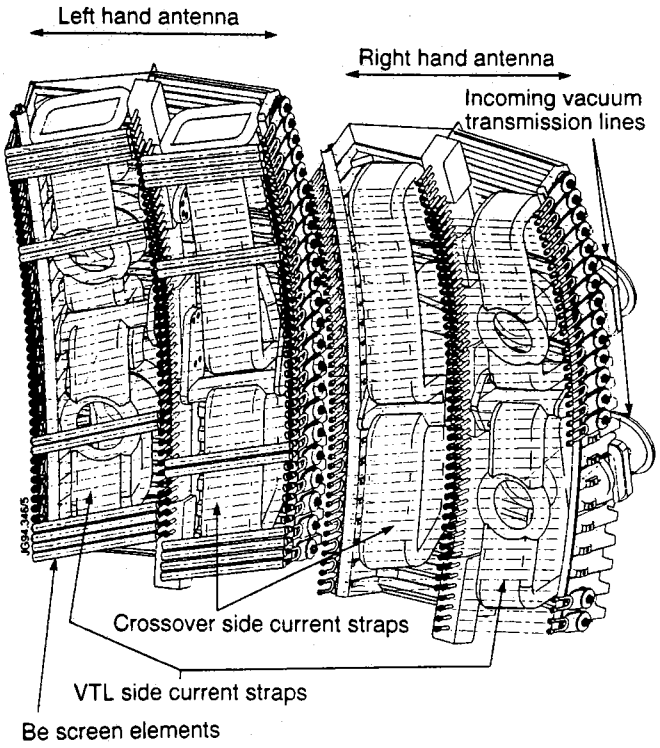

Fig.1: The new four strap, A2 antenna at JET.

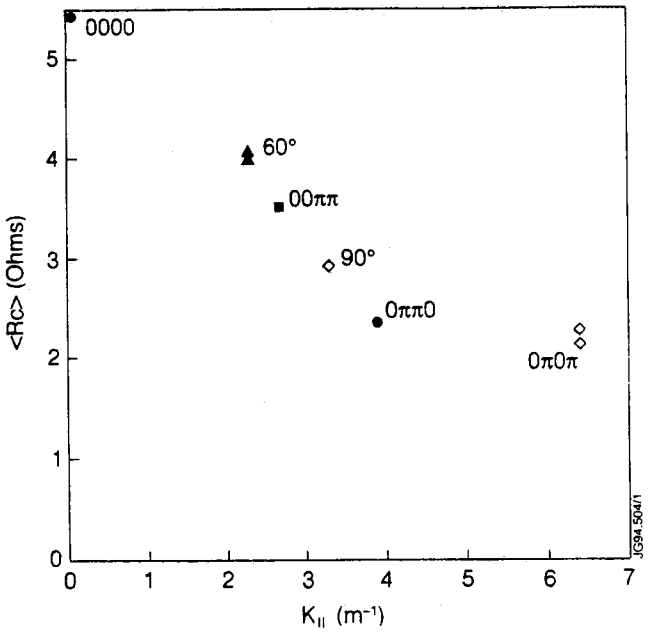

Fig.2: Coupling at different phasing.

2. ICRF COUPLING AND PHASING STUDIES

Coupling of the new antennas has been studied in detail (Fig.2) [2,3]:

- The highest coupling is observed for monopole phasing, a factor two lower coupling for dipole.
- A coupling imbalance between the outer and inner straps for all antenna phasings.
- The occurrence of hot spots on the poloidal limiters when phasing other than dipole is used.

The observed coupling imbalance has been studied over the frequency range of the RF amplifier:

- The average coupling resistance increases with frequency (Fig. 3) and the coupling imbalance decreases with frequency.

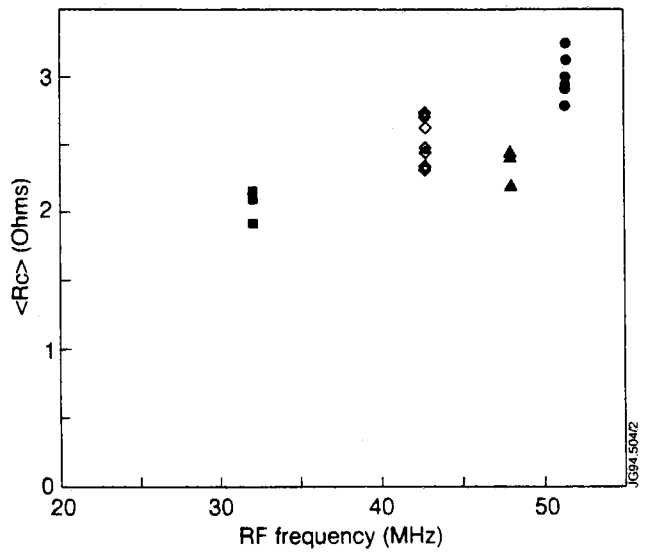

Fig.3: Average coupling vs. Frequency.

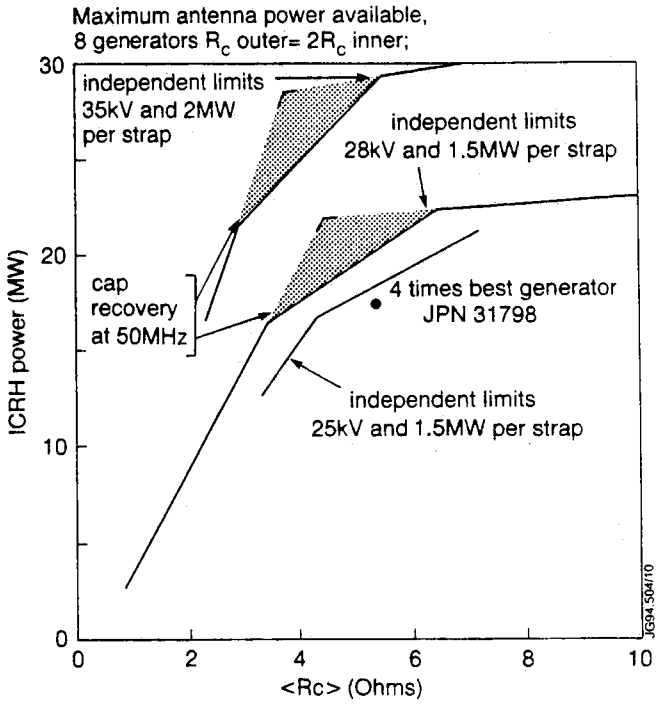

Fig.4: Power capabilities of the ICRH system.

Detailed studies of the coupling imbalance:

- Measurements of the scattering matrix reveal that observed imbalance is inherent to the design of the antenna and not caused by the loading of the plasma.
- The cross-over strap connecting the inner strap to the transmission line has a too high characteristic impedance degrading the coupling of the straps. This shifts the regime of equal coupling of all four straps to around 60 MHz.

To outline the performance of the ICRH system in the following section, two JET pulses are used:

⇒ Pulse 31795, 1MA/2.8T, high $\beta_{pol.}$ Discharge with 13 MW of ICRH and 13 MW NBI [4].

⇒ Pulse 31808, 3MA/2.8T, fast current rise study with early ICRH heating.

3. ICRF AT HIGHEST POWER LEVELS

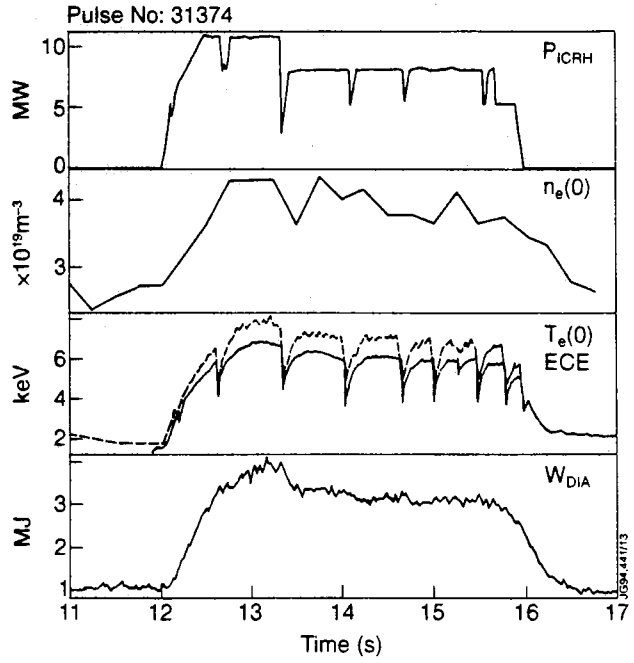

Fig.5: High power at 2MA/2.8T with ICRH only.

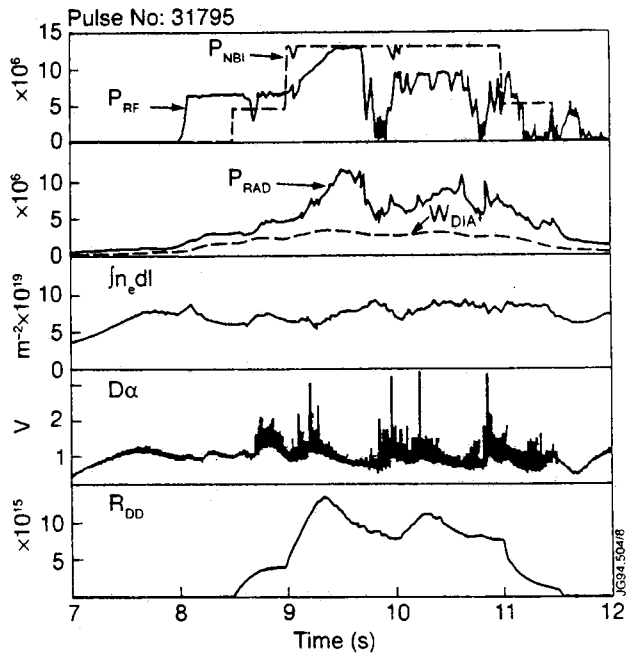

Fig.6: 13MW of ICRH combined with 13MW NBI at 1MA/2.8Tesla.

The JET experiments have concentrated on optimising the ICRH heating in dipole to maximise heating. The results are:

- Power imbalance between the four straps can be used to maximise the available power with respect to the observed coupling imbalance.
- The coupling increases with q_{95} (lower plasma current/higher toroidal field).
- The change of plasma loading during 'Grassy' ELMs can be tolerated by the transmitter. Under these conditions the coupling increases significantly. At 'Giant' ELMs the systems trips.
- 11 MW of ICRH has been coupled at 2MA/2.8T with 15 MW of NBI (Fig. 5), and 13 MW has been coupled to a 1MA/2.8T plasma with 13 MW of NBI (Fig. 6).

- Recently the first RF only H-mode of the present campaign was obtained in a 1MA/2.8T discharge. The power level was 9MW using dipole phasing at 42MHz. The average coupling resistance before the H-mode was 3 Ohm which dropped to 1.8 Ohm during the 100ms ELM-free phase, this caused tripping of some of the amplifiers. The distance from the antenna at the onset of H-mode was 2 centimetres.

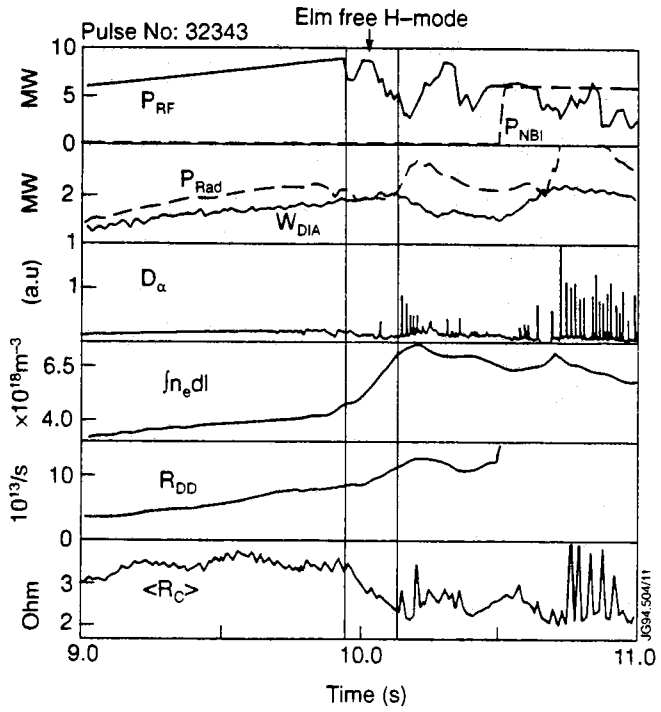

Fig.7: First RF H-mode at 1MA/2.8T.

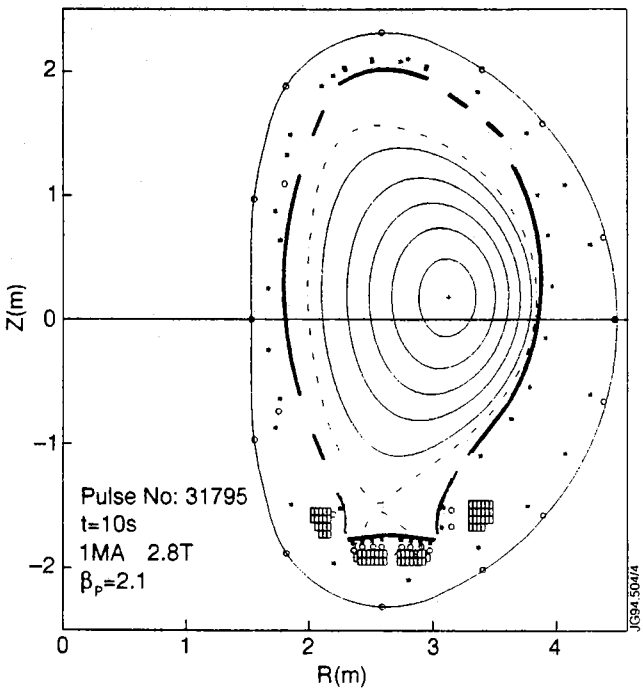

Fig.8: Configuration with high combined heating power at 1MA.

4. PLASMA SHAPING AND PLASMA POSITION CONTROL

The antenna design with respect to the shape of the Last Closed Flux Surface is as follows (Fig. 9):

- Discrete poloidal limiters are installed on each side of the antenna.
- The position of the screen is 20 mm behind the front surface of the Carbon tiles of the poloidal limiter, the straps are 36 mm behind the front of the screens.
- The Be-screen bars are aligned for a field line helicity obtained at low edge q (q_{95}=2.3 for 5MA/ 3.4T).

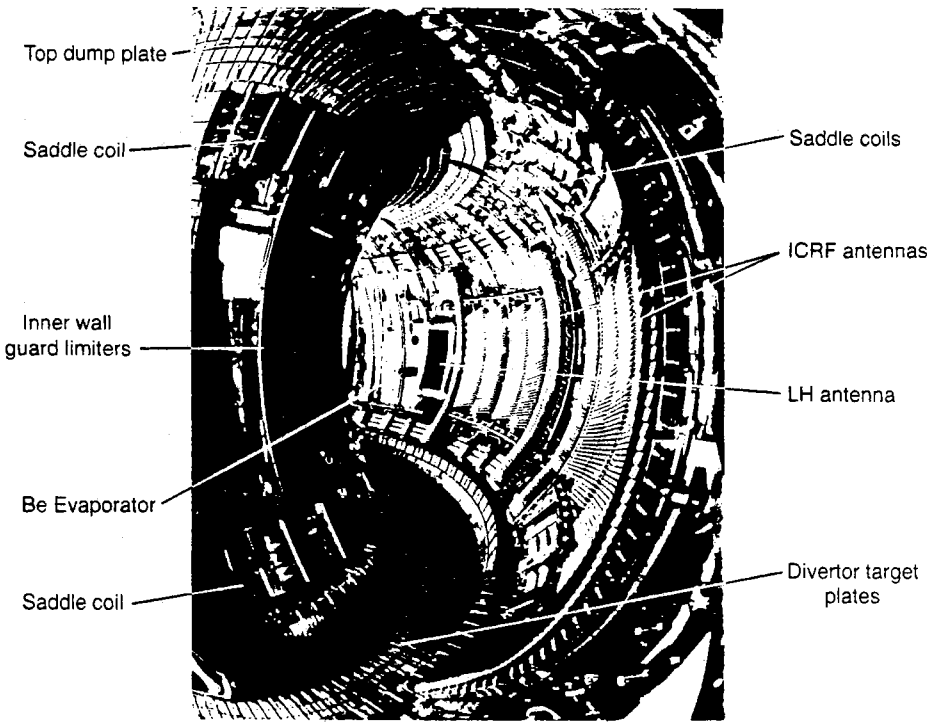

Fig.9: Poloidal view of the antenna.

⇒ Position feedback control (Fig. 10):

The feedback on the vertical field at JET can be used to maintain a requested coupling resistance since the coupling depends almost linearly on the plasma radial position [2]. During this feedback the fast real time boundary reconstruction monitors distances from the LCFS to the antenna:

- To define an inner limit for the radial position under coupling resistance feedback.
- To define an outer limit for the radial position under coupling resistance feedback. This to keep the plasma from moving into the limiter when the coupling request can not be achieved.
- To define a radial position when the ICRF system trips completely.

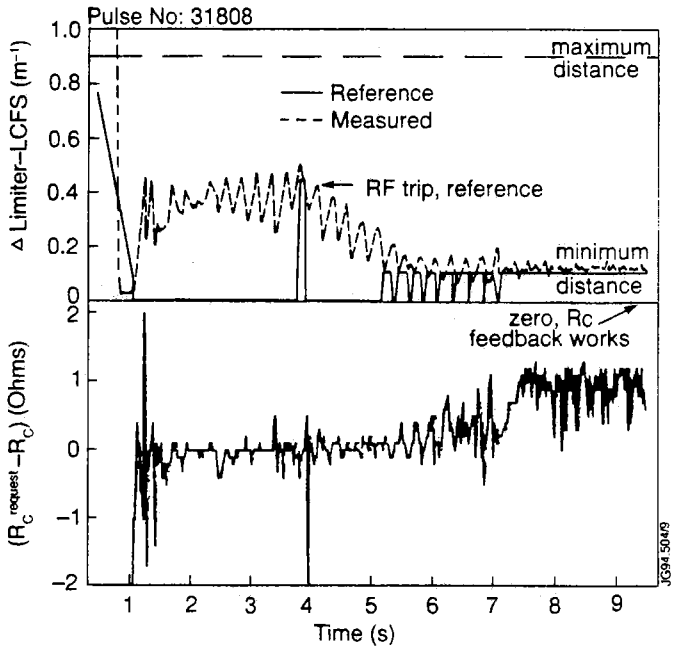

Fig.10: Plasma position feedback.

⇒ **Shape of the LCFS (Fig. 11 and Fig. 8):**

The ICRH coupling is related to the alignment of the LCFS to the shape of the antenna:

- A well aligned LCFS gives 1 Ohm better coupling compared to the so called standard Fat plasma in JET (Figures 11a and 11b compare the two shapes for equal conditions). However the well aligned LCFS is difficult to maintain due to variations in plasma inductance and beta.
- When the LCFS has a much smaller radius of curvature compared to the poloidal limiters the field lines are allowed to penetrate into the antenna screen raising the density in front of the strap.
- Under this condition it is observed that the coupling is improved again compared to a standard JET configuration. Only in this configuration the coupling is even further improved with the application of NBI (Fig. 8).

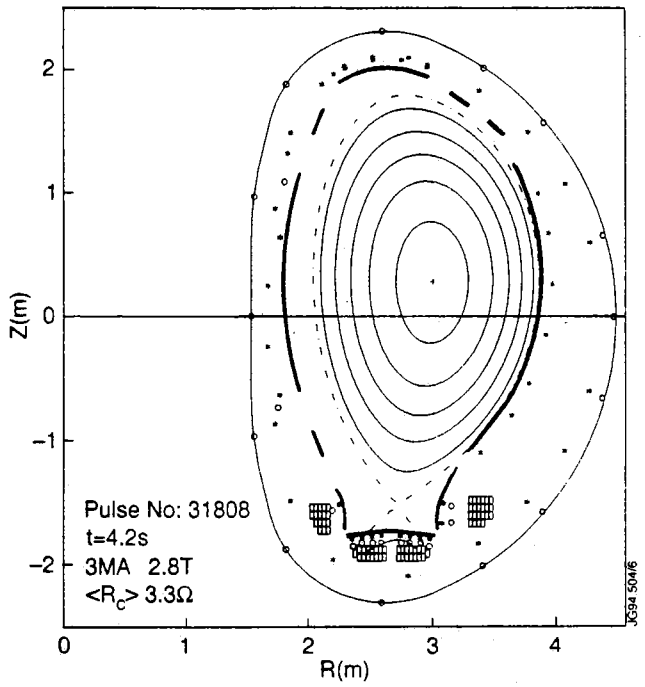

Fig.11(a): Well aligned LCFS.

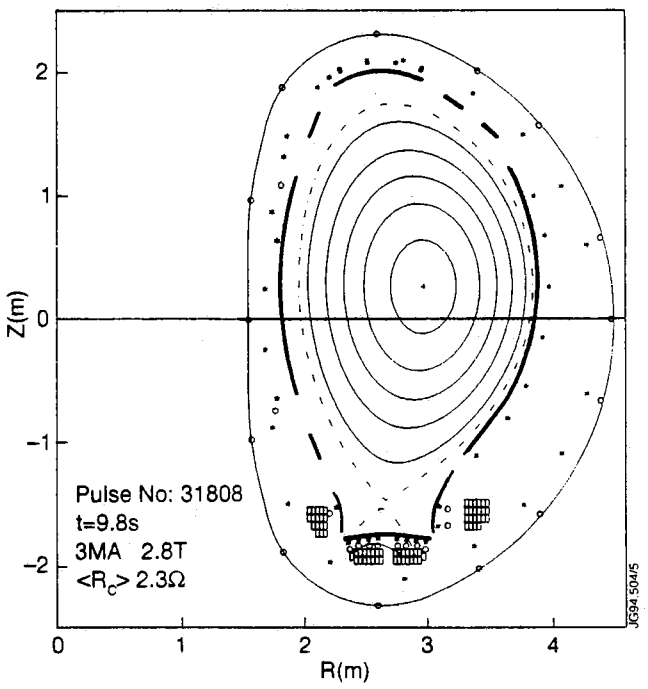

Fig.11(b): Standard Fat plasma.

5. FUTURE EXPERIMENTS AND POSSIBLE ANTENNA UPGRADES

In view of the results presented above the following modification the ICRH system are being prepared:

Problems	Remedies and potential power gain
Bad heating efficiency and hot spots in monopole phasing.	Bumper limiter between inner straps and shield ends of antenna (1995 shutdown). Move plasma away from antenna (to be assessed). Power gain: factor 2.
Coupling imbalance between inner and outer straps.	Replace or change cross-over strap. Work at highest frequencies (this campaign). Power gain: factor 1.25.
Crowbars due to ELMs or rapid change at the plasma edge.	Trombones in Outer Transmission lines and improve trip identification system. No power gain but system more reliable (under study).
Electronics generate side bands which limit the power generation for low coupling.	New electronics (starting from October 1994). Power gain: factor 1.5 for low coupling, factor 1.2 for high coupling cases.

- The use of the ICRF antenna test bed will be crucial in the development of these modifications.

6. REFERENCES.

[1] Wade, T., et al, to be published in Fusion Engineering and Design, 1993.
[2] Bures, M., Proceedings of 21st EPS, Montpellier, 1994.
[3] Rimini, F., et al, IAEA-CN-60/A3/5-P-7, Seville, 1994.
[4] Gormezano, C., et al, IAEA-CN-60/A-5-I-3, Seville, 1994.